Engineering Nanocarbon Interfaces for Electron Transfer

by
Andrew J. Hilmer

Bachelor of Science in Chemical Engineering
University of Rochester, 2008

SUBMITTED TO THE DEPARTMENT OF CHEMICAL ENGINEERING IN PARTIAL FULFILLMENT OF THE REQUIREMENTS FOR THE DEGREE OF DOCTOR OF PHILOSOPHY IN CHEMICAL ENGINEERING
AT THE
MASSACHUSETTS INSTITUTE OF TECHNOLOGY

September, 2013

Signature of Author: _____
Department of Chemical Engineering
June 7, 2013

Certified by: _____
Michael S. Strano
Professor of Chemical Engineering
Thesis Supervisor

Accepted by: _____
Patrick S. Doyle
Professor of Chemical Engineering
Chairman, Committee for Graduate Students

Engineering Nanocarbon Interfaces for Electron Transfer

by
Andrew J. Hilmer

Submitted to the Department of Chemical Engineering
on June 7, 2013, in Partial Fulfillment of the
Requirements for the Degree of
Doctor of Philosophy

Abstract

Electron-transfer reactions at nanometer-scale interfaces, such as those presented by single-walled carbon nanotubes (SWCNTs), are important for emerging optoelectronic and photovoltaic technologies. Electron transfer also governs a primary means by which these interfaces are chemically functionalized and subsequently manipulated. This thesis explores several chemical approaches to understanding and controlling charge transfer at nanocarbon interfaces. In the first part of this thesis, we explore ground-state electron transfer via the chemical reaction of SWCNTs with selected diazonium salts as a means of controlling the number of moieties attached to a given nanotube. We initially explore this reaction theoretically using a kinetic Monte Carlo simulation, with rate parameters evaluated using Gerischer-Marcus theory, in order to examine the extent to which these reactions can be controlled stoichiometrically. These modeling results indicate that heterogeneities in SWCNT chiral population result in a large variance in the number of covalent defects, even at low conversions, thereby limiting the ability to control these reactions through stoichiometry.

We then experimentally examine the ability to impart an additional degree of control over these reactions through utilization of the adsorbed surfactant layer. Surfactants are commonly employed in the processing of nanoparticles to impart colloidal stability to otherwise unstable dispersions. We find that the chemical and physical properties of adsorbed surfactants influence the diazonium reaction with SWCNT in several ways. Surfactants can impose electrostatic attraction or repulsion, steric exclusion, and direct chemical modification of the reactant. Electrostatic effects are most pronounced in the cases of anionic sodium dodecyl sulfate and cationic cetyltrimethylammonium bromide, where differences in surfactant charge can significantly affect the ability of the diazonium ion to access the SWCNT surface. For bile salt surfactants, with the exception of sodium cholate, we find that the surfactant wraps tightly enough that exclusion effects are dominant. Here, sodium taurocholate exhibits almost no reactivity under the explored reaction conditions, while for sodium deoxycholate and sodium taurodeoxycholate, we show that the greatest extent of reaction is observed among a small population of nanotube species, with diameters between 0.88 and 0.92nm. The anomalous reaction of nanotubes in this diameter range implies that the surfactant is less effective at coating these species, resulting in a reduced surface coverage on the nanotube. Contrary to the other bile salts studied, sodium cholate enables high selectivity toward metallic species and small band-gap semiconductors, which is attributed to surfactant-diazonium coupling to form highly reactive diazoesters.

We subsequently move on to examine excited-state electron transfer events between SWCNTs and fullerenes. This electron transfer system is distinct from the diazonium system since it does not result in the formation of a covalent bond between the donor and acceptor species. To study this interface, we synthesized a series of methanofullerene amphiphiles, including derivatives of C_{60}, C_{70}, and C_{84}, and investigated their electron transfer with SWCNT of specific chirality, generating a structure/reactivity relationship. In the cases of lipid-C_{61}-PEG and lipid-C_{71}-PEG, which are predicted to similar surfactant surface coverages, band-gap dependent, incomplete quenching was observed across all semiconducting species, indicating that the driving force for electron transfer from SWCNT is small. This is further supported by a Marcus theory model, which predicts that the energy offsets between the SWCNT conduction bands and the fullerene LUMO levels are less than the exciton binding energy of the SWCNT in these two systems. In contrast, the lipid-C_{85}-PEG derivative shows complete quenching of all SWCNT species utilized in this work. This enhancement in quenching efficiency is consistent with the fact that the LUMO level of C_{85} methanofullerene is approximately 0.35eV lower than that of the smaller fullerene adducts, resulting in energy offsets which exceed the exciton binding energy. This result, combined with the fact that C_{85} has much higher photo-stability than C_{61} and C_{71}, makes this larger fullerene adduct a promising candidate for SWCNT-based sensors and photovoltaics.

Finally, we design and synthesize fullerene derivatives that self-assemble into one-dimensional arrays. We find that a dendritic fullerene, which possesses a Boc-L-Ser-L-Ala-OMe dipeptide sequence at its apex, selectively forms *S*-oriented, helical, one-dimensional nanowires upon cooling from an isotropic state in cyclohexane. These nanowires possess diameters of 3.76 $\pm$ 0.52nm, and can be several microns in length. Control molecules, which do not possess the dipeptide sequence, only produce poorly formed aggregates under identical conditions, indicating that dipeptide-dipeptide interactions are integral to assembly. These nanorods open new opportunities in the chiral assembly of novel electron acceptor materials for optoelectronic and photovoltatic applications.

Thesis Supervisor: Michael S. Strano
Professor of Chemical Engineering

Acknowledgements

I would like to thank my advisor, Professor Michael S. Strano, for his enthusiasm and mentorship, and for encouraging me to pursue an area of research that has extended beyond the expertise of our lab. I am grateful to have had the opportunity to work under him during the course of my thesis. I would also like to thank my committee members, Professor T. Alan Hatton and Professor Timothy M. Swager, for their unending support, as well as their criticism over the past several years. I truly feel that they have always had my best interests in mind, and I am privileged to have had them on my thesis committee. Thirdly, I would like to thank my labmates, friends, and all the wonderful people that I have had the opportunity to meet during my time at MIT; they have been a source of constant support. I would like to thank Dr. Changsik Song for mentoring me early in the course of my PhD, and Dr. Shangchao Lin for his collaborations in bringing a molecular understanding to the surfactant studies explored in this thesis. I would like to thank my wife (and former labmate), Dr. Jingqing Zhang, for both her support and the innumerable helpful discussions that we have had over the past few years. She has certainly demonstrated that love can arise in the most unexpected places. Finally, I would like to thank my family for their constant support of my scientific education. It is to them that this thesis is dedicated.

Table of Contents

List of Figures

from excited-state SWCNT to the fullerene molecule, while k_{CR} is the rate constant associated with relaxation of the SWCNT excited state to the valence band.

Figure 1.13 In organic photovoltaics, the development of donor or acceptor species which self-assemble on nanoscale dimensions could allow for the design of heterojunctions with large interfacial area, while maintaining contiguous pathways for charge carrier extraction.

Figure 2.1 Binomial probability distributions for the number of attached groups at six different conversions, p, for n = 1000. The inset depicts the variance in the number of attached groups as a function of the mean number of groups attached.

Figure 2.2 (a) Distribution of nanotubes for which density of states and relative rate constants were evaluated. (b) Interpolated surface plot showing the SWCNT composition for a typical HiPCO solution used during a simulated reaction.

Figure 2.3 Example of the transformation from nanoribbon representation to reactive-site-matrix for a (n,m) = (6,4) nanotube. The number of rows in the site matrix is equal to n + m with the edge connectivity being defined by m - n for alternating carbons along the nanoribbon edge. The number of columns is determined by the tube length (see text).

Figure 2.4 Initial and modified densities of states for (10,0) and (8,8) nanotubes evaluated using the results of DFT calculations[2]. E_{redox} and E_{Fermi} are depicted for each nanotube, and the reorganization energy associated with electron transfer is shown in (a).

Figure 2.5 (a-e) Distributions in the number of functional groups attached for five selected conversions. The mean number of groups attached and variance in the number of groups attached are provided for each plot. (f) Depicts the relationship between the variance in the number of attached functional groups and the mean number of attached groups.

Figure 2.6 (a) Total fractions of mono- and bifunctional tubes as a function of conversion. (b) Monofunctional species fractions for eight selected chiralities as a function of conversion.

Figure 2.7 Effect of rate constant distribution on the variance in the number of attached groups, with columns corresponding to FC-CVD, HiPCO and Co-MCM-41 SWCNT, respectively. (a-c): Rate constant distributions of pristine SWCNTs. (d-f): Rate constant distributions in the limit of complete reaction. (g-i): Variance in number of functional groups attached (as a function of mean groups attached) for the cases of unmodified and modified site reactivities.

Figure 2.8 Fraction of monofunctional tubes as a function of conversion for three different nanotube solutions, along with the monofunctional fractions of both metallic and semiconducting species.

Figure 2.9 Implications of chiral distribution for nanotube separation. Because electron transfer chemistries are typically selective toward metallic species, the functionalized sample has been denoted as the "metallic solution," while the unfunctionalized sample has been labeled as the "semiconducting solution."

Figure 3.1 Structures of the diazonium ion and six surfactants utilized in this study. Diazonium salt: (a) running reactions under slightly acidic conditions favors the cationic diazonium ion over the base-mediated conversion to diazotates and diazoanhydrides. Surfactants: (b) sodium dodecyl sulfate, (c) cetyltrimethylammonium bromide, (d) sodium cholate, (e) sodium deoxycholate, (f) sodium taurocholate, and (g) sodium taurodeoxycholate. The bile salts, (d)-(g), have rigid steroidal backbones, which impart them with hydrophobic and hydrophilic "faces". The rigidity of these bile salts causes them to form close-packed

structures on the nanotube surface. The linear chain surfactants, (b) sodium dodecylsulfate and (c) cetyltrimethylammonium bromide possess less rigid, lipidic chains, which tend to coat the nanotube in a more disordered manner.

Figure 3.2 Reaction data for SDS and CTAB-SWCNTS under various conditions. (a)-(c) Selective reaction data for SDS-SWCNTs under dark conditions. (a) Absorbance data shows little change under addition of small quantities of reagent. (b) Fluorescence spectra show an enhanced reactivity of small band-gap semiconductors for all aliquot sizes. (c) Raman data (normalized by the G-peak intensity) depicting slight increases in the D-to-G ratio with additional reagent, which is characteristic of covalent derivatization. (d)-(e) In situ snapshots of the transient fluorescence quenching response of carbon nanotubes suspended in (d) SDS and (e) CTAB, upon addition of diazonium salt. Here the samples are continuously illuminated at an excitation wavelength of 785 nm. (d) In the case of SDS, a similar fluorescence response is observed across all species. (e) CTAB exhibits a preferential reaction of small diameter species. Insets depict the relative reactivities of 8 nanotube species as a function of tube radius. (f)-(g) G-peak-normalized pre- and post-reaction Raman spectra (633nm excitation) for (f) SDS and (g) CTAB-SWCNTs, which demonstrate an enhanced D/G ratio (D peaks shown in insets).

Figure 3.3 (i) Absorbance (ii) fluorescence, and (iii) Raman data for reactions performed under conditions similar to SDS-selective reactions (1.10×10^{-4} moles diaz./mole carbon, pH 5.5, T = 45°C, 24 hour reaction time). Rows correspond to the surfactants (a) CTAB, (b) SC, (c) SDC, (d) STC, and (e) STDC. Because of the loose packing of SDS on the surface of the nanotube, reaction occurs at diazonium concentrations that are several orders of magnitude lower than those used for other surfactants. The absorbance, fluorescence, and Raman spectra (above) show that, under similar conditions, the other surfactant-SWCNT solutions undergo little to no reaction.

Figure 3.4 Absorbance spectra for four bile salts, (a) sodium cholate and (b) sodium deoxycholate, (c) sodium taurocholate, and (d) sodium taurodeoxycholate, and Raman D/G ratios for (e) sodium cholate, (f) sodium deoxycholate, and (g) sodium taurodeoxycholate. Spectra have been normalized to match abs(632nm) of the control. (a) Sodium cholate provides the clearest demonstration of selective reaction, with metallic and large diameter (small bandgap) nanotubes reacting preferentially. The other three species also appear to demonstrate an enhanced reactivity of small band-gap semiconductors, albeit to different extents. The increase in baseline, toward the ultraviolet region, can be attributed to reaction byproducts. Raman reaction trends for sodium deoxycholate (f) and sodium taurodeoxycholate (g) appear similar, which is consistent with their absorbance spectra, which also show similar results. (e) The D/G ratios for sodium cholate attain higher values than those observed for the other bile salts, which is consistent with a greater decrease in the absorbance associated with Van Hove singularities.

Figure 3.5 Fluorescence spectra and deconvoluted fractional quenching results for the four bile salts used in this study: (a) sodium cholate, (b) sodium deoxycholate, (c) sodium taurocholate, and (d) sodium taurodeoxycholate, at an excitation wavelength of 785nm. (a) As observed in the absorbance spectra, sodium cholate demonstrates predominantly electron-transfer selective reaction, with large diameter (small bandgap) nanotubes reacting preferentially. For sodium cholate, the fractional quenching results are generally plotted from large to small E_{11} gap. For species whose E_{11} emissions overlap to the extent that a single peak is observed (i.e. (9,4)/(7,6) and (10,5)/(8,7)), the species with the larger E_{22} gap has been plotted first. In contract to sodium cholate, the other three bile salts display preferential reactivity among a small population of nanotubes (see text).

Figure 4.6 Excitation-emission plots for SWCNTs suspended in (a) lipid-C_{71}-PEG and (b) lipid-C_{85}-PEG. Plots are depicted on the same scale. In the case of Lipid-C_{85}-PEG, no significant fluorescence was observed above background.

Figure 4.7. Absorbance and fluorescence results from fullerene family analysis. (a) Absorbance spectra of SWCNT suspensions in lipid-PEG, as well as the C_{61}, C_{71}, and C_{85} methanofullerenes. (b) Averaged fluorescence spectra (3 samples) for these amphiphilic systems, acquired at an excitation wavelength of 785nm. (c) Deconvoluted relative intensities, normalized to the intensities of SC-SWCNT, for the three lipidic methanofullerenes.

Figure 4.8 Plots of $(E_{11})^2\Delta E_{11}$ versus $1/d^4$, evaluated from deconvoluted absorbance spectra, for the lipid-PEG, lipid-C_{61}-PEG, pyrene-PEG, and pyrene-C_{61}-PEG. The slopes of these curves were used to predict the fractional coverage of methanofullerene on the SWCNT surface.

Figure 4.9 Plots of $(E_{11})^2\Delta E_{11}$ versus $1/d^4$ for the lipid-C_{71}-PEG and lipid-C_{85}-PEG, with lipid-PEG shown for reference. The slopes of these curves were used to predict the fractional coverage of methanofullerene on the SWCNT surface.

Figure 4.10 Predicted energy offsets between SWCNT conduction bands and the C_{61} LUMO level. Offsets were evaluated using the C_{61} LUMO level determined from Marcus theory. The data are compared with *ab initio* values reported in Ref [39] for $PC_{61}BM$.

Figure 4.11 Parity plot showing the agreement between experimental and theoretical relative rate constants for different values of the reorganization energy.

Figure 5.1 Molecular structures of the fullerodendrimers studied in this work.

Figure 5.2 Temperature-dependent absorbance data for fullerodendrimers 1 (left) and 2 (middle) in cyclohexane at concentrations of 80μM. The rightmost figure follows the absorbance at 259nm as a function of temperature. Upon cooling from an isotropic state, the fullerene peak at 259nm decreases, with the evolution of a new peak near 267nm. The transition temperature occurs approximately 20°C higher in the case of fullerodendrimer 2.

Figure 5.3 SEM (a),(d) and AFM (b),(c),(e),(f) images of self-assembled morphology. (d) SEM of a drop-cast solution of 1 shows the formation of densely matted regions of aligned fibers, while (a) SEM of a drop-cast solution of 2 shows randomly oriented domains. (e-f) AFM on spin-cast assemblies of 2 show structurally homogeneous fibers with average diameters of 3.76 ± 0.52nm, and lengths of a few hundred nanometers to > 10μm. (b-c) AFM on spin-cast assemblies of 1 show the formation of aggregated fibrils, rather than well-formed wires.

Figure 5.4 AFM (a) phase image, and (b) height profiles obtained from helical assemblies of fullerodendrimer (2). The inset of (b) shows a height image of an isolated, helical fiber, along with the positions at which height traces were evaluated.

Figure 5.5 AFM phase images of assembled fullerodendrimer (2) showing helical striations along the length of the assembled nanorods. (b) Zoomed-in phase image of one of these assemblies.

Figure 5.6 Left: Room-temperature CD spectra of fullerodendrimers 1 and 2. Fullerodendrimer 1, which lacks the dipeptide sequence, shows no significant CD features, whereas fullerodendrimer 2 shows clear spectral features, indicating selectivity toward a particular handedness during self-assembly. Middle: temperature-dependent CD spectra of fullerodendrimer 2. CD features emerge upon cooling from an isotropic state, indicating that these features emerge during the self-assembly of the nanorods, and are not intrinsic to

the molecule, itself. Right: comparison between temperature dependent absorbance (259nm) and the temperature dependent CD signal at 283nm.

Figure 7.1 Absorbance spectra of SWCNT suspensions in amphiphiles (4), (7), (10), (12), and (14) – from Schemes 4-1 and 4-2 – before (black) and after (red) removal of free amphiphile. In order to account for slight concentration differences, absorbance spectra have been adjusted by a constant such that their absorbance values near 900nm are similar. Despite small redistributions in chirality, most spectra taken before and after removal are fairly consistent. However, the pyrene-PEG sample shows evident decrease in peak-to-valley ratio, as well as slight peak shifting, indicating that aggregation is occurring. Visible aggregates were also observable the pyrene-PEG system after the removal of excess surfactant.

Figure 7.2 MALDI-TOF for the three methanofullerene intermediates, (3), (6), and (9) from Scheme 4-1.

Figure 7.3 MALDI-TOF on the PEGylated amphiphiles (4), (7), (10), (12) and (14) from Schemes 4-1 and 4-2.

Figure 7.4 Zoomed-in MALDI-TOF on the PEGylated amphiphiles (4), (7), (10), (12) and (14), from Schemes 4-1 and 4-2, along with expected values.

Figure 7.5 MALDI-TOF comparing the three methanofullerenes intermediates used for the fullerene family analysis.

Figure 7.6 MALDI-TOF comparing the three PEGylated methanofullerenes used for the fullerene family analysis.

Figure 7.7 AFM images showing individually dispersed nanotubes in the cases of pyrene-PEG, pyrene-C61-PEG, lipid-PEG, and lipid-C61-PEG. SWCNT suspensions using methyl-C61-PEG displayed bundles of nanotubes.

Figure 8.1 MALDI-TOF data for the two fullerodendrimers used in the self-assembly study.

Figure 8.2 Variable temperature ^{1}H-NMR data for the peptidic fullerodendrimer in C_6D_{12}.

Figure 8.3 Intensity of the aromatic NMR feature at ~6.74ppm as a function of temperature. The magnitude of the feature shows a monotonic decrease as the sample is cooled. Due to the higher concentration of the sample, the assembly transition is shifted to higher temperatures in comparison with the variable-temperature absorbance and circular dichroism datasets.

1. Introduction

Single-walled carbon nanotubes (SWCNTs) are one-dimensional materials consisting of a single cylinder of entirely sp^2 hybridized carbon atoms. Essentially, SWCNTs are grapheme sheets which have been seamlessly rolled into cylinders that possess diameters on the order of one nanometer. The structure of the resulting nanotube, and its corresponding electronic properties, are determined by the way in which the graphene sheet is rolled. When looking at the honeycomb lattice of a sheet of graphene (see Figure 1.1), two unit vectors can be defined, $\boldsymbol{a_1}$ and $\boldsymbol{a_2}$, each of which connects one lattice site to an adjacent neighbor. Using one site as the origin, all other lattice points can be described by a vector, $\boldsymbol{C}$, which consists of a linear combination of these two unit vectors:

$$\boldsymbol{C} = n\boldsymbol{a}_1 + m\boldsymbol{a}_2$$

When the graphene sheet is rolled such that the tail and the head of the vector $\boldsymbol{C}$ are connected, an (n,m) carbon nanotube is formed, and the vector is called the *chiral* or *rolling vector* of the nanotube[3]. The (n,m) indices of a carbon nanotube determine both the diameter of the nanotube and its electronic properties, and the combination of these indices are termed the "chirality" of the nanotube. Except for armchair (n,n) and zigzag $(n,0)$ nanotubes, all other species of nanotube will also possess a handedness (R or S) with which they are rolled. Therefore, the chiral index is somewhat of a misnomer, since it solely refers to the rolling vector, not the handedness of the resulting nanotube. If $(n-m) = 3d$, in which d is an integer, the

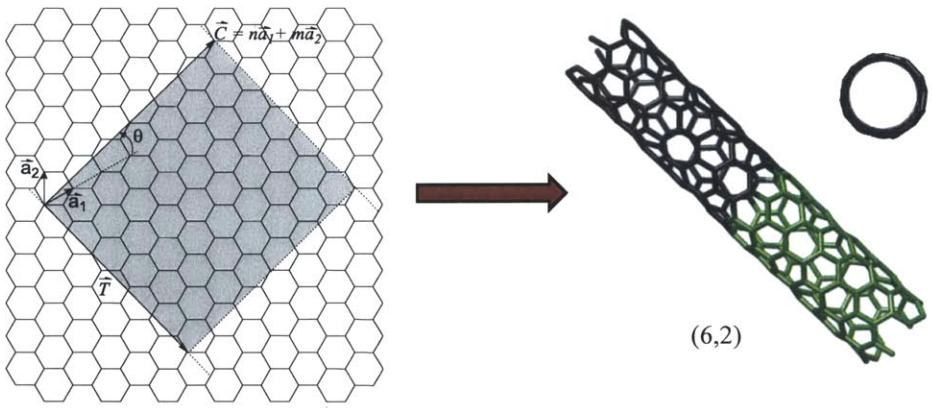

Figure 1.1 Graphene lattice representation of a carbon nanotube. a_1 and a_2 form the two unit vectors of the graphene lattice. By taking a linear combination of these two unit vectors, na_1+ma_2, it is possible to generate any species of carbon nanotube. The (n,m) index referring to a particular species of nanotube is termed its "chirality". Shown above is a (6,2) nanotube. The translational vector, T, specifies the translational repeat unit along the axial direction, or the period with which the nanotube maps back onto itself.

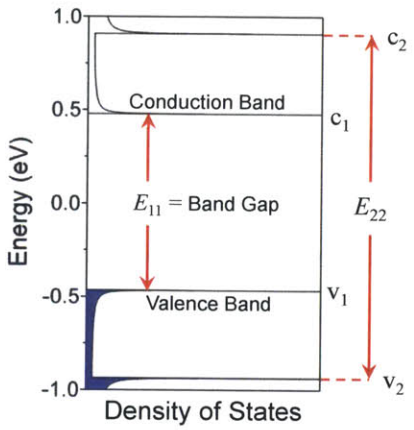

Figure 1.2 Schematic energy diagram of a generic semiconducting SWCNT depicting both the valence and conduction bands, as well as the various optical transitions that can occur. The E_{11} transition is also refered to as the band-gap of the nanotube.

resulting nanotube is metallic or semi-metallic; all other nanotubes are semiconducting[3-5]. Additionally, for semiconducting carbon nanotubes, the chirality determines the optical bandgap of that species. A schematic depicting the electronic states of a semiconducting nanotube is depicted in Fig. 1.2. Here, the occupied *valence band* is shown in blue, while the unoccupied *conduction band* is located at the top of the energy axis. Optical excitation can occur between the v_1-c_1 and v_2-c_2 transitions, which are termed the E_{11} and E_{22} transitions, respectively. Excitation of the E_{22} transition is followed by ultrafast relaxation to the c_1 band[6], and subsequent radiative (or non-radiative) decay to the valence band, which results in the characteristic near-infrared fluorescence of single-walled carbon nanotubes. The manner in which chirality can influence the electronic properties of SWCNTs is generally depicted in Fig 1.3 for three chiralities of carbon nanotube. By comparing the two semiconducting species (6,5), and (10,8), it is apparent that the chirality influences the energy separation between both the E_{11} and E_{22} transitions. Thus, there is a unique combination of E_{11} and E_{22} transition energies for each semiconducting species of carbon nanotube. This property of semiconducting carbon nanotubes is more apparent upon examination of 3-D excitation-emission plots of nanotube fluorescence, such as that shown in Fig 1.4. Here, the y-axis corresponds to the wavelength of photo-excitation, while the x-axis corresponds to the wavelength of SWCNT

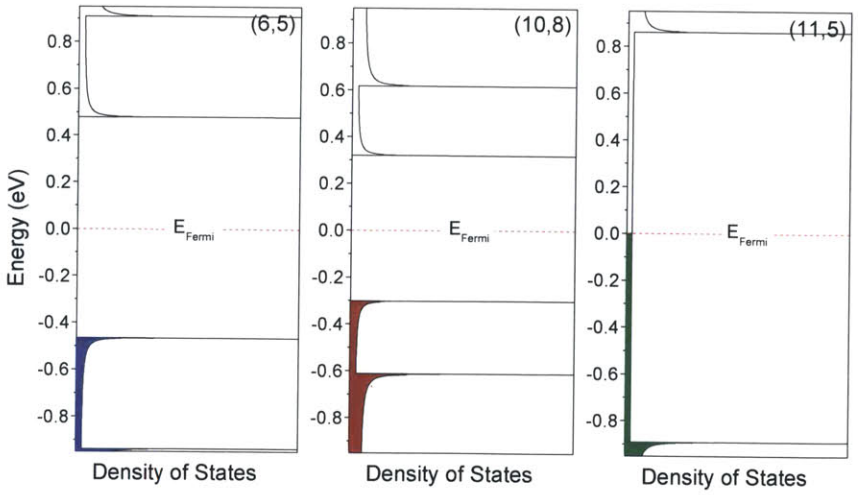

Figure 1.3 Density of states representations for three chiralities of SWCNTs. The (6,5) and (10,8) nanotubes are semiconducting, while the (11,5) SWCNT is metallic. For semiconducting species, the chirality of the tube determines the energies of the E_{11} and E_{22} optical transitions.

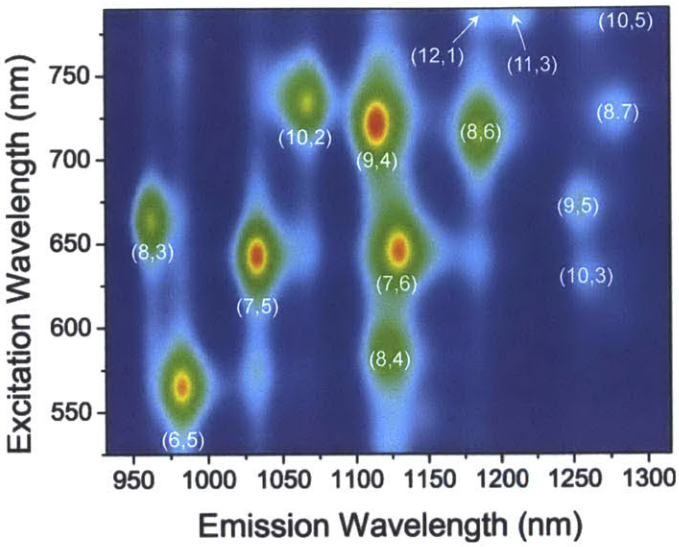

Figure 1.4 3D excitation-emission plot showing the distinct combination of E_{11} and E_{22} transition energies for various chiralities of semiconducting carbon nanotubes. The y-axis corresponds to the wavelength of photoexcitation (E_{22} energies), while the x-axis corresponds to the wavelength of SWCNT photoemission (E_{11} energies).

fluorescence emission. As can be seen from the plot, in scanning through the excitation wavelength range on the y-axis, when the energy of the excitation wavelength matches the E_{22} transition energy of a particular nanotube, there is an enhancement in the fluorescence emission of that nanotube. Thus, each peak in the excitation-emission plot corresponds to a particular chirality of carbon nanotube, with a unique pairing of E_{11} and E_{22} transitions. In addition to this property of semiconducting nanotubes, certain chiralities of nanotubes are metallic, as mentioned above. These species, such as the (11,5) nanotube in Fig 1.3, do not have a band-gap, but instead possess a finite density of states near the Fermi level. Because the chirality of a carbon nanotube influences both the nature of the nanotube electronic properties (metal, semimetal, or semiconductor) as well as the optical transition energies of semiconducting SWCNTs, electron transfer events which involve SWCNTs are highly dependent upon the nanotube chirality.

1.1. Ground-State Electron Transfer: Toward Discretized Functionalization of SWCNTs

In Chapters 2 and 3 of this thesis, we explore the ability to control the electron transfer reactions of single-walled carbon nanotubes with aryl diazonium salts, with the goal of achieving a minimal number of defect sites.

1.1.1. Motivation—Singularly-Tethered Nanotubes

Singularly tethered nanoparticles – nanoparticles chemically derivatized with a single chemical chain or tether – are emerging as important from both a scientific and technological standpoint. In the past several years, this has primarily been driven by interest in quantum dots or plasmonic nanoparticles, which display interesting optical resonances when assembled into

controlled dimers, trimers, or higher order assemblies[7]. In spherical nanoparticles, it has been found that the introduction of stoichiometric[8] or substoichiometric[9] quantities of ligands has allowed for the synthesis of well-defined nanoparticle assemblies, while excess ligation results in the formation of cross-linked aggregates[9]. Advances in the separation of such ligand-functionalized nanoparticles has led to the creation of hierarchical nanostructures containing a specific number of one[10] or more types of nanoparticles[11]. Building on this progress, Alivisatos and co-workers successfully utilized plasmonically coupled nanoparticles as molecular rulers[12] for monitoring the in vitro cleavage of DNA by EcoR enzymes[13] and the in vivo detection of caspase-3 activation[14]. In other applications, monovalent quantum dots and monovalent streptavidin have been shown to be useful agents for site-selective biological imaging in living cells[15, 16]. However, similar advances in the SWCNT field have lagged behind.

Efforts toward controlling the extent of nanotube covalent reaction have primarily focused on reaction stoichiometry[17], reaction time[18], and harshness of oxidative treatment[19-21]. However, nanotube solutions may possess as many as 30 distinct species of semiconducting nanotubes[22], alone, with each nanotube potentially exhibiting a significantly different affinity toward a reagent molecule. In fact, the reactivity of a particular species is often dependent upon the specific properties of the nanotube, including electronic structure[23-25], diameter [21], and bond curvature radius[26]. Additionally, nanotube solutions contain a distribution of tube lengths, which further complicates the ability to control the extent of SWCNT covalent reaction. Therefore, it remains difficult to obtain similar degrees of functionalization across all species.

To date, the most promising means of controllably functionalizing carbon nanotubes is through regioselective modification of the SWCNT ends[27-29]. This has been elegantly demonstrated by Weizmann et al, who utilized a mild oxidation procedure to introduce carboxylic acid groups to the ends of the SWCNT, which were then addressable for further chemistry[27, 28]. However, under these oxidative conditions, the extent to which the nanotube sidewall is damaged remains unclear. More recently, it has been shown that the suspension of SWCNT by sonication imparts the nanotube ends with carboxylic acid functionalities that can be addressed using EDC/NHS coupling, without the need of acid-based oxidation[29]. However, such methods are intrinsically limited to carboxylic acid functionality, and the yield of

regioselectively modified SWCNTs remains unclear. If high yield, reliable techniques for sparsely functionalizing SWCNTs become available, they would enable such applications as the development of site-directed sensors by utilizing orthogonal chemistries between the wrapping polymer (sensor component) and the covalent attached ligand (directing component). This would allow for sensors to be directed to specific cellular locations while simultaneously detecting a desired analyte. Such a construct is depicted in Figure 1.5.

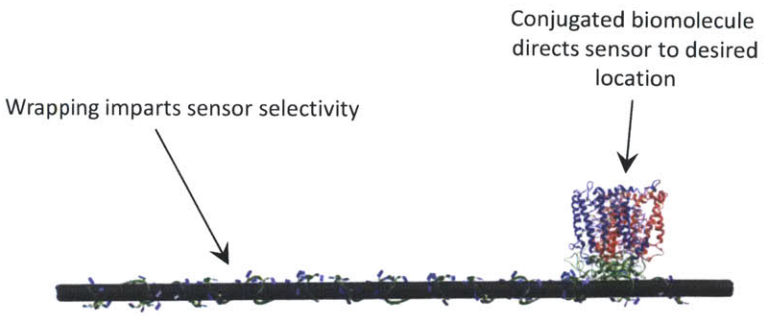

Figure 1.5 Schematic depicting the principles behind using sparsely functionalized nanotubes for directed sensing. Here, the wrapping ligand imparts selectivity for sensing a particular analyte, while the covalently conjugated molecule directs the sensor to a desired location.

In this thesis, we explore the ability to introduce a minimal number of covalent defect sites by utilizing the electron transfer reactions of carbon nanotubes with diazonium salts.

1.1.2. Background and Theory

Nanotubes have been shown to participate in a variety of electron-transfer reactions[23-25]. Here, we focus on the reaction of carbon nanotubes with aryl diazonium salts, in which the rate-determining step involves ground-state electron transfer from the SWCNT valence band to the unoccupied electronic states of the diazonium molecule. This reaction has been shown to proceed through a two-step mechanism[30], in which the nanotube and diazonium molecule form an intermediate charge transfer complex[30, 31]. The reaction network can be described by:

$$A + \theta_{(n,m)} \xrightarrow{k_A^{(n,m)}} A_{ads}\theta_{(n,m)} \xrightarrow{k_R^{(n,m)}} A\theta_{(n,m)} \tag{1.1}$$

where A represents the aryl diazonium salt and $\theta_{(n,m)}$, $A_{ads}\theta_{(n,m)}$, and $A\theta_{(n,m)}$ represent vacant nanotube sites, adsorbed sites, and covalently reacted sites, respectively. Former kinetic studies by Nair et. al. [32] have shown that, under certain reaction conditions, the reaction rate of this system can be described by second order kinetics:

$$\frac{d\theta_{(n,m)}}{dt} = k_A^{(n,m)} A \cdot \theta_{(n,m)} \tag{1.2}$$

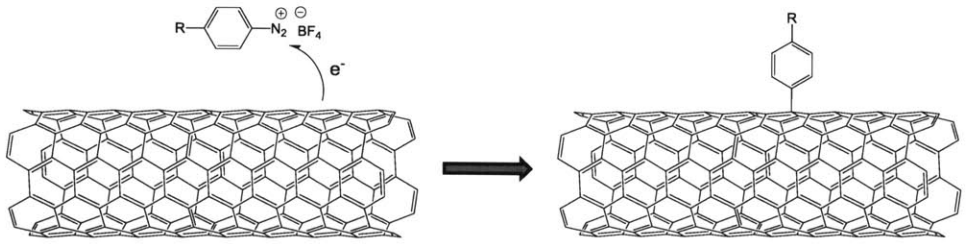

Figure 1.6 Reaction of SWCNTs with aryl diazonium salts are initiated by electron transfer from SWCNT to the diazo moiety, and result in the introduction of a covalent defect to the π-conjugated sidewall.

with the relative rate constants of all nanotubes being evaluated using Gerischer-Marcus theory[33]. This theory is applicable for kinetic networks in which the rate-limiting step involves electron transfer between reacting species. Insights into the applicability of G-M theory to these electron-transfer reactions have been recently provided through computational studies[34]. In that work, it was shown that for diazonium reactions, the counterion (BF_4^-) plays an integral role by actively competing with SWCNT as a source of electron density for stabilizing the diazonium cation. Because of this, the ability of the nanotube to donate electron density, and therefore, the nanotube density of states, is highly important. Gerischer-Marcus theory predicts that the rate of reaction between a carbon nanotube and an electron acceptor molecule is proportional to the degree of overlap between the SWCNT density of states, $DOS_{(n,m)}$, and the distribution of vacant, oxidized states of the diazonium molecule in solution, W_{ox}[33]:

$$k_{ET}^{(n,m)} = \upsilon_n \int_{E_F^D}^{E_F^{SWNT}} \varepsilon_{ox}(E) DOS_{(n,m)}(E) W_{ox}(E) dE \tag{1.3}$$

The densities of states for two semiconducting nanotubes, (6,5) and (10,8), are depicted in Figure 1.7, along with the distribution of vacant states for a diazonium molecule in solution. From this figure, it is evident that smaller band-gap species, such as (10,8), exhibit a greater degree of overlap with the vacant states of the diazonium ion, and therefore react more readily than larger band-gap species, such as (6,5). Further, metallic species, which have a continuum of states near the Fermi level, will react preferentially to semiconducting SWCNTs.

1.1.3. Overview

In Chapter 2 of this thesis, we examine the limitations of reaction stoichiometry for controlling the covalent functionalization of carbon nanotubes with diazonium salts. There, a kinetic Monte Carlo simulation is employed to demonstrate that, due to the heterogeneous nature

of SWCNT suspensions, which can have as many as 30 different semiconducting species, alone[22], stoichiometry is insufficient for controlling the extent of covalent functionalization, and a large variance in the number of attached groups arises even at low conversions.

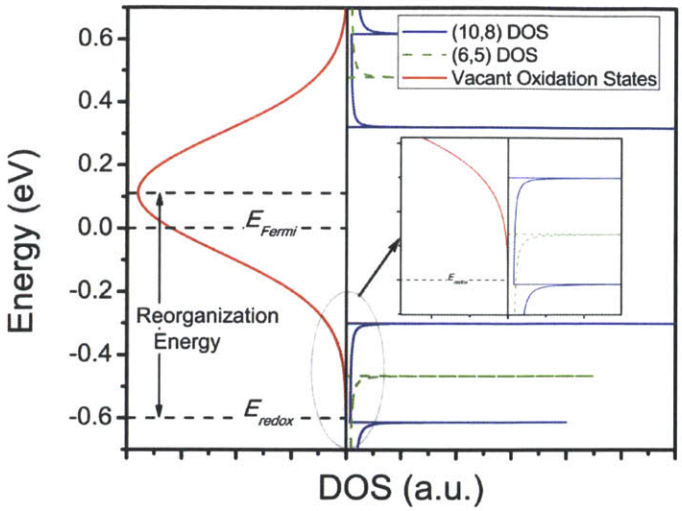

Figure 1.7 Densities of states for two semiconducting SWCNTs, evaluated using a tight-binding model. The degree of overlap between the occupied SWCNT states and the vacant states of the diazonium molecule (red), determine the rate of reactivity of the diazonium ion with the SWCNT sidewall. Reprinted with permission from reference [1]. Copyright 2011 American Institute of Chemical Engineers.

Then, in Chapter 3, we explore the ability to utilize the adsorbed surfactant layer to modulate nanotube reactivity in these reactions. There, it is shown that the adsorbed surfactant layer can influence the diazonium derivatization of carbon nanotubes in several ways, including electrostatic attraction or repulsion, steric exclusion, and direct chemical modification of the diazonium reactant.

1.2. Excited-State Electron Transfer: Developing Structure-Reactivity Relationships for SWCNT-Fullerene Heterojunctions

In Chapter 4 of this thesis, we synthesize a series of amphiphilic fullerene derivatives that are capable of dispersing carbon nanotubes in aqueous solution. Using these molecules, and SWCNT fluorescence measurements, we are able to deduce information about the driving force for electron-transfer from photo-excited SWCNTs to fullerenes as a function of both the SWCNT chirality and the nature of the employed fullerene derivative.

1.2.1 Motivation

Near-Infrared Light Harvesting Using SWCNT-Based Photovoltaics

Combining the entire spectral range of solar irradiance, in one hour, the earth receives enough solar energy to supply the energy demands of the world for an entire year[35]. The near-infrared region of the solar spectrum, which we define as occupying the range of 800 to 2500 nm, comprises 43% of the solar irradiance that hits the earth's surface. Therefore, if we can

develop an efficient means of capturing this energy range, nIR light harvesting would present a viable means of meeting the world's growing energy demands.

Commercially available, HiPCO single-walled carbon nanotubes possess E_{11} optical transitions between 875-1350nm (fig 1.8), which could be utilized for harvesting 56% of the nIR region of the solar spectrum, or 24% of the total solar irradiance. When combined with a suitable fullerene as an electron acceptor, such as a C_{85} methanofullerene, whose absorbance is depicted in Fig 1.8, a significant region of the visible spectrum can also be captured. In terms of SWCNT-based energy harvesting capability, assuming a cutoff of 1350nm for HiPCO SWCNTs is highly conservative, as other means of synthesizing carbon nanotubes, such as arc-discharge, can produce larger diameter species, extending the optical range of these materials to wavelengths of 1750nm or longer. Therefore, if we assume an effective optical collection range of $E_{11}^{(6,4)}$ = 875nm to $E_{11}^{(11,10)}$ = 1750nm to approximate solar harvesting capability, single-walled carbon nanotubes can potentially be utilized to harvest ~73% of the nIR spectral region. In addition to their broad spectral range, the photostability[36] and high carrier mobilities[37] of semiconducting SWCNTs make them promising materials for utilization in near-infrared harvesting photovoltaic devices.

Several efforts have been expended toward developing "all-carbon" photovoltaics[38-41], and it has recently been demonstrated that SWCNT-based photovoltaics outperform polymeric analogues in device lifetime measurements[39]. However, while a large body of work has been directed at fabricating SWCNT-based devices, little work has been expended toward elucidating the kinetics of electron transfer at the SWCNT-fullerene interface, and these studies have focused on photo-excitation of fullerene, rather than SWCNT[42, 43]. Such a study is beneficial, as a combination of factors, including morphology[39] and active-layer impurities[38], can limit the quantum efficiency of photovoltaic devices. This is

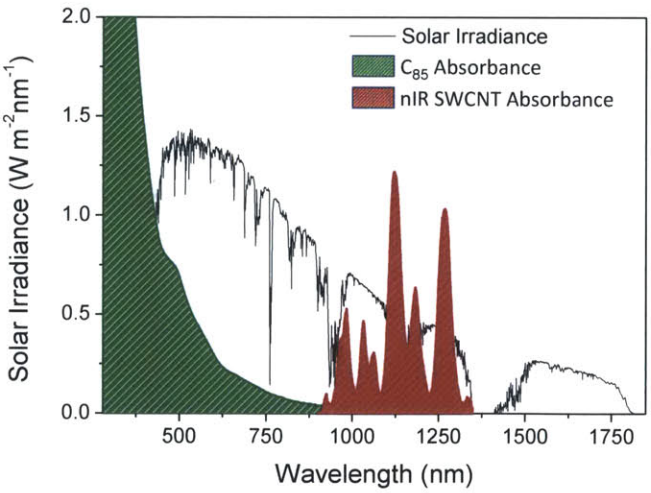

Figure 1.8 Solar irradiance spectrum depicting the wavelength range that could potentially be captured using commercially available HiPCO SWCNTs.

evidenced by the fact that the efficiencies of current, SWCNT-based active layer devices falls much lower than the theoretical value of 13% [39]. In addition, $PC_{60}BM$, which has frequently been used as an electron acceptor in polymer photovoltaics, is not an ideal electron acceptor for SWCNT-based solar cells, since the LUMO level lies close to the SWCNT valence band, and therefore, the SWCNT-fullerene heterojunction has been predicted to switch from type II to type I in going from SWCNT diameters of 0.9-1.3nm[39]. The same is true of $PC_{70}BM$, due to similarity in electronic structure. However, C_{84} has a deeper LUMO level than C_{60} and C_{70}[44], as well as a higher photostability[45], making it a potential candidate for SWCNT-based photovoltaics. Because of this, it is of interest to compare across different fullerenes and interfaces in order to optimize photoinduced electron transfer in the absence of complicating factors associated with device fabrication.

Label-Free Detection of Biological Macromolecules

In addition to photovoltaic devices, SWCNT-fullerene junctions hold potential for utilization in SWCNT fluorescence-based sensors. Fluorescence-based carbon nanotube sensors have demonstrated potential for utilization in the detection of a variety of small molecule analytes, including direct detection of nitric oxide[46, 47] and hydrogen peroxide[48], as well as indirect detection of sugars[49] and adenosine triphosphate [50]. However, in order to observe molecular adsorption events, it is necessary that the adsorbing molecule possess redox properties which are capable of modulating the nanotube fluorescence[51]. For the detection of proteins and other biomacromolecules, which do not have redox properties, ions near the nanotube surface have been utilized as an intermediate species in modulating nanotube fluorescence[52].

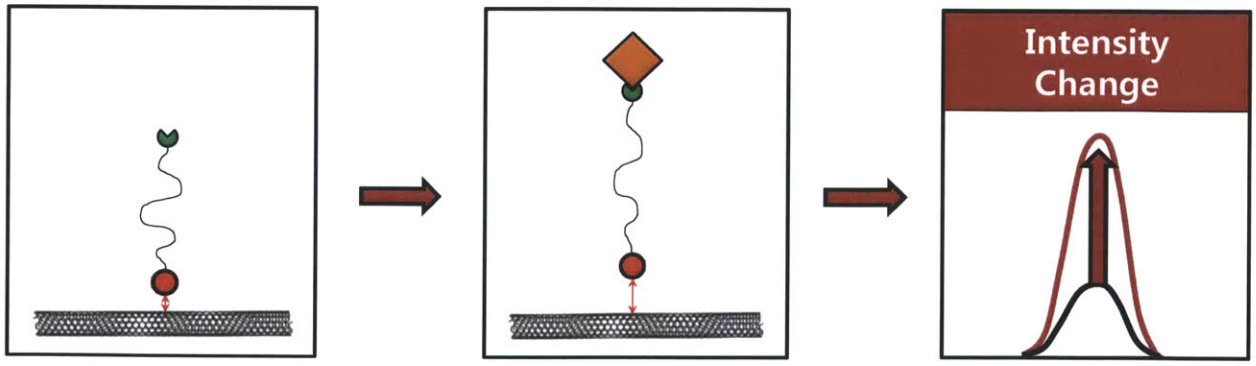

Figure 1.9 Schematic of a label-free protein detection scheme which takes advantage of the distance-dependence of excited-state electron transfer to a mediator species (red). Upon binding of an analyte, the distance of the mediator from the SWCNT is altered, resulting in fluorescence modulation.

However, the mechanism for signal transduction is not fully understood. In contrast, fullerenes are expected to interact with SWCNT by accepting excited-state electrons from the SWCNT conduction band, thereby quenching the SWCNT fluorescence signal. Because this process is distance dependent, it is possible that fullerenes could be employed as a proximity quencher for transducing protein-SWCNT interactions in fluorescence-based SWCNT sensors. Such a scheme is depicted schematically in Figure 1.9.

1.2.2 Background and Theory

A schematic of the photophysical properties of functionalized fullerenes is depicted in Figure 1.10 [53]. Under ambient conditions, most fullerene molecules will be in the lowest vibrational level of the ground state. Upon photoexcitation (processes 1 and 2), an electron can be promoted to higher energy states. After excitation, electrons that are promoted to energy levels greater than the lowest vibratational level of the first excited state will undergo a rapid, cascaded energy relaxation back to the first excited state, as shown in process (3). This generally occurs without emission of a photon. Once an electron has relaxed to the first excited state, the fullerene molecule can either return to any one of the vibrational levels of the ground state by fluorescent emission of a photon (process 4), or undergo intersystem crossing to the triplet state (process 5), which is followed by phosphorescent relaxation to the ground state. In pristine and monofunctional fullerenes, this intersystem crossing occurs with an efficiency that approaches unity[53].

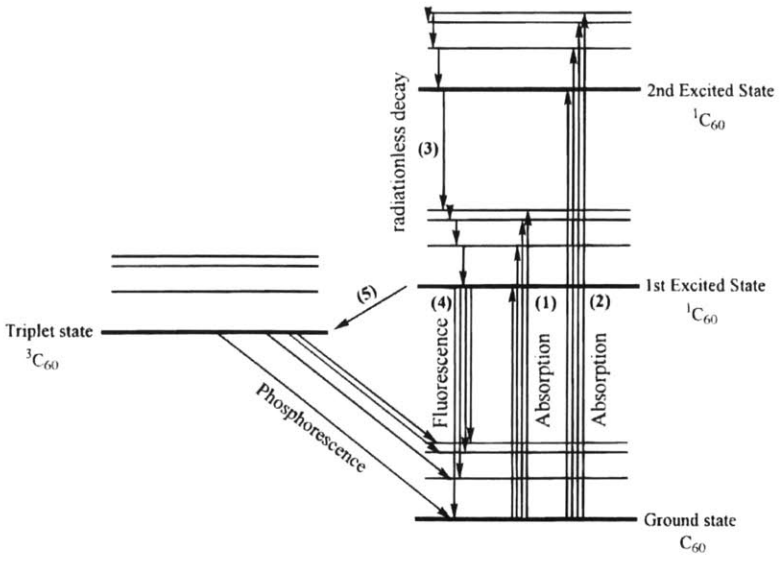

Figure 1.10 Electronic properties of functionalized fullerenes. Reprinted with permission from reference [53]. Copyright 1997 American Chemical Society

To date, there has only been a small body of work that examines electron transfer from SWCNTs to C_{60}-derivatives in non-covalent SWCNT-fullerene constructs[42, 43]. However, this work been directed at analyzing electron transfer from

ground-state SWCNT to photo- excited C_{61} (depicted in Scheme 1 of fig. 1.11). Therefore, while these studies provide useful information for incorporating C_{60} or its derivatives into the active layer of photovoltaic devices, they fail to address how to optimize photocurrent generation from photo-excited SWCNT (Scheme 2). This is because the triplet-state lifetime of C_{61}, in these manuscripts, is greater than 1000ps, allowing sufficient time for ground state electron transfer from SWCNT to fullerene, which occurs on the order of 150-250ps. In contrast, the excited-state of semiconducting SWCNT is extremely short-lived, relaxing to the ground state in less than 100ps[54]. Therefore, it is of interest to study the SWCNT-fullerene interface in order to optimize the electron transfer from photoexcited SWCNTs to C_{60} or its derivatives.

From an electron-transfer standpoint, while ground-state electron transfer from SWCNTs to an electron acceptor has been shown to require a Gerischer-Marcus theory treatment[32],

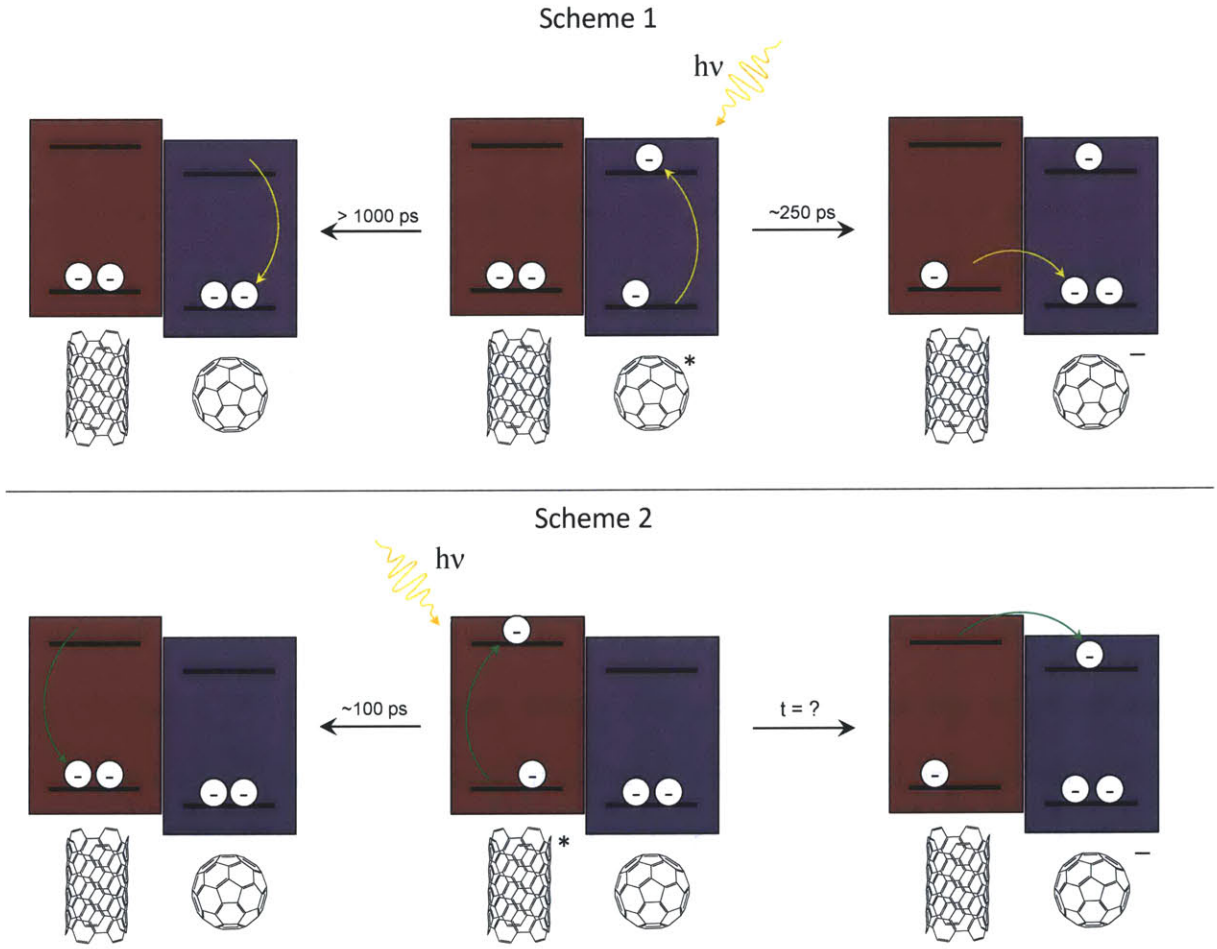

Figure 1.11 Schematic representation of electron transfer upon photoexcitation of fullerene (Scheme 1), and SWCNT (Scheme 2).

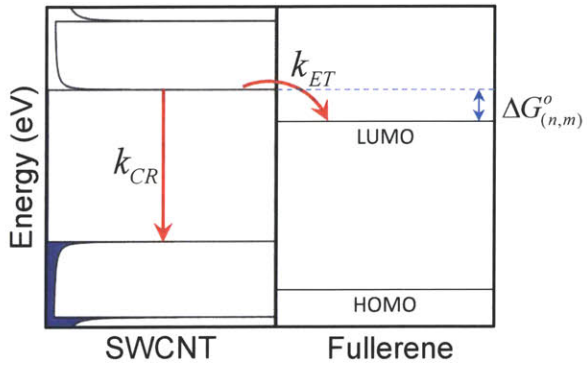

Figure 1.12 Schematic energy diagram of the SWCNT-fullerene interface. On the left is the DOS of a semiconducting SWCNTs, while the HOMO and LUMO levels of a fullerene electron acceptor are shown on the right. k_{ET} is the rate constant associated with electron transfer from excited-state SWCNT to the fullerene molecule, while k_{CR} is the rate constant associated with relaxation of the SWCNT excited state to the valence band.

which accounts for the one-dimensional band structure of carbon nanotubes by integrating over the occupied density of states, excited-state electron transfer is expected to be described by Marcus theory. This is because the relaxation of excited-state electrons to the edge of the conduction band is expected to occur on ultrafast time scales[6]. Therefore, upon excitation to higher states of the conduction band, the electron first relaxes to the E_{11} band edge, and is subsequently transferred to the fullerene acceptor. In such a case, only the energy offset between the LUMO level of the fullerene and the edge of the SWCNT conduction band is necessary for determining the driving force for electron transfer. A schematic for this excited-state charge transfer event is shown in Fig. 1.12.

According to Marcus theory, the rate constant associated with electron transfer from photo-excited SWCNTs to the LUMO level of fullerene can be represented as[55]:

$$k_{et} = \frac{2\pi}{\hbar\sqrt{4\pi\lambda k_b T}} V_R^2 \exp\left(-\Delta G^{\ddagger}_{(n,m)} / kT\right) = \frac{2\pi}{\hbar\sqrt{4\pi\lambda k_b T}} V_R^2 \exp\left(-\frac{\left(\lambda + \Delta G^{o}_{(n,m)}\right)^2}{4\lambda kT}\right) \qquad (1.4)$$

In which V_R^2 is an electronic coupling term between the initial and final states, λ is the reorganization energy, and $\Delta G^{o}_{(n,m)}$ is total change in Gibbs free energy for the electron transfer event. The electronic coupling term, V_R^2, decays exponentially as a function of the distance between the donor and acceptor species, and is often represented by: $V_R^2 = V_o^2 \exp(-\beta r)$ [55], where V_o^2 is the coupling between the two molecules in direct contact, and β is a constant that is medium-dependent. The exponential decay of this term enables the potential application of fullerene-SWCNT interfaces for label-free protein detection, as discussed in the previous section. The change in Gibbs free energy, $\Delta G^{o}_{(n,m)}$, is given by the energy difference between the SWCNT conduction band and the LUMO level of the methanofullerene:

$$\Delta G^{o}_{(n,m)} = -\left(E^{c_1}_{(n,m)} - E^{LUMO}\right) \tag{1.5}$$

If we assume that the electronic coupling term is invariant across nanotube species, relative rate constants of electron transfer can be evaluated as follows:

$$\left(\frac{k^{(n,m)}_{et}}{k^{(6,5)}_{et}}\right)_{theory} = \frac{\exp\left(-\Delta G^{\ddagger}_{(n,m)} / kT\right)}{\exp\left(-\Delta G^{\ddagger}_{(6,5)} / kT\right)} \tag{1.6}$$

where $-\Delta G^{\ddagger}_{(n,m)}$ is only dependent upon the reorganization energy of electron transfer and the energy offsets between the fullerene LUMO and the SWCNT conduction bands. SWCNT conduction band energies, referenced to the standard hydrogen electrode (SHE), have been reported in the literature for several chiralities[56], allowing direct utilization of these values for evaluating energetics of electron transfer. In addition, reorganization energies for fullerene-based electron transfer systems have previously been reported[57-60]. Therefore, if relative rate constants can be evaluated experimentally, the energetic driving force for electron transfer can be deduced.

1.2.3 Overview

In Chapter 4, we use SWCNT relative fluorescence quenching as a proxy for relative rate constants of electron transfer, and thereby deduce structure-reactivity relationships for electron transfer between photo-excited SWCNTs and fullerene acceptors. This is possible because, among competing excited-state decay pathways in SWCNT, the selectivity toward a particular pathway – in this case electron transfer to fullerene – will be proportional to the rate constant associated with that pathway, k_{ET}. Since energy transfer ultimately diverts an electron from the radiative decay pathway, fractional quenching results can be utilized as an approximation for the rate constant of electron transfer. If the fractional quenching is normalized to a particular chirality, such as (6,5), it is possible to approximate relative rate constants for electron transfer as:

$$\left(\frac{k^{(n,m)}_{et}}{k^{(6,5)}_{et}}\right)_{expt} = \frac{1-\left(I/I_o\right)_{(n,m)}}{1-\left(I/I_o\right)_{(6,5)}} \tag{1.7}$$

Using equations 1.6 and 1.7, it was possible to fit our Marcus theory model to experimental results, thereby deducing an effective LUMO level, E^{LUMO} for the fullerene derivatives employed

in the study. Using calculated values of E^{LUMO}, we were then able to assess the energetic driving force for excited-state electron transfer from photo-excited SWCNTs to fullerenes, as a function of the SWCNT chirality, using the equation: $\Delta G^{o}_{(n,m)} = -\left(E^{c_1}_{(n,m)} - E^{LUMO}\right)$.

1.3. Formation of High-Aspect Ratio Nanorods via Peptide-Driven Helical Self-Assembly of Fullerodendrimers

In Chapter 5 of this thesis, we examine the ability to design fullerene derivatives which organize into 1-dimensional supramolecular assemblies.

1.3.1. Motivation

The ability to self-assemble fullerene molecules into well-defined nanostructures is desirable for applications in polymer photovoltaics and organic electronics[61-64]. Fullerenes are excellent electron acceptors for utilization in organic solar cells[65], and have remained the electron-acceptor of choice since their usage in the first bulk-heterojunction photovoltaic, 18 years ago[66]. However, the ability to obtain high efficiency devices is highly dependent upon the morphology of the fullerenes molecules in the active layer[67, 68]. In particular, in order to maximize efficiency of bulk-heterojunction photovoltaics, it is desirable to form a donor-acceptor interface which possesses a large surface area while maintaining contiguous pathways for charge carrier extraction. Such an objective could be enabled by the development of donor or acceptor species which self-assemble into contiguous domains on the nanoscale.

In addition to photovoltaic applications, in organic electronics, confined arrays of C_{60} fullerenes have been shown to possess highly delocalized electronic states[69, 70], and superconducting properties have been observed in intercalated C_{60} networks[71-73]. Therefore, C_{60}-based electronics and photovoltaics could greatly benefit from controllable assembly and patterning of fullerenes.

1.3.2. Background

C_{60} fullerenes and their derivatives have been observed to assemble into a variety of structures, and reviews of fullerene assembly have recently been published[61, 74]. To date, the self-assembly of pristine C_{60} has been accomplished through a number of methods including liquid-liquid interfacial precipitation (LLIP), template-assisted drying, and drop drying[61]. In

addition to pristine C_{60}, functionalized fullerenes have been shown to form a variety of bilayer structures, the shape of which is dependent upon solvent conditions[74]. However, the dimensions of these assemblies are on the order of several hundred nanometers to a few microns. In contrast, only a few instances of nanometer-scale, high-aspect ratio fullerene assembles have been reported, and these have relied on surface-based assembly methods[75-78], including Langmuir-Blodgett techniques[75], or HOPG-driven self-assembly[76, 77], thereby limiting their scalability.

In order to develop one-dimensional, nanoscale fullerene assemblies, we utilized principles from the self-assembly of benzyl ether dendrons. The self-assembly behavior of these molecules is well established[79] with libraries of molecular and supramolecular architectures[80, 81]. A subset of these materials, which possess a dipeptide sequence at the dendron apex, has been shown to self-assemble into porous cylinders (d=0.9-1.3nm) which pack hexagonally in the solid state[82-86]. These pore diameters are ideally suited for interfacing with SWCNTs ($d \approx 0.8$-1.2nm). Previous benzyl dendron fullerene derivatives have been synthesized, but they have focused on either symmetric fullerene derivatives [87], which have dendritic components on either side of the fullerene, or dendritic fullerenes with a large aliphatic spacer between the fullerene and dendritic moiety[87-89]. These structures have been shown to form liquid crystalline phases, but lack the degree of structural order that has been observed for other benzyl dendrons and their derivatives[80-82]. Two potential reasons for this could be that: (1) the long, flexible linkers between the fullerene and the dendron make the molecules too labile for the formation of highly ordered domains, and (2) only dendrons with either very high, or very low, degrees of branching have been utilized to date. Based on these prior studies, we hypothesized that fullerodendrimers with a more compact, asymmetric, wedge-like configuration may be capable of organizing into 1-dimensional fullerene assemblies.

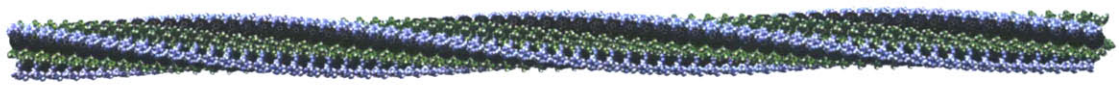

Figure 1.13 In organic photovoltaics, the development of donor or acceptor species which self-assemble on nanoscale dimensions could allow for the design of heterojunctions with large interfacial area, while maintaining contiguous pathways for charge carrier extraction.

1.3.3. Overview

In Chapter 5, we synthesize a novel pair of fullerodendrimers which self-assemble into one-dimensional fibers in cyclohexane. We find that high-aspect ratio fullerene nanorods, with diameters of 3.76 ± 0.52nm, can be formed by utilizing peptide-driven self-assembly. Atomic Force Microscopy (AFM) and Circular Dichroism (CD) measurements appear to indicate that these wires consist of interwoven, helical assemblies of peptidic methanofullerenes.

2 A Kinetic Monte Carlo Analysis for the Low Conversion Reactions of Single-Walled Carbon Nanotubes

2.2 Introduction

Singularly tethered nanoparticles – nanoparticles chemically derivatized with a single chemical chain or tether – are emerging as important from both a scientific and technological standpoint. In the past several years, this has primarily been driven by interest in quantum dots or plasmonic nanoparticles, which display interesting optical resonances when assembled into controlled dimers, trimers, or higher order assemblies[7]. Despite advances in spherical nanoparticle chemistry, analogous studies aimed at forming these types of structures using single-walled carbon nanotubes (SWCNTs) have not yet been demonstrated. This may partially be due to the fact that nanotube solutions are comprised of a wide distribution of chiral species[22], in some instances exhibiting substantially different affinities toward a reacting molecule[24, 91]. However, when combined with an appropriate functional handle, the singular tethering of carbon nanotubes may prove to be an effective means of separating them by electronic type while preserving their electronic structure. Therefore, it is of interest to study the conditions under which monofunctionalization of carbon nanotubes can be achieved.

In spherical nanoparticles, it has been found that the introduction of stoichiometric[8] or substoichiometric[9] quantities of ligands has allowed for the synthesis of well-defined nanoparticle assemblies, while excess ligation results in the formation of cross-linked aggregates[9]. Advances in the separation of such ligand-functionalized nanoparticles has led to the creation of hierarchical nanostructures containing a specific number of one[10] or more types of nanoparticles[11]. Building on this progress, Alivisatos and co-workers successfully utilized plasmonically coupled nanoparticles as molecular rulers[12] for monitoring the *in vitro* cleavage of DNA by EcoR enzymes[13] and the *in vivo* detection of caspase-3 activation[14]. In addition to spherical particle assembly, the directed end-to-end assembly of gold nanorods has been achieved by utilizing the different surface energies of their end and side facets[92]. However, similar advances have not been mirrored in the field of carbon nanotubes to date.

While the work is comparatively undeveloped, some effort has been expended toward controlling the density of functionalized sites on nanotube sidewalls. This has primarily been done by varying the degree of oxidative treatment for multiwalled[19] and single-walled[20] nanotubes. However, mild oxidative treatments typically involve the reflux of nanotubes in dilute acid, resulting in an absence of stoichiometric control over the extent of reaction. In addition, attached functionalities are primarily limited to carbonyl and carboxylic acid groups[93]. Perhaps the closest that researchers have come to creating sparsely functionalized SWCNT samples is through the monitoring of single fluorescence quenching events in single-walled carbon nanotubes immobilized in agarose gels[94, 95]. However, thus far, a method for the bulk production of singularly tethered nanotubes has not been developed.

When covalently functionalizing carbon nanotubes, there remains an incentive to keep the number of attached groups small, since sidewall functionalization significantly alters the electronic band structure of the nanotube. While thermal annealing has proven capable of driving off covalently attached groups, it has been found that such homolytic cleavage results in samples that are often difficult to re-disperse in solution. This may result from the cross-recombination of radicals during the annealing process, producing covalently crosslinked SWCNT samples[96]. With singular-tethering, this problem is avoided by minimizing the number of covalent attachments.

The application of such a technique to nanotube separation is particularly relevant. In the past, separation of carbon nanotubes has been demonstrated using a variety of methods[97], including density gradient ultracentrifugation[98, 99], selective dispersion[100], dielectrophoresis[101, 102], DNA-assisted ion-exhange chromatography[103, 104], and selective chemistry[96, 105]. However, while some of these approaches have succeeded in enriching certain SWCNT species[99, 103], or metallic and semiconducting fractions[96, 101, 102, 105], many of them remain limited to lab-scale separation. Because species-selective chemistries are most effective at low conversions, combining single-particle tethering with an appropriate functional handle may hold particular promise for the scaled separation of carbon nanotubes by electronic type.

In this work, we examine the reaction conditions required to maximize the number of singularly tethered species for several cases of homogeneously dispersed nanoparticles. We start by examining the case of a monodisperse sample of equally reactive particles of identical size.

We then build complexity by allowing the solution to have a variety of particles possessing different sizes and rate constants. In order to do so, we utilize the electron-transfer reactions of single-walled carbon nanotubes as a model system. Finally, we look at how the initial distribution of rate constants in solution, and changes in site reactivity due to covalent functionalization, affect the maximum obtainable fraction of monofunctional particles. In each case, we examine how changes in model complexity affect the variance in the number of particles attached.

2.3 Results and Discussion

Case I: Equal Size and Site Reactivity

If each particle contains the same number of sites, and all sites are both independent and equally reactive, the reacting sites will be indistinguishable, and the distribution in the number of attached groups, as a function of conversion, can be predicted by a simple binomial distribution[106]:

$$\Pr(X = x) = \binom{n}{x} p^x (1-p)^{n-x} = \frac{n!}{x!(n-x)!} p^x (1-p)^{n-x} \tag{2.1}$$

Here, n represents the number of sites on the nanoparticle, p represents the constant probability that each particular site is reacted, and Pr is the probability mass function associated with observing x reacted sites. Because all reactive sites are independent and indistinguishable, p is simply given by the conversion of the reacting system. Within the probability mass function, the expectation value and variance are described by:

$$E(X) = np \tag{2.2}$$

$$Var(X) = np(1-p) \tag{2.3}$$

Therefore, the binomial distribution, shown as a curve in Fig. 2.1, informs us that there is a clear maximum in the number of x-functional particles that can be achieved, and that the variance in the number of attached groups goes to a minimum as we approach the limit of sparse functionalization. For the specific case of monofunctionalized nanoparticles, $E(X) = 1$ and $p = 1/n$, with the maximum fraction of monofunctional particles given by:

$$\Pr = \left(1 - \frac{1}{n}\right)^{n-1} \tag{2.4}$$

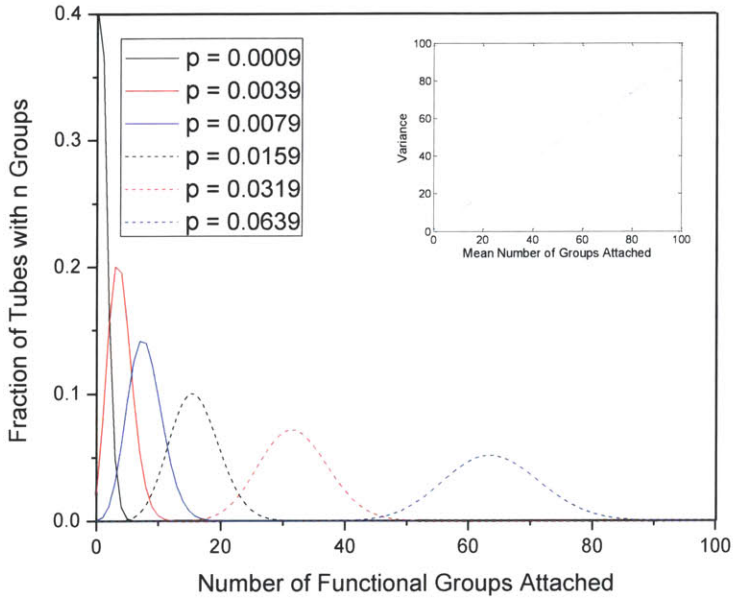

Figure 2.1 Binomial probability distributions for the number of attached groups at six different conversions, p, for n = 1000. The inset depicts the variance in the number of attached groups as a function of the mean number of groups attached.

If all particles possess the same number of reactive sites, as is approximately the case for monodisperse samples of spherical nanoparticles, the binomial distribution predicts that the maximum number of singularly tethered nanoparticles will be obtained when the ligand and nanoparticle populations are stoichiometrically equal. While this formalism is useful for understanding simple kinetic systems, it loses validity as variability is introduced in both particle size and reactivity. For these cases, a more complex model becomes necessary.

Case II: Distinguishable Particles and Changes in Site Reactivity

Additional degrees of complexity are introduced as particles are allowed to possess both different sizes and reactivities, as well as when the activity of reactive sites can change on the basis of nearby functionalization. In these cases, it is impossible to predict the conditions under which monofunctionalization is achieved by stoichiometry, alone. Because they can be comprised of a variety of species with disparate electronic properties, nanotube solutions provide a useful system with which to analyze this case, especially in the case of electron transfer reactions.

(a) Model Construction

Carbon nanotubes have been shown to participate in electron transfer chemistries via a two-step mechanism in which the nanotube and reacting molecule form an intermediate charge transfer complex[30, 31]. The reaction network can be described by:

$$A + \theta_{(n,m)} \xrightarrow{k_A^{(n,m)}} A_{ads}\theta_{(n,m)} \xrightarrow{k_R^{(n,m)}} A\theta_{(n,m)} \tag{2.5}$$

where A represents a generic electron acceptor and $\theta_{(n,m)}$, $A_{ads}\theta_{(n,m)}$, and $A\theta_{(n,m)}$ represent vacant nanotube sites, adsorbed sites, and covalently reacted sites, respectively. Former kinetic studies by Nair et. al. [32] have shown that, under certain reaction conditions, the reaction rate of this system can be described by second order kinetics:

$$\frac{d\theta_{(n,m)}}{dt} = k_A^{(n,m)} A \cdot \theta_{(n,m)} \tag{2.6}$$

with the relative rate constants of all nanotubes being evaluated using Gerischer-Marcus theory[33]. This theory is applicable for kinetic networks in which the rate-limiting step involves electron transfer between reacting species. Insights into the applicability of G-M theory to these electron-transfer reactions have been recently provided through computational studies[34]. In that work, it was shown that for diazonium reactions, the counterion (BF_4^-) plays an integral role by actively competing with SWCNT as a source of electron density for stabilizing the diazo cation. Because of this, the ability of the nanotube to donate electron density, and therefore, the nanotube density of states, is highly important. Gerischer-Marcus theory predicts that the rate of reaction between a carbon nanotube and an electron acceptor molecule is proportional to the degree of overlap between the SWCNT density of states, $DOS_{(n,m)}$, and the distribution of oxidized states for the molecule in solution, W_{ox}[33]:

$$k_{ET}^{(n,m)} = \upsilon_n \int_{E_F^D}^{E_F^{SWNT}} \varepsilon_{ox}(E) DOS_{(n,m)}(E) W_{ox}(E) dE \tag{2.7}$$

If the proportionality function, ϵ_{ox}, is assumed to be independent of energy, and both v_n and ϵ_{ox} are taken to be independent of nanotube chirality, it follows that the two terms can be cancelled during the evaluation of relative rate constants. In this work, all rate constants were evaluated relative to the (11,5) nanotube. The distribution of oxidized states for the solvated species is given by[107]:

$$W_{ox}(E) = \frac{1}{\sqrt{4\pi\lambda kT}} \exp\left(-\frac{(E-(E_{redox}+\lambda))^2}{4\lambda kT} \right) \tag{2.8}$$

In this equation, λ is the reorganization energy required for electron transfer to take place and E_{redox} is the Fermi level of the redox molecule in solution. We assign a value of λ = 0.71 eV for our electron transfer chemistry, which has been formerly determined for the diazonium-functionalization of carbon nanotubes using 4-hydroxybenzene diazonium salt[32]. Ensuring consistency with our previous study, we have assigned a redox potential of 0.35 eV (SCE) to the

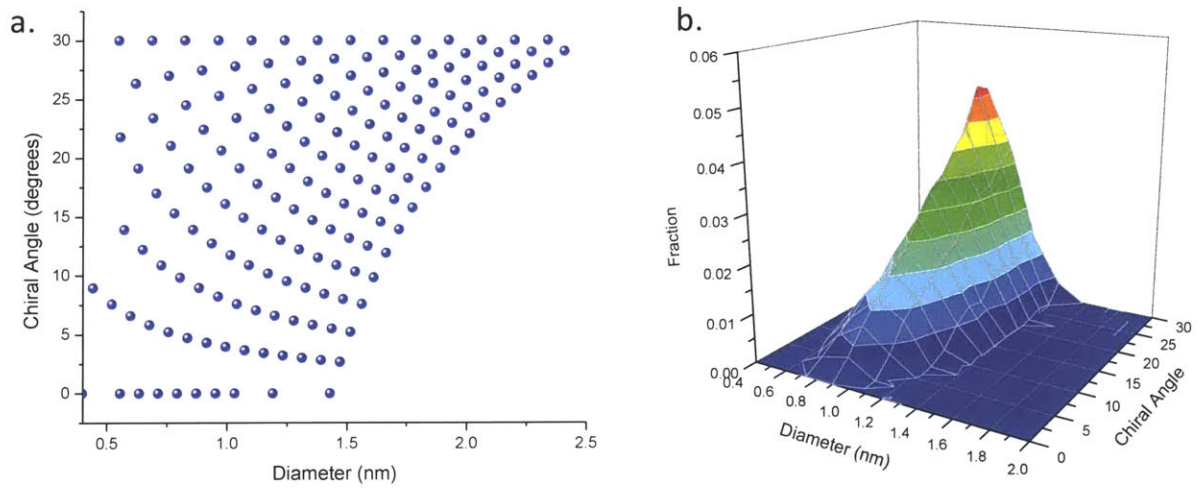

Figure 2.2 (a) Distribution of nanotubes for which density of states and relative rate constants were evaluated. (b) Interpolated surface plot showing the SWCNT composition for a typical HiPCO solution used during a simulated reaction.

redox species and a constant nanotube work function of $W_{SWNT} = 4.45$ eV. Defining the Fermi level of SWCNT to be the zero energy in the DOS, the redox potential of reacting molecule, relative to the SWCNT energy axis, becomes $E_{redox} = -0.6$. By adjusting the redox potential of the reacting molecule, it is possible to apply this same model to a variety of redox-active species.

In the limit of sparse functionalization, the reaction kinetics will be inherently stochastic. Therefore, the kinetic Monte Carlo algorithm proposed by Gillespie was employed[108]. In this algorithm, a random number is used to determine which site reacts, based on the assigned site probabilities:

$$P_{site} = \frac{k_{site} N_A}{\sum_i k_i N_{\theta,i} N_A} = \frac{k_{site}}{\sum_i k_i N_{\theta,i}} \tag{2.9}$$

where k_{site} is the rate constant associated with the site under consideration, N_A is the number of redox-active molecules, and the denominator sums over the kinetics associated with all sites in solution (note that $N_{\theta,site} = 1$, and is omitted from the numerator). In order to monitor the reaction progress, a conversion was defined based upon the total initial number of carbon atoms:

$$\chi = \frac{N_{\theta,o} - (N_{\theta,o} - N_{A\theta})}{N_{\theta,o}} = \frac{N_{A\theta}}{N_{\theta,o}} \tag{2.10}$$

In this equation, $N_{\theta,o}$ is the initial number of carbon atoms in solution, and $N_{A\theta}$ is the number of reacted sites. In the Gillespie algorithm, a second random number can also be used to evaluate

the time evolution of the reacting system. However, this paper uses conversion exclusively, and so a discussion on the time evolution of the system is omitted.

In order to simulate the reaction of a random solution of nanotubes, the density of states for 170 species were evaluated using a 3rd nearest neighbor tight binding model[4, 109] and a universal density of states for one-dimensional systems[110]. The distribution of evaluated nanotubes is depicted in fig. 2.2(a) as a function of diameter and chiral angle. For each simulation, a nanotube solution was randomly generated based upon a HiPCO suspension. To do this, we assumed a linear dependence on chiral angle[111] and a log-normal diameter distribution with a mean, $\mu_d = \ln(0.906)$ and standard deviation (σ_d) of 0.160[112]:

$$f(x) = \frac{1}{\sqrt{2\pi}\sigma_d D} \exp\left(-\frac{(\ln D - \mu_D)^2}{\sigma_d} \right) \tag{2.11}$$

A typical solution composition, based upon these parameters, is depicted in fig 2.2(b). For each nanotube, a tube length was chosen based upon a log-normal distribution with a mean (μ_d) of 6.24 (512.9 nm) and standard deviation (σ_d) of 1.0[113].

In order to track the reactivity of each site on the nanotube, a lattice model was developed by utilizing the fact that any chirality of nanotube can be constructed by rolling a zigzag (or armchair) graphene nanoribbon into a cylinder, and connecting the edge carbons with some axial dislocation vector[111]. The formalism for constructing a nanotube in this manner is depicted in fig. 2.3 for a zigzag nanoribbon. For constructing a matrix of reactive sites, each row of zigzag carbons along the length of the nanoribbon translate to a row of the reaction site matrix and each carbon along the uppermost row defines a column of the corresponding site matrix. Utilizing this formalism, an X by Y site matrix belonging any (n,m) nanotube can be constructed with the dimensions specified by:

$$X = n + m \tag{2.12}$$

$$Y = \frac{L_{SWNT}}{a} \cdot \frac{N_c}{(n+m)} \tag{2.13}$$

and a carbon-carbon connectivity of $m - n$ for alternating atoms along the zigzag edge (fig. 2.3). In the equation for Y, L_{SWNT} represents the length of the nanotube, a is the translational period of the nanotube, and N_c is the number of carbons per unit cell.

When a site on a nanoparticle reacts, it is possible for there to be changes in nanoparticle reactivity due to steric effects, electrostatic repulsion, or changes in electronic structure. For

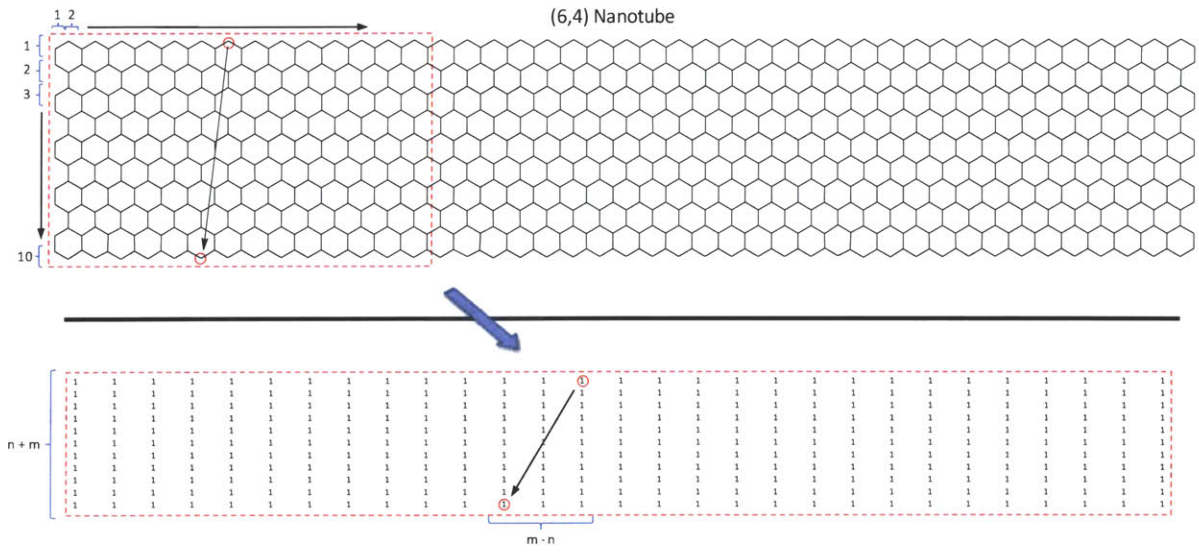

Figure 2.3 Example of the transformation from nanoribbon representation to reactive-site-matrix for a (n,m) = (6,4) nanotube. The number of rows in the site matrix is equal to n + m with the edge connectivity being defined by m - n for alternating carbons along the nanoribbon edge. The number of columns is determined by the tube length (see text).

electron transfer reactions involving carbon nanotubes, changes in site reactivity are likely to be primarily due to modifications to the nanotube density of states, which will alter the overlap integral in the Gerischer-Marcus formalism. In order to estimate the effects of functionalization on the nanotube density of states, we utilized theoretical band structure data for carboxylated (10,0) and (8,8) nanotubes[2]. The evaluated band structures of the functionalized and unfunctionalized tubes are depicted in fig. 2.4. As can be seen from the figure, covalent functionalization introduces a half-occupied impurity state near the Fermi level of the pristine nanotube[2]. Because band structure data is not available for all of the nanotubes utilized in this study, the effects of functionalization on other species had to be inferred from the (10,0) and (8,8) nanotubes. This was done by assuming that the characteristics of the impurity state primarily result from the attached molecule and the nanotube electronic type (metallic or semiconducting), rather than the specific chirality of the tube. Therefore, the impurity state of all metallic species could be inferred from the (8,8) nanotube, and that of semiconductors from the (10,0) species. To do this, the non-normalized DOS for the impurity states of the (10,0) and (8,8) nanotubes were evaluated and then normalized, on a per atom basis, according to the unit cell of each nanotube species used in this study. The impurity states were then inserted into the DOS of the corresponding, pristine nanotubes. For all semiconducting species, the DOS of functionalized nanotubes were predicted by introducing a normalized, half-occupied impurity

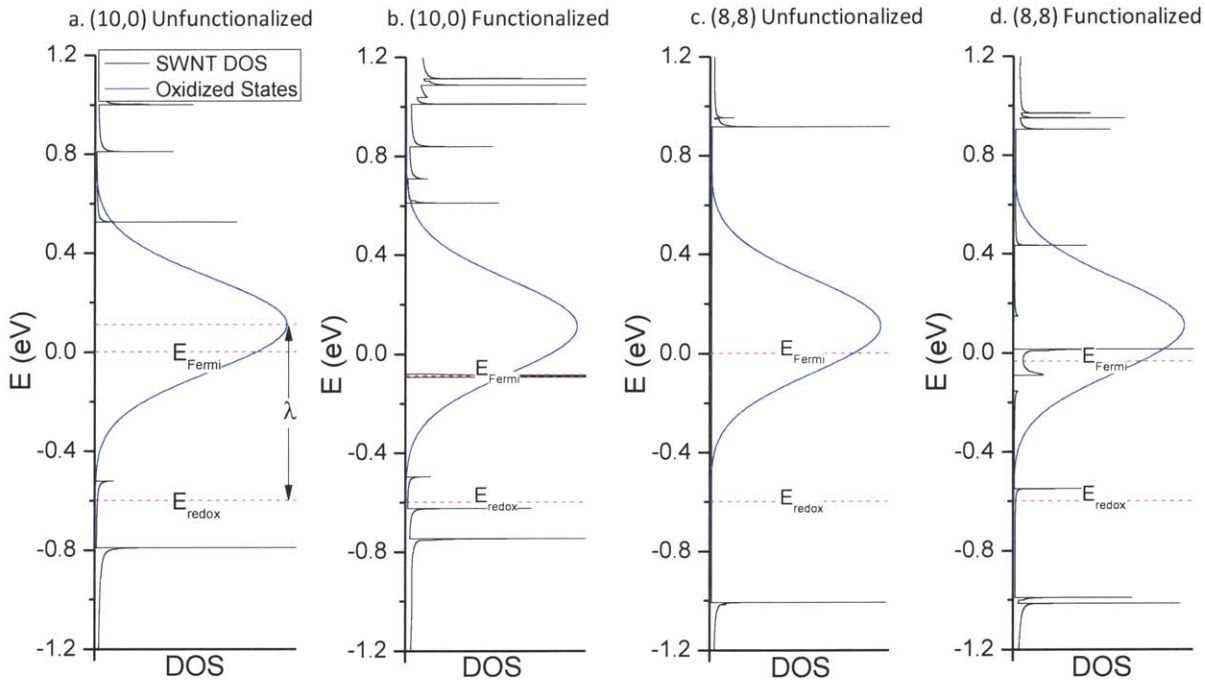

Figure 2.4 Initial and modified densities of states for (10,0) and (8,8) nanotubes evaluated using the results of DFT calculations[2]. E_{redox} and E_{Fermi} are depicted for each nanotube, and the reorganization energy associated with electron transfer is shown in (a).

state centered at -0.09 eV. For metallic species, an impurity state was introduced as well as a gap in the DOS from -0.15 to -0.09 eV. While changes to the nanotube electronic structure occur in addition to the induced impurity state, these changes account for less than 1% of the predicted changes in nanotube reactivity for both the (10,0) and (8,8) nanotubes, and were neglected for all species. For reacted nanotubes, it has been shown that the impurity state wavefunction is relatively localized around the reaction site in semiconducting tubes, with a characteristic length of approximately 1.5 nm, but delocalized along a distance of at least 4 nm in metallic species. In this work, we assume that the semiconducting impurity wavefunction decays with distance according to a gaussian distribution with a standard deviation of 0.7 nm. Due to lack of further knowledge of the extent of delocalization in metallic species, we conservatively estimate that the wavefunction extends along approximately 4.5 nm of the longitudinal axis in the nanoribbon representation.

(b) Results

Using this formalism, we performed kinetic Monte Carlo simulations for solutions of nanotubes synthesized using the HiPCO approach[114]. For these solutions, we analyzed two

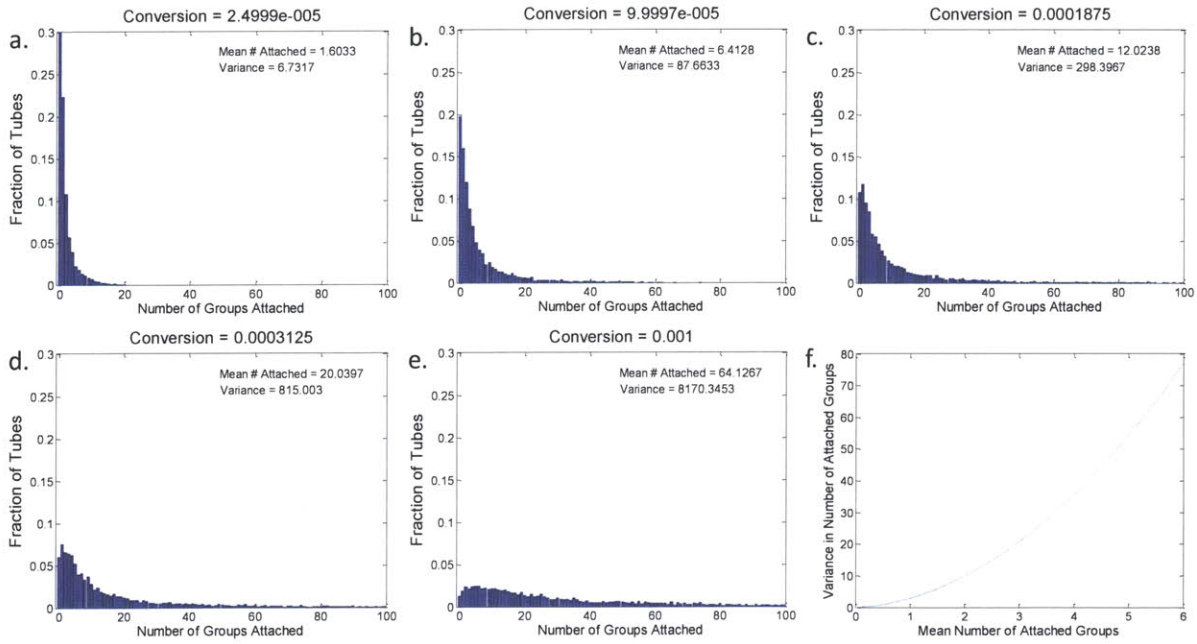

Figure 2.5 (a-e) Distributions in the number of functional groups attached for five selected conversions. The mean number of groups attached and variance in the number of groups attached are provided for each plot. (f) Depicts the relationship between the variance in the number of attached functional groups and the mean number of attached groups.

cases in which: (1) no site reactivities were adjusted, and (2) adjacent site reactivities were adjusted as described in the section on model construction. For unadjusted reactivities, the averaged results of 10 simulations, each containing 5000 nanotubes, are depicted in figs. 2.5 and 2.6. As was shown for the binomial distribution, figures 2.5(a)-(e) depict the distributions in the number of functional groups attached for five selected conversions. From the data, we also calculated the variance in the number of attached groups as a function of the mean number of groups attached (fig. 2.5(f)). Compared to the binomial distribution, the variance of the more complex system increases much more rapidly, growing proportional to the square of the mean number of groups attached, rather than linearly at low functionalization. Here, it should be noted that the mean number of functional groups attached is linearly proportional to the conversion, so that a plot of the variance versus the conversion results in a similar trend. In addition, the maximum fraction of monofunctional tubes is not achieved at the same conversion that results in an average number of functional groups equal to unity, convoluting stoichiometric considerations. The fractions of mono- and bifunctional tubes are depicted in fig. 2.6(a) as a function of conversion. For monofunctional tubes, a maximum fraction of 0.224 ± 0.006 is achieved at a conversion of 2.25×10^{-5}, while a maximum fraction of 0.128 ± 0.004 is obtained for bifunctional tubes at a conversion of 5.50×10^{-5}. Conversely, considering a solution of (7,6)

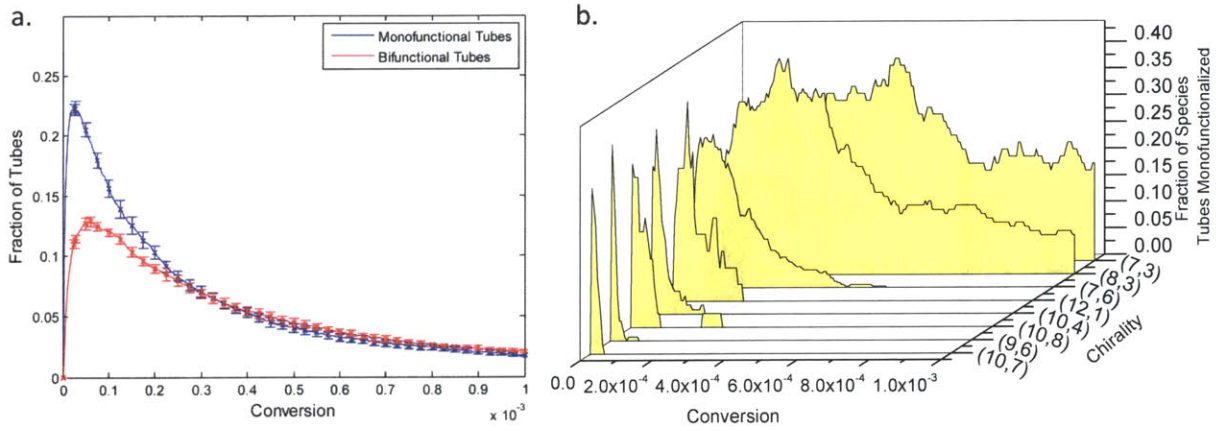

Figure 2.6 (a) Total fractions of mono- and bifunctional tubes as a function of conversion. (b) Monofunctional species fractions for eight selected chiralities as a function of conversion.

nanotubes, 500 nm in length, the binomial distribution predicts a maximum obtainable monofunctional fraction of 0.37. The deviation from this idealized value results from the distribution of rate constants in solution, which leads to different species attaining their maximum fraction of monofunctional tubes at different conversions. This effect is depicted in fig. 2.6(b) for eight species of nanotubes arranged from high to low reactivity.

Because of this effect, it was of interest to examine how the distribution of rate constants in solution affects the variance in the number of attached groups. In addition, we examined how the variance is affected by changes in adjacent site reactivity. To do this, we performed KMC simulations for SWCNT synthesized by three different approaches: HiPCO, Co-MCM-41[115, 116], and a scaled version of the floating-catalyst method (FC-CVD)[117, 118]. For each case, the simulations were performed both with and without modifying adjacent site reactivity. As was done for HiPCO, a linear dependence on chiral angle was assumed for both Co-MCM-41 and FC-CVD SWCNT. For Co-MCM-41, we assumed a log-normal distribution in diameter with a mean, $\mu_d = \ln(0.834)$ and standard deviation (σ_d) of 0.052[112], while for FC-CVD SWCNT, a Gaussian distribution was assumed with a mean diameter of 1.3 nm and a standard deviation of 0.2 nm [118]. The simulation results are depicted in fig. 2.7. As expected, a solution containing a more disparate rate constant distribution results in a higher variance in the number of functional groups attached. In addition, there is little change in the variance when modifications to site reactivity are accounted for.

The fact that adjustments in adjacent-site reactivity produce little effect on the variance in the number of attached groups is consistent with expectations, since in the early stages of the

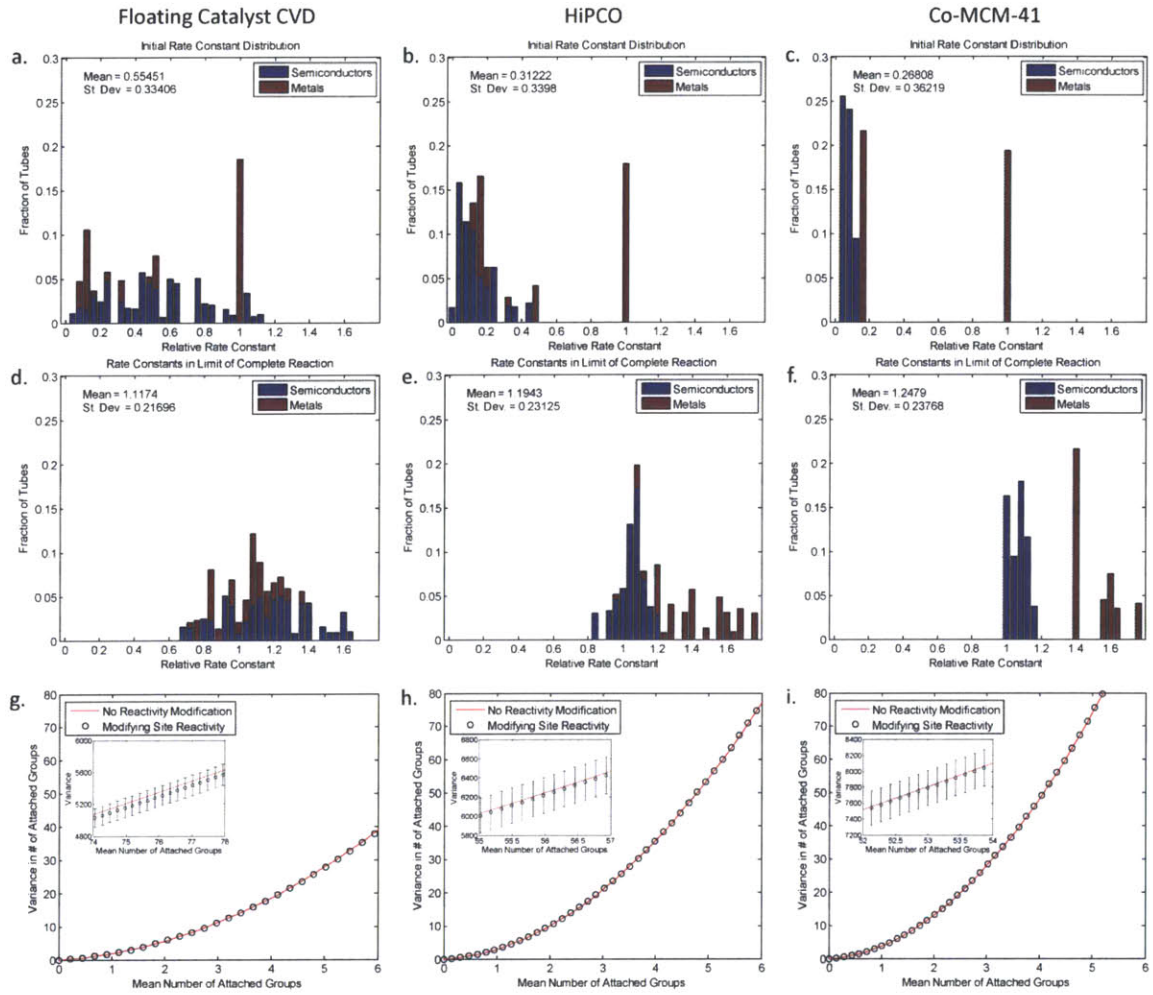

Figure 2.7 Effect of rate constant distribution on the variance in the number of attached groups, with columns corresponding to FC-CVD, HiPCO and Co-MCM-41 SWCNT, respectively. (a-c): Rate constant distributions of pristine SWCNTs. (d-f): Rate constant distributions in the limit of complete reaction. (g-i): Variance in number of functional groups attached (as a function of mean groups attached) for the cases of unmodified and modified site reactivities.

reaction, the kinetics of reaction are predominantly determined by the vast majority of unfunctionalized sites. In a kinetic system, the relative probability of a particular tube reacting can be described by:

$$P_i = \frac{\sum_i k_i N_{\theta,i} N_A}{\sum_j \sum_i k_{ij} N_{\theta,ij} N_A} = \frac{\sum_i k_i N_{\theta,i}}{\sum_j \sum_i k_{ij} N_{\theta,ij}} \tag{2.14}$$

where the numerator sums over all the sites of a single nanoparticle, and the denominator sums over all nanoparticles in solution. If the effect of reacting a particular site is relatively small, the values in the numerator and demominator will change little upon the addition of a small number of functional groups, and the equation for P becomes:

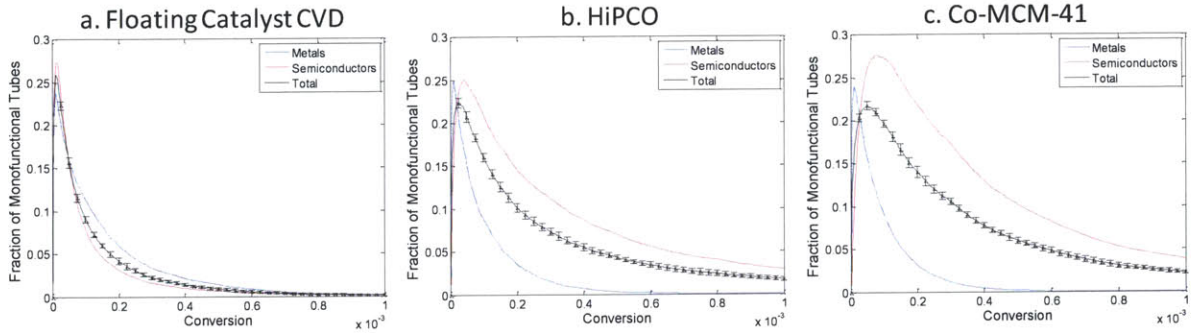

Figure 2.8 Fraction of monofunctional tubes as a function of conversion for three different nanotube solutions, along with the monofunctional fractions of both metallic and semiconducting species.

$$P_i = \frac{k_{i,o} N_{\theta_o,i}}{\sum_j k_{j,o} N_{\theta_o,j}} \tag{2.15}$$

or that the probability of each tube reacting will remain approximately constant at early reaction times. Therefore, there is minimal deviation from the unmodified reactivity case in the limit of low conversion. However, while the result is not statistically significant in the functionalization range examined here, we do expect the variance to exhibit slightly different trends, at high conversions, for the cases of modified and unmodified site reactivity (see fig. 2.7(g-h) insets). In particular, we expect the variance in the number of attached groups to increase more slowly for the case in which modified site reactivity is accounted for. This is due to the fact that the rate constants of the species in solution nanotube tend to converge upon reaction (see figs. 2.7(a-f)). In general, it is expected that reactions which serve to converge the rate constant distribution of the particles will also decrease the variance in the number of attached groups relative to the unmodified case, and vice versa. An extreme of this is the case in which all rate constants converge to zero upon the first chemical reaction, resulting in a sample that is almost entirely monofunctionalized[119]. Because there is little change in the variance of the system, identical maxima are attained for the total fraction of monofunctional HiPCO tubes both with and without site reactivity modification (see Table 2-1). Therefore, we instead focused on how the distribution of the initial rate constants affects the maximum fraction of monofunctional tubes obtained.

In fig. 2.8, we depict the fraction of total monofunctional tubes as a function of conversion for all three nanotube solutions. In addition, because the deviations in the initial rate constants are primarily due to metallic and semiconducting species, we plot the monofunctional fractions of both these electronic types. As can be seen from the plots, and the summarized data

Table 2-1 Conversions at which maximum fractions of monofunctional nanotubes are obtained for four cases analyzed.

		No Site Adjustment	Adjusting Site Reactivity		
		HiPCO	FC-CVD	HiPCO	Co-MCM-41
Monofunctional Tubes	Conversion	2.25×10^{-5}	1.00×10^{-5}	2.25×10^{-5}	5.00×10^{-5}
	Maximum	0.224 ± 0.006	0.260 ± 0.004	0.224 ± 0.006	0.218 ± 0.005

in Table 2-1, the maximum fraction of monofunctional tubes decreases as the standard deviation of the initial rate constant distribution increases. This should be expected for all reacting solutions in which the particles possess a distribution of rate constants. In addition, as the rate constants of semiconducting and metallic species become more disparate, the conversions at which the maximum fractions of these species are reached begin to separate. This led us to look at the implications of solution composition on the ability to use electron transfer chemistries to separate nanotubes by electronic type.

(c) Applied Example: Using Singular Tethers to Separate SWCNTs by Electronic Type

For the purpose of using selective chemistry to separate single-walled carbon nanotubes by electronic type, it is desirable to limit the number of functionalized sites in order to preserve the nanotube electronic structure. Since electron transfer chemistries have been shown to be selective to metallic nanotubes, we examined the ability to use these chemistries for metal/semiconductor separation with the three solutions utilized in this study. For each of these solutions, the typical nanotube composition with respect to electronic type is provided in Table 2-2. For this work, large band -gap semiconductors were defined as those having E_{11} greater than 1 eV, while all others were considered small band-gap.

The averaged results of ten simulations, using the model which incorporates site-reactivity modifications, are shown in fig. 2.9. In these plots, the "metallic solution" refers to a solution of functionalized nanotubes, which are assumed to be separable from the unfunctionalized "semiconducting solution." From fig. 2.9, our KMC simulations show that the ability to use electron-transfer chemistry to separate nanotubes by electronic type is strongly dependent on the distribution of nanotubes in solution, with the greatest degree of separation being achieved using Co-MCM-41 SWCNT. This results from the presence of entirely large band-gap semiconductors, which have low rate constants due to the small degree of overlap between the SWCNT density of states and the oxidized states of the redox molecule. As more small-band gap semiconductors are introduced in HiPCO and FC-CVD SWCNT, the ability to

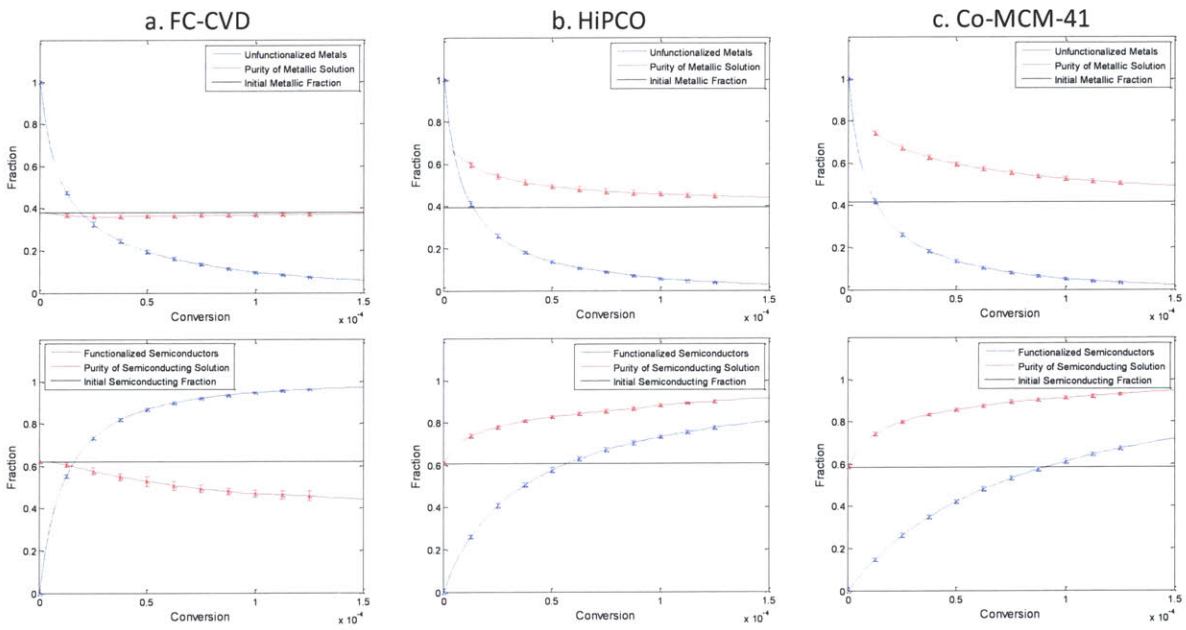

Figure 2.9 Implications of chiral distribution for nanotube separation. Because electron transfer chemistries are typically selective toward metallic species, the functionalized sample has been denoted as the "metallic solution," while the unfunctionalized sample has been labeled as the "semiconducting solution."

separate tubes by electronic type decreases due to the increased reactivity of the semiconducting species. In the extreme of FC-CVD SWCNT, no degree of enrichment is obtained for semiconducting or metallic nanotubes. For these tubes, the observed deviation in the purity of the semiconducting solution, from initial composition, can be attributed to the fact that as the number of unfunctionalized tubes decreases to zero, small variations the number of semiconducting or metallic tubes will result in significant deviations in the fraction of semiconductors present. Considering the conditions for optimizing the number of monofunctional metallic tubes, it was determined that for HiPCO, metallic and semiconducting purities of 61.5 ± 1.2% and 72.3 ± 1.0% can be obtained with losses of 46% and 23% of the metallic and semiconducting tubes, respectively. For Co-MCM-41 SWCNT, purities of 75.9 ± 1.2% and 72.4 ± 0.7% can be obtained for metals and semiconductors with losses of 47.2% and 12.0%. By carrying the reactions out under these conditions, it may therefore be possible to obtain enriched samples of semiconducting and metallic species with minimal damage to the

Table 2-2 Compositions of nanotube solutions used for KMC simulations.

Nanotube Type	Metals	Small Band-Gap Semiconductors	Large Band-Gap Semiconductors
Floating Catalyst CVD	0.373 ± 0.007	0.611 ± 0.007	0.016 ± 0.002
HiPCO	0.384 ± 0.008	0.290 ± 0.006	0.325 ± 0.003
Co-MCM-41	0.414 ± 0.009	0.000 ± 0.000	0.586 ± 0.009

nanotube electronic properties.

2.4 Conclusions

In this study, we analyzed the conditions under which singularly-tethered nanoparticles can be achieved. For simple systems, such as the ligation of monodisperse, spherical nanoparticles, the results of reaction can be predicted by a statistical binomial distribution. This leads to the conclusion that a stoichiometric addition of ligand results in the greatest number of singularly-tethered particles. However, for systems in which the solution contains a heterogeneous dispersion of different types of nanoparticles, each possessing a different reactivity, a simple statistical analysis no longer suffices. We examined this more complex system using carbon nanotubes as a model system, and add a further degree of complexity by incorporating the effects of covalent reaction on the reactivity of adjacent carbons. We found that the variance in the number of attached groups increases much more rapidly in these complex systems, making it more important to operate at low conversions in order to obtain samples with monodisperse degrees of functionalization. In addition, the maximum attainable fraction of monofunctional particles is strongly dependent upon the distribution of rate constants in the initial solution, with the fraction increasing for samples in which the standard deviation of the initial rate constant distribution decreases. We then examined the implications of the nanotube distribution on the ability to use selective electron-transfer chemistries to separate nanotubes by electronic type. Based on the kinetic parameters used in this study, there appear to be upper limits on the purity of semiconducting and metallic fractions that can be obtained. This purity was found to be highly dependent on the initial distribution of nanotubes in solution, with Co-MCM-41 SWCNT appearing the most promising for separation of carbon nanotubes by electronic type. Fundamentally, this study shows that, due to the heterogeneous population of SWCNT rate constants in solution, simple stoichiometric considerations are not sufficient for obtaining a large population of carbon nanotubes which possess a minimal number of covalent tethers. Because of this, we explore the ability to utilize the surfactant adsorbed layer to impart an additional degree of control over SWCNT covalent reactions in colloidal dispersions of single-walled carbon nanotubes.

3 The Role of Adsorbed Surfactant in the Reaction of Aryl Diazonium Salts with Single-Walled Carbon Nanotubes

3.2 Introduction

Covalently modified carbon nanotubes have been utilized for a variety of applications[121], ranging from drug-delivery vehicles[122-124], to molecular sensors[125, 126] and are promising materials for the development of both optical[127] and mechanical[128] switches. However, for such applications as electronic sensors and actuators, the introduction of covalent defect sites to the highly conjugated nanotube sidewall significantly alters the electronic properties of the nanotube, which in the case of single-walled carbon nanotubes (SWCNTs), can substantially hinder tube conductance [129, 130]. Additionally, in the case of semiconducting SWCNTs, such defect sites can quench nanotube fluorescence along a length of approximately 140-240 nm[94, 131], thereby inhibiting the use of covalently modified nanotubes for fluorescence sensing applications. Thus, there is an interest in developing a means of controlling the degree of covalent functionalization, such that the majority of the properties of pristine nanotubes are preserved.

To date, efforts toward controlling the extent of nanotube reaction have primarily focused on reaction stoichiometry[17], reaction time[18], and harshness of oxidative treatment[19-21]. However, nanotube solutions may possess as many as 30 distinct species of semiconducting nanotubes[22], alone, with each nanotube potentially exhibiting a significantly different affinity toward a reagent molecule. In fact, the reactivity of a particular species is often dependent upon the specific properties of the nanotube[132], including electronic structure[23-25], diameter [21], and bond curvature radius[26]. Therefore, it remains difficult to obtain similar degrees of functionalization across all species. Here, we examine the promise of utilizing dispersing agents to help control the extent of functionalization in the reactions of carbon nanotubes with diazonium salts.

Diazonium salts are useful candidates for the covalent modification of carbon nanotubes because they can be synthesized with a variety of different functional groups[133], which can

then be utilized for additional chemistry[134, 135]. However, it is well-known that aryl diazonium salts undergo a large number of reactions in solution[136]. Even in the limited case of aryl diazonium reactions with carbon nanotubes, a variety of mechanisms have been proposed[24, 30, 137, 138], sometimes displaying significantly different trends in reaction selectivity. These trends range from enhanced reactivity of metallic, and large diameter species[24, 32], to preferential reaction of small bandgap tubes[137]. In the case of metallic-selective reaction, it has been determined that the rate-limiting step of the reaction involves electron-transfer from the nanotube to the diazo moiety, and that selectivity is imparted during the initial, adsorption step of the reaction[24, 32]. This has allowed for the use of chemical derivatization as a means of separating carbon nanotubes by electronic type[96, 105] and for increasing the on-off ratio of SWCNT network transistors[139-141]. In the small band-gap selective case, the trend in reactivity has been attributed to the formation of an electron-rich, diazoanhydride intermediate under basic conditions. However, despite these mechanistic hypotheses, little work has been expended toward elucidating the role of the surfactant in these reactions.

Because surfactants and polymers stabilize nanoparticles by a variety of mechanisms, from coulombic forces, to steric exclusion, and thermal fluctuations[142], it should be expected that these adsorbed layers will also influence the ability of a reagent molecule to access the nanoparticle surface. It is useful to explore this effect for two reasons: (1) the reactions of SWCNT-surfactant complexes can provide insight into the structure of the surfactant wrapping, and (2) the surfactant wrapping, if understood, can help direct, and control, the chemical functionalization of SWCNTs, as we show. Indeed, promise toward utilizing surfactants to direct SWCNT modification has been demonstrated in the regioselective, end-modification of oxidized carbon nanotubes[27, 28, 143]. Here, we investigate the influence of surfactant on the diazonium reactions of carbon nanotubes. We particularly focus on the fluorescence quenching response of SWCNT solutions, since this provides the most sensitive indicator of covalent functionalization[137]. In doing so, we design the reaction conditions such that there is only a partial quenching of the nanotube fluorescence, since these conditions are likely to correspond to the conditions under which the nanotubes possess both pristine segments, and covalent functional handles. Ultimately, it is found that the surfactant can affect the reactions of carbon

nanotubes in a variety of ways, including electrostatics, steric exclusion, and direct chemical modification of the reacting species.

3.3 Methods

Sample Preparation

HiPCO nanotubes (Unidym, Inc.) were suspended using methods similar to those previously published[144], which have been shown to produce individually dispersed carbon nanotubes, thereby minimizing aggregation effects. Briefly, for each sample, nanotubes were dispersed at 1mg SWCNT/mL solution (~30mL total volume) via 30 minutes of homogenization using a T-10 Ultra-Turrax (IKA Works, Inc.) dispersion element at approximately 11,400 min^{-1}. Linear chain surfactants were utilized at 1wt%, while bile salts were used at a concentration of 2wt%. The homogenized dispersions were sonicated at 10W, in an ice bath, for 1 hour using a 6mm probe tip (Cole-Parmer). Samples were then centrifuged at 30,000 rpm (153,720 rcf) and 22°C for 4 hours, and the supernatant collected. For CTAB, efforts were made to minimize the precipitation of surfactant during ultracentrifugation by operating above the Krafft temperature (~25°C). The aryl diazonium salt, 4-Propargyloxybenzenediazonium tetrafluoroborate, was synthesized according to previous protocols[135, 145, 146] and stored at -20°C until use. Fresh stock solutions of diazonium were prepared immediately prior to all experiments.

SDS and CTAB Transient Reactions

SWCNT solutions (pH = 5) were preheated to 45°C and the PL was allowed to stabilize for 1 hour prior to initiating the reaction. Reactions were initiated by a single injection of diazonium solution to the well-stirred vessel, such that the final molar ratios of diazonium to carbon were 1.10×10^{-4} and 3.25×10^{-2} for SDS and CTAB, respectively. Photoluminescence spectra were obtained using a fiber optically coupled MKII Probe Head (Kaiser Optical Systems), fitted with an immersion optic, which served as both the excitation and collection device. The excitation element of the probe head was fiber optically coupled to a 785nm Kaiser Invictus laser (~54 mW at sample). The collection port was coupled to a liquid nitrogen-cooled, nIR InGaAs detector (Princeton Instruments) through a PI Acton SP2150 spectrometer, with which transient photoluminescence spectra were acquired.

SDS Selective Reaction

SDS selective reactions were carried out by pre-heating samples (pH = 5) to 45°C, allowing them to stabilize at that temperature, and initiating the reaction by a single addition of diazonium solution to the well-stirred vessel. Solutions were reacted 24 hours, and were carried out at 3 different molar ratios of diazonium to carbon: $6.50x10^{-5}$, $1.30x10^{-4}$, and $1.95x10^{-4}$.

Bile-Salt SWCNT Reactions

Solutions were pre-heated to 45°C and allowed to stabilize for 1 hour prior to addition of diazonium reagent. For all samples, the SWCNT solution was diluted to a total carbon concentration of 15 mg/L. Reactions were initiated by a single addition of diazonium solution, and were allowed to proceed for 24 hours at 45°C under constant stirring. Photoluminescence (785nm excitation) and 2D excitation-emission data were acquired using a home-built near-infrared fluorescence microscope which has been described previously[147]. Raman spectroscopy was performed on dispersed nanotube samples using a LabRAM HR spectrometer (Horiba) with a 633nm excitation source. A Shimadzu UV-310PC spectrometer was utilized for UV-vis-nIR absorbance measurements.

3.4 Results

In order to study the influence of surfactants on the diazonium derivatization of carbon nanotubes, six surfactant molecules were utilized (fig 3.1). For examining the effects of surfactant charge, two linear-chain surfactants were used, sodium dodecyl sulfate (SDS), and cetyltrimethylammonium bromide (CTAB). These surfactants are expected to form loosely packed, beaded structures on the nanotube surface[30, 148-150], which results from a tendency of the flexible, aliphatic chains to orient themselves into hydrophobic regions. Further, because the molecules are not rigid, they present little steric hindrance to diazonium derivatization, thereby allowing for direct observation of coulombic effects. For examining the effects of structural packing and surfactant rigidity, four bile salts, sodium cholate (SC), sodium deoxycholate (SDC), sodium taurocholate (STC), and sodium taurodeoxycholate (STDC) were used. In contrast to the linear-chain surfactants, these bile salts possess stiff, steroidal backbones that impart them with their characteristic hydrophobic and hydrophilic "faces"[151]. Computational simulations have shown that this bifacial nature of sodium cholate causes the surfactant to form a tightly packed monolayer on the SWCNT surface[30, 152]. Therefore, these six surfactants allow the examination of how rigidity and charge influence the reactions of

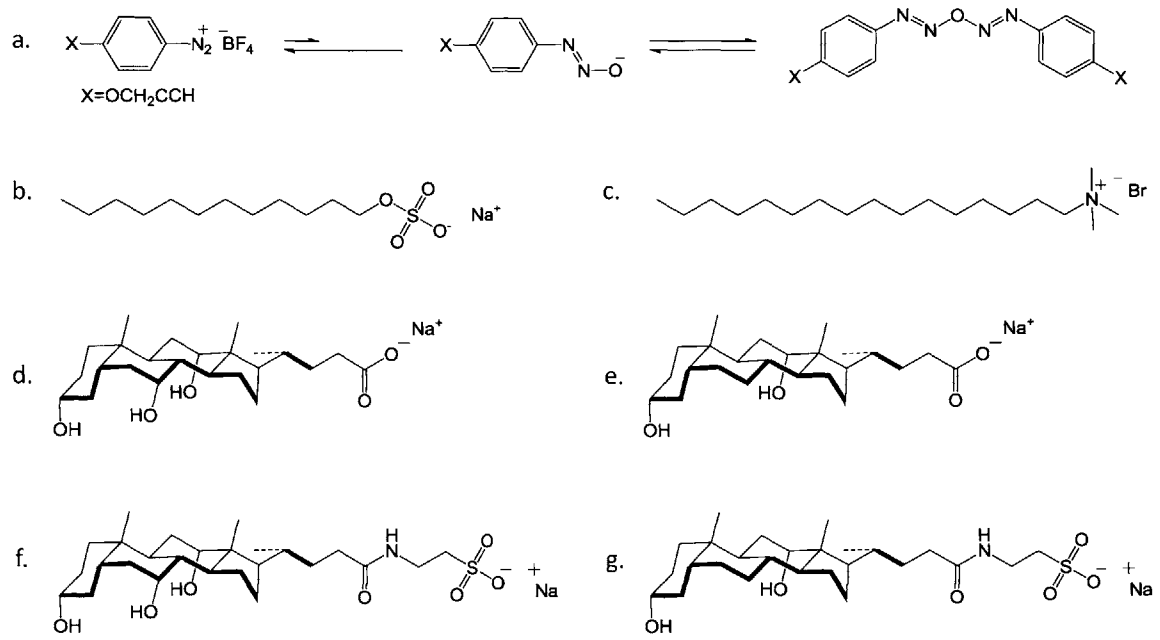

Figure 3.1 Structures of the diazonium ion and six surfactants utilized in this study. Diazonium salt: (a) running reactions under slightly acidic conditions favors the cationic diazonium ion over the base-mediated conversion to diazotates and diazoanhydrides. Surfactants: (b) sodium dodecyl sulfate, (c) cetyltrimethylammonium bromide, (d) sodium cholate, (e) sodium deoxycholate, (f) sodium taurocholate, and (g) sodium taurodeoxycholate. The bile salts, (d)-(g), have rigid steroidal backbones, which impart them with hydrophobic and hydrophilic "faces". The rigidity of these bile salts causes them to form close-packed structures on the nanotube surface. The linear chain surfactants, (b) sodium dodecylsulfate and (c) cetyltrimethylammonium bromide possess less rigid, lipidic chains, which tend to coat the nanotube in a more disordered manner.

diazonium salts with carbon nanotubes. It should be noted that for all reactions, the use of slightly acidic conditions aids in preserving the cationic, aryldiazonium moiety by suppressing the base-mediated conversion to the corresponding diazotate or diazoanhydride (fig. 3.1(a))[136].

Linear Chain Surfactants

Because the diazonium ion is cationic, it is of interest to see how the charge of the surfactant-SWCNT complex affects the ability of the diazonium molecule to access the SWCNT surface. Due to the relatively fast reaction kinetics of SDS-SWCNTs, and the desire to directly observe how the charge of the SWCNT-surfactant complex actively attracts or repels diazonium ions, we continuously probed the fluorescence quenching response of SDS- and CTAB-suspended SWCNTs upon exposure to aryl diazonium salt. Under dark reaction conditions at pH = 5 and T = 45°C, SDS-suspended carbon nanotubes have been shown to undergo an electronically selective reaction which depends upon the nanotube density of states[24, 32]. Such reactions are shown in figure fig. 3.2(a-c), for different molar ratios of diazonium to carbon.

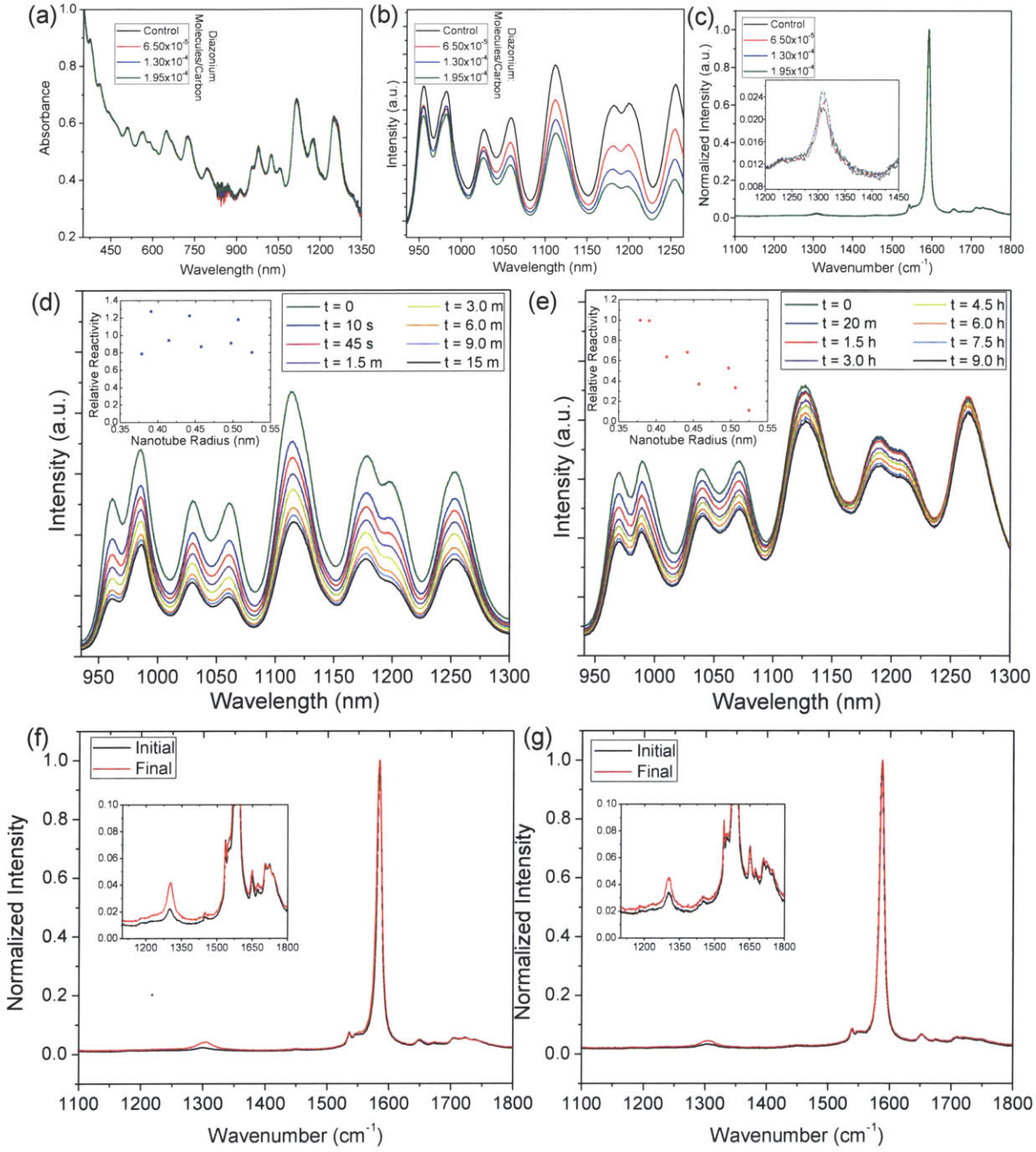

Figure 3.2 Reaction data for SDS and CTAB-SWCNTS under various conditions. (a)-(c) Selective reaction data for SDS-SWCNTs under dark conditions. (a) Absorbance data shows little change under addition of small quantities of reagent. (b) Fluorescence spectra show an enhanced reactivity of small band-gap semiconductors for all aliquot sizes. (c) Raman data (normalized by the G-peak intensity) depicting slight increases in the D-to-G ratio with additional reagent, which is characteristic of covalent derivatization. (d)-(e) In situ snapshots of the transient fluorescence quenching response of carbon nanotubes suspended in (d) SDS and (e) CTAB, upon addition of diazonium salt. Here the samples are continuously illuminated at an excitation wavelength of 785 nm. (d) In the case of SDS, a similar fluorescence response is observed across all species. (e) CTAB exhibits a preferential reaction of small diameter species. Insets depict the relative reactivities of 8 nanotube species as a function of tube radius. (f)-(g) G-peak-normalized pre- and post-reaction Raman spectra (633nm excitation) for (f) SDS and (g) CTAB-SWCNTs, which demonstrate an enhanced D/G ratio (D peaks shown in insets).

Here, the extent of reaction is small enough that there is a negligible effect on the absorbance spectra of the solutions. In contrast, the nanotube fluorescence, which is more sensitive to covalent functionalization than absorbance[137], depicts a preferential decrease in emission features associated with small band gap semiconducting nanotubes, whose E_{11} transition energies appear furthest into the near-infrared (fig. 3.2(b)). It is worth noting that SDS-SWCNTs are much more reactive than SWCNTs dispersed in other surfactants, such that a similar quantity diazonium, when applied to the other SWCNT-surfactant systems studied here, results in little to no degree of functionalization (fig. 3.3). This is likely attributable to both the charge and loose structural packing of the SDS molecules.

When laser-illumination is used to analyze the transient quenching response, a substantially different reaction trend is observed for both SDS and CTAB-SWCNT solutions. For transient experiments, SWCNT suspensions (pH = 5) were preheated to 45°C and reactions were initiated by a single injection of diazonium solution. During reaction, the transient fluorescence behavior was monitored *in situ* by utilizing an immersion optic-fitted Kaiser Raman MKII probe head, which was coupled to a nIR spectrometer. In order to collect photoluminescence spectra in real-time, the reacting samples were continuously excited using 785nm laser illumination (~54 mW at sample) during the experiment. The fluorescence spectra of the SDS- and CTAB-SWCNT solutions, at various time points after addition of diazonium ions, are depicted in fig. 3.2(d) and fig. 3.2(e), respectively. For anionic SDS, the fluorescence quenching response appears to be relatively independent of the nanotube species, with all SWCNTs exhibiting similar degrees of quenching. Further, the quenching response occurs very quickly, leveling off after approximately 25 minutes. On the other hand, CTAB-SWCNTs, besides displaying a much slower quenching rate than that of SDS-suspended nanotubes, exhibit an enhanced reactivity of large band-gap (small diameter) species. Spectral deconvolution allows for more rigorous analysis of 8 nanotube species whose fluorescence is predominantly observed at 785 nm laser excitation. The relative reactivities of these 8 species are depicted as a function of tube radius in the insets of fig 3.2(d)-3.2(e). In the case of both surfactant systems, covalent derivatization was confirmed by Raman spectroscopy, which displayed an increase in the D/G ratio(fig. 3.2(f)-3.2(g)).

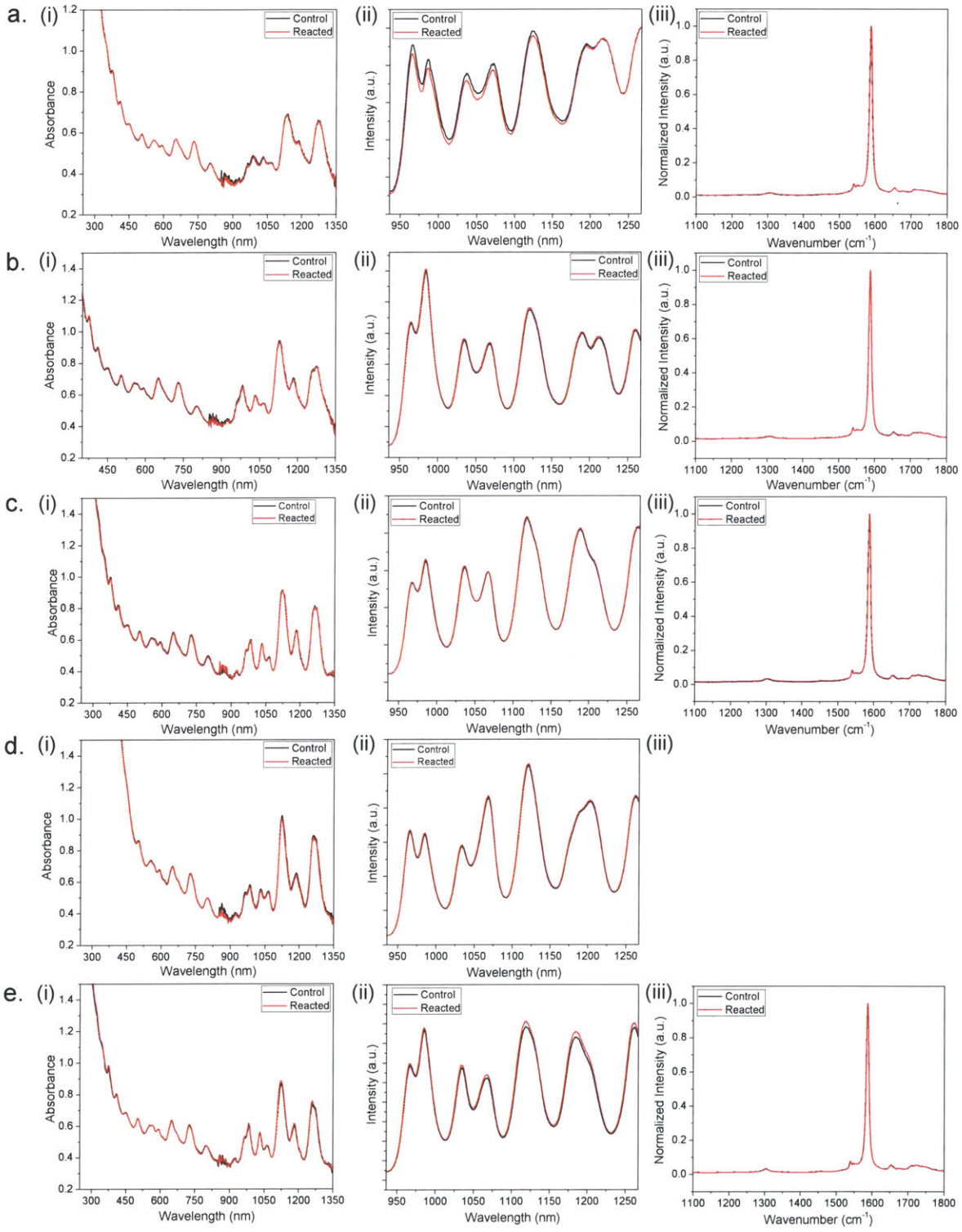

Figure 3.3 (i) Absorbance (ii) fluorescence, and (iii) Raman data for reactions performed under conditions similar to SDS-selective reactions (1.10 x 10^{-4} moles diaz./mole carbon, pH 5.5, T = 45°C, 24 hour reaction time). Rows correspond to the surfactants (a) CTAB, (b) SC, (c) SDC, (d) STC, and (e) STDC. Because of the loose packing of SDS on the surface of the nanotube, reaction occurs at diazonium concentrations that are several orders of magnitude lower than those used for other surfactants. The absorbance, fluorescence, and Raman spectra (above) show that, under similar conditions, the other surfactant-SWCNT solutions undergo little to no reaction.

Bile Salt Derivatives

The effects of surfactant rigidity and structure were analyzed with a focus on bile salt derivatives. Here, the rigidity of the surfactant layer resulted in much slower reaction kinetics, which were dominated by the effects of structural packing, even under laser illumination. Therefore, for analyzing the reactions of bile salt-suspended SWCNTs, reactions were performed over a 24 hour time period in the absence of illumination. The absorbance spectra of nanotube suspensions at varying conversions are depicted in fig. 3.4. As can be seen in fig. 3.4(a), sodium cholate-SWCNTs appear to undergo electron-transfer-selective reaction, with peaks attributable to the metallic E_{11} transitions disappearing first, followed by small band-gap and then larger band-gap semiconductors. In contrast to sodium cholate, the structural homolog, sodium taurocholate (fig. 3.4(c)), exhibits a minimal degree of reactivity with only a small decrease in select absorbance peaks. The deoxycholate bile salts, sodium deoxycholate (fig. 3.4(b)) and sodium taurodeoxycholate (fig. 3.4(d)) demonstrate similar reactivity trends. However, a strong absorption peak at 309 nm, in the case of STDC-SWCNT, indicates that a significant amount of residual diazonium ion remains in the STDC-SWCNT solution, which does not appear in the case of SDC. A similar comparison between SC and STC was not possible due to saturation of the STC absorbance spectrum in the ultraviolet region. After the allotted reaction time, Raman spectra were taken in order to evaluate the D/G ratio of each sample (fig 3.4(e)-3.4(f)). Consistent with absorbance results, sodium cholate-suspended nanotubes exhibit the largest D/G ratios (fig 3.4(e)). The two deoxycholic species, SDC (fig. 3.4(f)) and STDC (fig (3.4(g)), appear to attain comparable D/G ratios for similar quantities of added diazonium. Raman analysis of the sodium taurocholate derivative was not possible due to a large background signal. Judging from these data, it appears that all solutions have similar reactivity trends, with larger band-gap species reacting preferentially to smaller band-gap tubes, albeit to different extents. However, upon analyzing fluorescence data, a significantly different trend is observed.

The corresponding fluorescence spectra for the bile salt suspensions are shown in fig. 3.5. Here, the data are presented as both the raw spectra and deconvoluted, fractional quenching results for individual species. In agreement with the absorbance data of fig. 3.4, SC-SWCNTs undergo a reaction that is predominantly determined by the electronic structure of the nanotube. This is apparent from the fractional quenching results of the individual species, which have

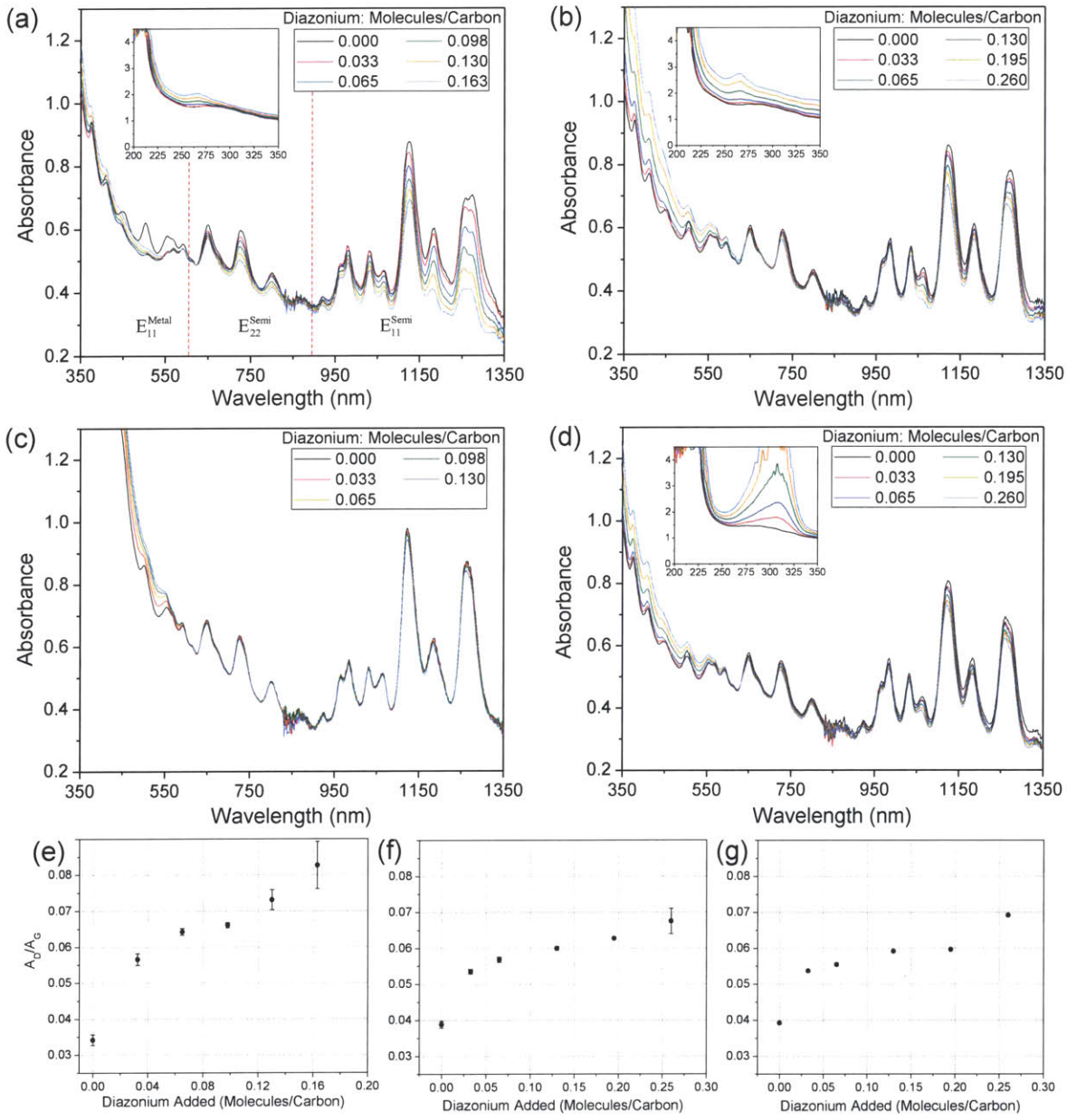

Figure 3.4 Absorbance spectra for four bile salts, (a) sodium cholate and (b) sodium deoxycholate, (c) sodium taurocholate, and (d) sodium taurodeoxycholate, and Raman D/G ratios for (e) sodium cholate, (f) sodium deoxycholate, and (g) sodium taurodeoxycholate. Spectra have been normalized to match abs(632nm) of the control. (a) Sodium cholate provides the clearest demonstration of selective reaction, with metallic and large diameter (small bandgap) nanotubes reacting preferentially. The other three species also appear to demonstrate an enhanced reactivity of small band-gap semiconductors, albeit to different extents. The increase in baseline, toward the ultraviolet region, can be attributed to reaction byproducts. Raman reaction trends for sodium deoxycholate (f) and sodium taurodeoxycholate (g) appear similar, which is consistent with their absorbance spectra, which also show similar results. (e) The D/G ratios for sodium cholate attain higher values than those observed for the other bile salts, which is consistent with a greater decrease in the absorbance associated with Van Hove singularities.

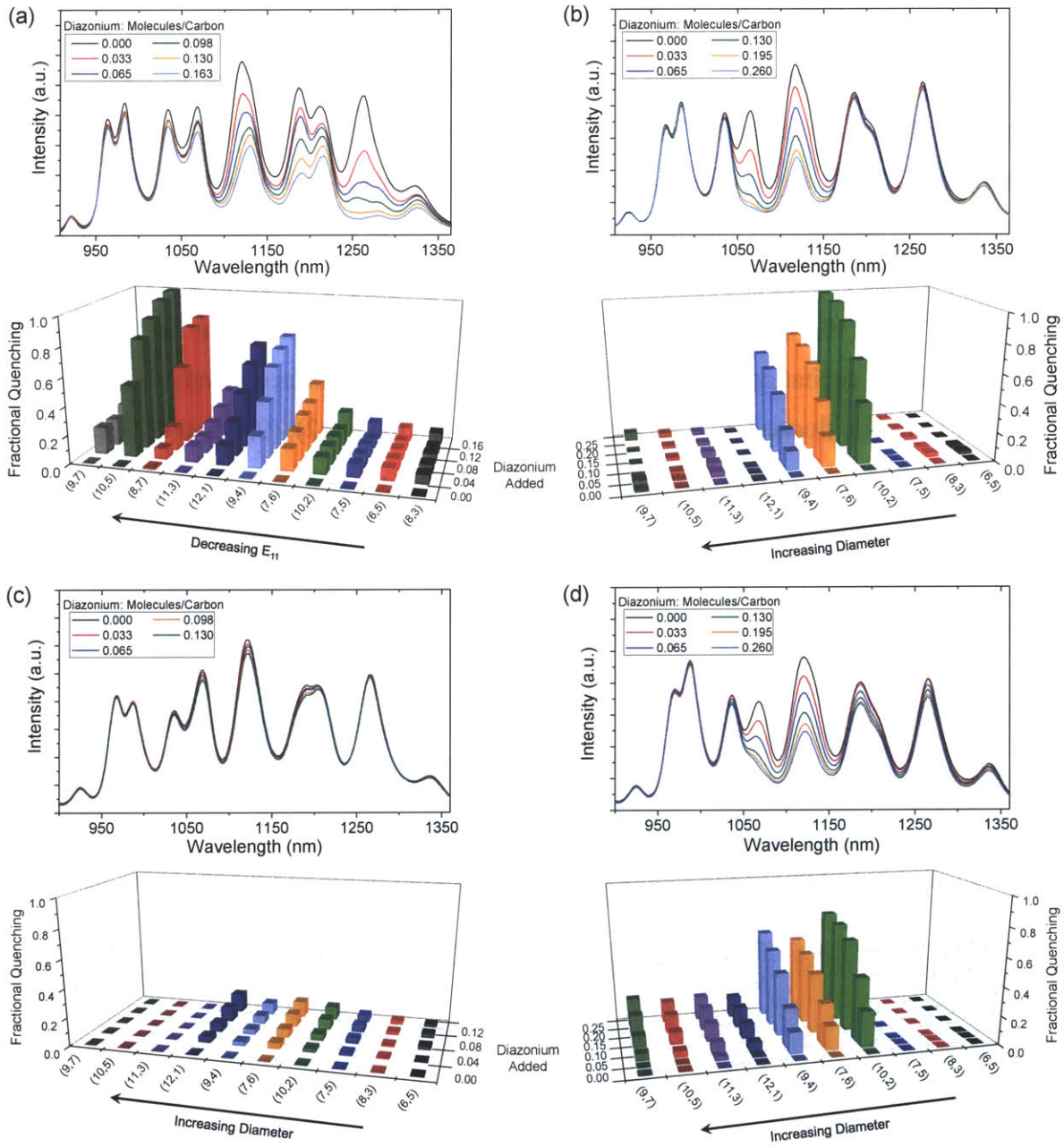

Figure 3.5 Fluorescence spectra and deconvoluted fractional quenching results for the four bile salts used in this study: (a) sodium cholate, (b) sodium deoxycholate, (c) sodium taurocholate, and (d) sodium taurodeoxycholate, at an excitation wavelength of 785nm. (a) As observed in the absorbance spectra, sodium cholate demonstrates predominantly electron-transfer selective reaction, with large diameter (small bandgap) nanotubes reacting preferentially. For sodium cholate, the fractional quenching results are generally plotted from large to small E_{11} gap. For species whose E_{11} emissions overlap to the extent that a single peak is observed (i.e. (9,4)/(7,6) and (10,5)/(8,7)), the species with the larger E_{22} gap has been plotted first. In contract to sodium cholate, the other three bile salts display preferential reactivity among a small population of nanotubes (see text).

generally been arranged according to the magnitude of their E_{11} band-gap. In going from right to left, those species whose E_{11} gaps overlap, such that their combined emissions appear as a single peak in the emission spectra (i.e. (9,4)/(7,6) and (10,5)/(8,7)), the species with the larger E_{22} gap has been plotted first. Here, except in the case of the (11,3) and (9,7) species, a general increase in reactivity is observed as the E_{11} band-gap decreases. However, as is especially evident in the case of SDC, the other SWCNT-surfactant complexes appear to undergo reactions among only a small subset of nanotube species. For SDC-SWCNT, the reacting population is comprised of: (10,2), (9,4), (7,6), (10,3), (11,1), and to a lesser extent, (8,4). This result is more clearly demonstrated in the excitation-emission spectra of reacted and unreacted samples (fig 3.6). Of these affected species, fluorescence features associated with the (10,2), (9,4) and (7,6) nanotubes are predominantly observed at an excitation wavelength of 785 nm, and their fractional

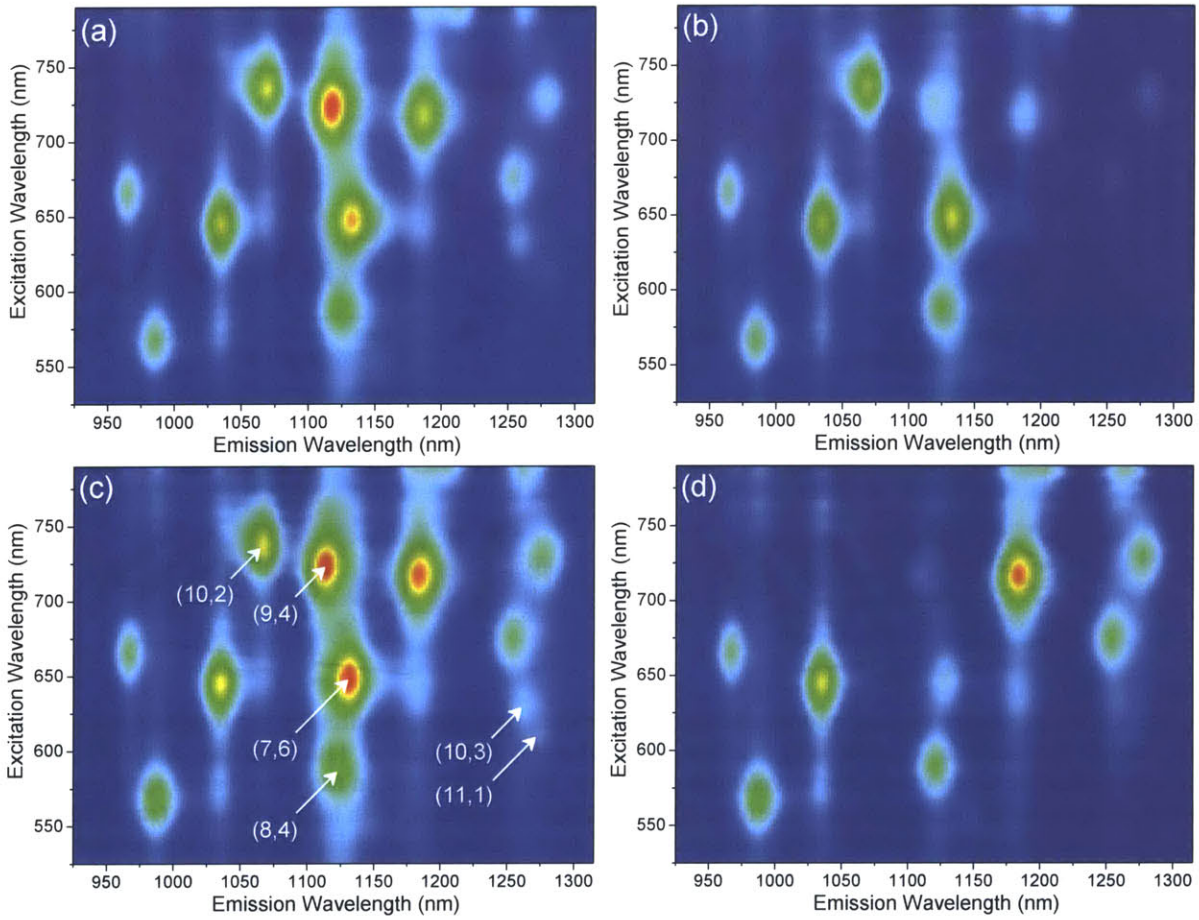

Figure 3.6 Excitation-emission spectra of unreacted (left), and reacted (right), SC-SWCNT (a)-(b) and SDC-SWCNT (c)-(d). In agreement with electron-transfer limitation, the SC-SWCNT reaction progresses from the top right to the bottom left of the plotted spectrum. SDC-wrapped SWCNTs, however, undergo reaction among predominantly a small diameter range of species, including (10,2), (9,4), (7,6), (10,3), (11,1), and to a lesser extent, (8,4).

quenching results are depicted in fig 3.5(b). Here, it is evident that these three species react to the near exclusion of the other semiconducting nanotubes which are observable at 785nm excitation. Similar trends are seen for STDC (fig.3.5(d)) and STC (fig 3.5(c)), though to different extents of reaction. In addition, a similar reactivity trend is observed under laser illumination, indicating that the surfactant packing, rather than electron transfer, is dominant in determining the SWCNT reactivity (Fig. 3.7). As is consistent with the absorbance data in fig. 3.4(c), sodium taurodeoxycholate-suspended nanotubes exhibit only a small degree of fluorescence quenching when compared to the other analyzed bile salts. It is worth noting that at even the lowest diazonium concentrations used for the bile salt species, SDS-suspended SWCNTs undergo significant extent of reaction, providing further evidence of the loose, pliable packing of SDS on the nanotube surface (fig. 3.8).

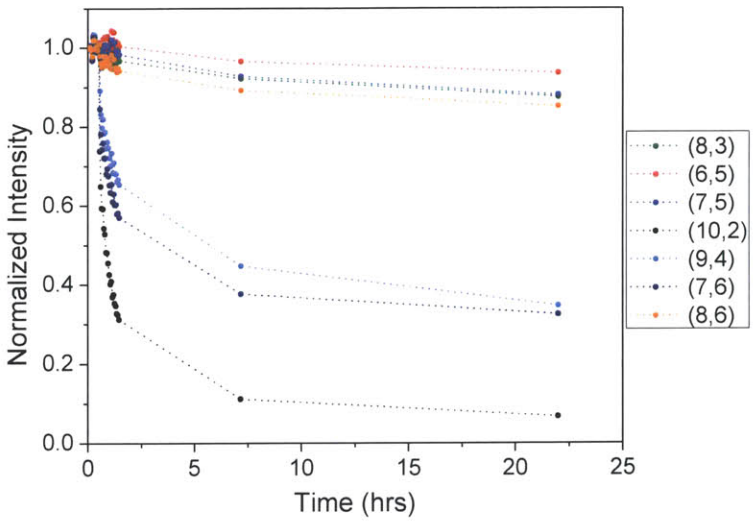

Figure 3.7 Transient fluorescence response of 2% SDC-suspended SWCNTs under constant laser illumination. Due to surfactant exclusion effects, the reaction of the bile salt suspended SWCNT samples takes much longer than the reactions of SDS, and the reactivity remains dominated by packing effects, as evidenced by the enhanced quenching response of (9,4), (7,6), and (10,2).

3.5 Discussion

Linear Chain Surfactants – Diffusion-Limited Kinetics

Under dark conditions, SDS-SWCNTs show typical, electron-transfer-limited reaction (fig 3.2(a)-(b), in which metallic and small band-gap species display a higher reactivity than large band-gap semiconductors[24, 96]. This is consistent with reported studies in which other surfactants were utilized, including Pluronic F127[138] and sodium cholate[105], and is in agreement with the predictions of electron-transfer theories [32, 90]. Generally, this selectivity results from an enhanced ability of these nanotube species to transfer an electron to the electrophilic, diazo moiety, thereby facilitating decomposition of the aryl diazonium molecule. However, under constant laser illumination, electron-transfer selectivity is not observed for

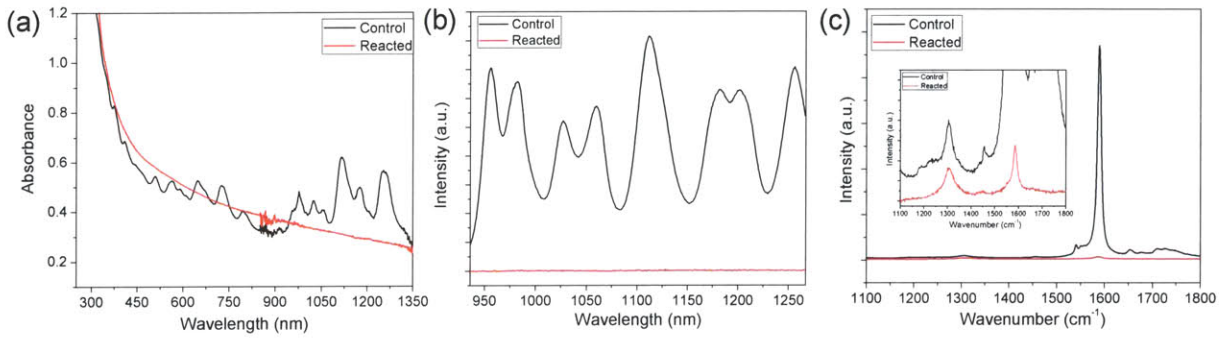

Figure 3.8 Experimental results for an SDS-SWCNT reaction performed under conditions similar to the lowest diazonium concentration bile salt reactions (0.033 moles diaz./mole carbon, pH 5.5, T = 45°C, 24 hour reaction time). Because of the loose packing of SDS on the surface of the nanotube, as well as its negative charge, (a) absorbance, (b) fluorescence, and (c) Raman measurements indicate that the nanotubes are highly functionalized under these conditions.

either SDS or CTAB-SWCNTs. We particularly noticed that, in the case of CTAB-SWCNTs, the reaction rate was very small due to coulombic repulsion between the diazonium ion and the adsorbed, surfactant layer, giving the appearance of diffusion-limitation.

Here, a diffusion-limited model is proposed for the reaction of surfactant-coated SWCNTs with aryl diazonium salts. Each nanotube is treated as residing within a cylindrical cell of solution[153, 154], which contains only a single SWCNT-surfactant complex and its corresponding counterions. This model hinges on the assumption that the SWCNT particles are dispersed at large enough distances that, on average, their interactions are negligible. Thus, there is a radius between SWCNTs at which the electrostatic potential goes to zero. Because nanotube solutions are typically dilute (~20nM in this study), this approximation should be valid. A schematic of the cell model is depicted in fig 3.9. For the purpose of this study, it was assumed that the charged heads of the surfactant layer reside on a cylindrical plane located at a distance, δ, from the nanotube surface. This distance was chosen to be 0.4 nm based on

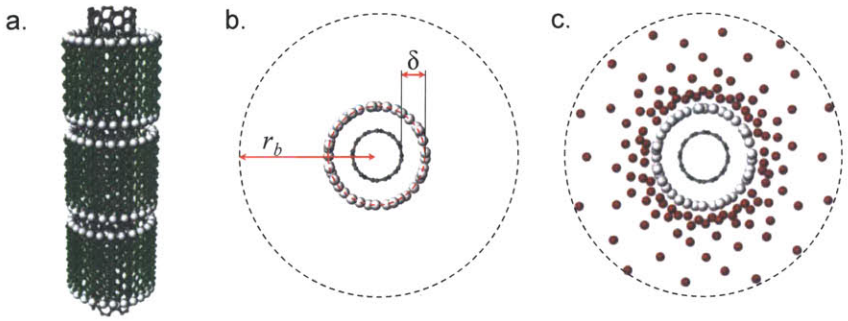

Figure 3.9 Illustration of the cell model, which was utilized to study the relative reactivities of SWCNTs in the diffusion limit. (a) Schematic of a surfactant encapsulated SWCNT. (b) Looking down the SWCNT axis, the charged head groups of the surfactant are assumed to reside on a cylindrical plane located a distance, δ, from the nanotube surface. The distance, r_b, is the radius at which the potential and the derivative of the potential go to zero. (c) Schematic of how the cell may appear in the presence of counterions.

molecular dynamics simulations of SDS-encapsulated SWCNTs[149]. The distance, r_b, represents the radial distance from the SWCNT axis to the boundary of the cell, at which both the potential and the derivative of the potential go to zero[155].

In diffusion limited reactions, as in the theory of slow coagulation[156], the rate of reaction is determined by the flux of diazonium molecules to the nanotube surface. In the presence of a potential, ψ, the flux of an ionic species is described by the Nernst-Planck equation:

$$\vec{J} = -D_A\left[\nabla C_A + \frac{z_A C_A F}{RT}\nabla\psi\right] \tag{3.1}$$

Where F is Faraday's constant, and D_A, z_A, and C_A are the diffusion coefficient, charge, and concentration of the diazonium ions, respectively. If the reaction is at steady-state, and edge effects are neglected, then the number of molecules passing through a cylindrical shell of area, $A = 2\pi rL$, where L is the SWCNT length, is equal to the diazonium-SWCNT collision rate, which is given by:

$$R_c = 2\pi rLD_A\left[\frac{dC_A}{dr} + C_A\frac{d\left(z_A F\psi / RT\right)}{dr}\right] = \text{constant} \tag{3.2}$$

Using the condition that $\lim_{r\to r_b}\psi = 0$, and assuming that the concentration of diazonium is effectively zero at the nanotube surface, it is possible to derive an expression for the rate of collision of aryl diazonium ions with a carbon nanotube in solution:

$$R_c^{(n,m)} = \frac{C_\infty 2\pi LD_A}{\int_{r_{(n,m)}+\delta}^{\infty}\frac{1}{r}\exp\left(F\psi / RT\right)dr} \tag{3.3}$$

where C_∞ is the bulk concentration of the aryl diazonium molecule, and z_A has been defined as +1. While this equation has been derived under the assumption of a constant collision rate, the ratio of collision rates, $R_c^{(n,m)} / R_c^{ref}$, fundamentally represents the relative attraction of diazonium ions to each SWCNT-surfactant complex, and is therefore more generally applicable. In order to utilize this expression, it is necessary to first evaluate the potential distribution, ψ, around the nanotube.

Within the cell of our model, the potential profile can be obtained by solving a modified Poisson-Boltzmann (MPB) equation, which incorporates excluded volume effects associated with counterion condensation[154, 157]. In a micellar system in which only surfactant counterions are present, the Poisson-Boltzmann equation can be represented as:

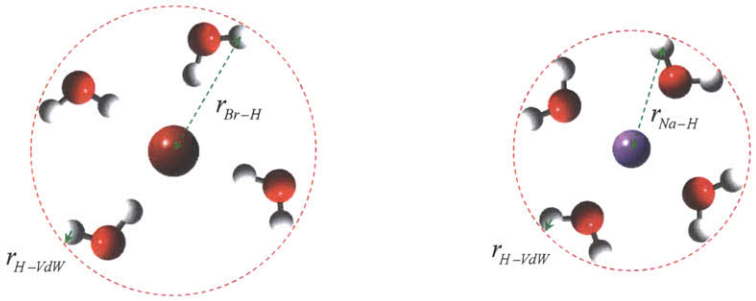

Figure 3.10 Schematic depiction of the effective volume of the ion, which assumes that the ion is surrounded by a single hydration shell. The schematic on the left is that for the CTAB bromide counterion, while the schematic on the right depicts the case of the SDS sodium counterion.

$$\nabla^2\psi = -\frac{z_c F c_c(r)}{\varepsilon} \tag{3.4}$$

Where z_c and $c_c(r)$ are the charge and concentration of the counterion, respectively. In evaluating the potential distribution, the population of diazonium ions is neglected due to its extremely low concentration (< 325 μM) relative to the surfactant (> 27 mM). Accounting for excluded volume effects of ions in solution, the surfactant counterion concentration, as a function of the distance from the tube surface, can be represented by[157]:

$$c(r) = \frac{c_b e^{-z_c F\psi/RT}}{1+\phi_0(e^{-z_c F\psi/RT}-1)} \tag{3.5}$$

Where c_b and $\phi_0 = c_b V_{ion} N_A$ represent the concentration and volume fraction of counter-ions at the cell boundary, respectively. Values for V_{ion} were approximated using: $V_{ion} = 4\pi r_{eff}^3/3$, in which the effective radius of the ion, r_{eff}, assumes a single hydration shell around the counterions, and utilizing hydration shell distances from the literature[158-161]. Therefore, in the case of CTAB, this effective radius was represented by: $r_{eff} = r_{Br-H} + r_{H-VdW}$, where r_{Br-H} is the center-to-center distance between the bromide ion and the outermost hydrogen of the hydration shell, and r_{H-VdW} is the Van der Waals radius of a hydrogen atom, as depicted in Fig. 3.10.

Inserting expression 3.5 into equation 3.4 yields the modified Poisson-Boltzmann equation[157]:

$$\nabla^2\psi = -\frac{z_c F}{\varepsilon}\frac{c_b e^{-z_c F\psi/RT}}{1+\phi_0(e^{-z_c F\psi/RT}-1)} \tag{3.6}$$

The boundary condition at the edge of the cell is specified by requiring that ψ and ψ' go to zero at $r = r_b$, and that at surfactant layer is determined by evaluating Gauss' law at $r = r_{SWNT} + \delta$, and assuming that the gradient of the potential inside of the surfactant layer is zero:

$$\left.\frac{d\psi}{dr}\right|_{r=r_{(n,m)}+\delta} = -\frac{q_e}{\varepsilon} \quad ; \quad \lim_{r\to r_b}\psi, \frac{d\psi}{dr} = 0 \tag{3.7}$$

Here, q_e is the charge density per unit area in the surfactant layer. In order to solve this problem numerically, it is useful to introduce scaling parameters and perform a change of variables. By introducing the scaled variables, ψ and $\tilde{r}$, and defining the Debye length, λ, according to the following relations:

$$\psi = \frac{F\psi}{RT} \quad ; \quad \tilde{r} = \frac{r}{\lambda} \quad ; \quad \lambda = \left(\frac{F^2 c_b}{\varepsilon RT}\right)^{-1/2} \tag{3.8}$$

the non-dimensionalized modified Poisson-Boltzmann equation is obtained:

$$\frac{1}{\tilde{r}}\frac{d}{d\tilde{r}}\left(\tilde{r}\frac{d\psi}{d\tilde{r}}\right) = \frac{e^{\psi}}{1+\phi_0(e^{\psi}-1)} \tag{3.9}$$

By utilizing the following change of variables: $\eta = \ln\tilde{r}$, it is possible to simplify the differential equation such that it can be solved using numerical methods:

$$\frac{d^2\psi}{d\eta^2} = \frac{e^{2\eta}e^{\psi}}{1+\phi_0(e^{\psi}-1)} \tag{3.10}$$

The transformed boundary conditions are:

$$\left.\frac{d\psi}{d\eta}\right|_{\eta=\eta_{surfactant}} = -\frac{q_e F}{\varepsilon RT}e^{\eta_{surfactant}} \quad ; \quad \lim_{r\to r_b}\psi, \frac{d\psi}{d\eta} = 0 \tag{3.11}$$

The non-dimensionalized modified Poisson-Boltzmann equation can be solved using a numerical ODE solver, and initializing the solver at $r = r_b$. At this boundary, ψ and ψ' are specified as zero, and a shooting method (varying the cell radius, r_b) is utilized to satisfy the boundary condition at the surfactant layer.

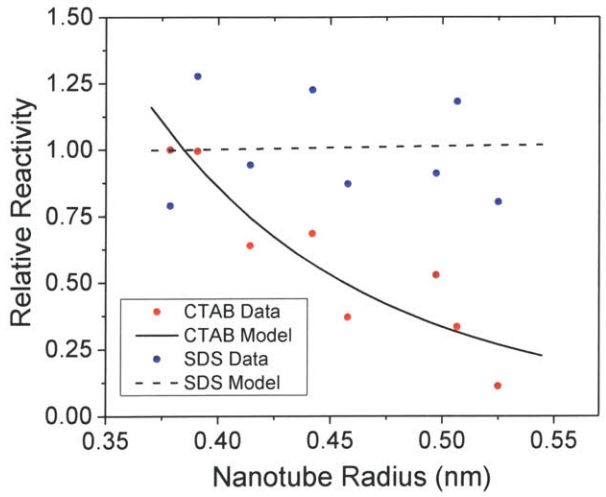

Figure 3.11 Results of applying a diffusion-limited model to the reaction data for SDS and CTAB. For CTAB, the fitting of the model to experimental data resulted in an estimated surface coverage 4.3 molecules/nm^2. For SDS, near-identical trends in reactivity are predicted for a wide range of surface coverages, making it difficult to fit the results to a single value. The black, dotted line corresponds to an SDS surface coverage of 2.8 molecules/nm^2.

For fitting experimental data, all parameters were kept fixed except the surface coverage of surfactant, which was assumed to be invariant across nanotube species. For CTAB-suspended SWCNTs, by fitting the model to the relative reactivities of the 8 nanotube species, the solid black curve in fig 3.11 was obtained, which corresponds to a surface coverage of 4.3 molecules/nm^2. The magnitude of this value is fairly consistent with previously estimated values of 2.2-3.0 molecules/nm^2 for SDS suspended SWCNTs[162]. The decreasing reactivity trend for CTAB-SWCNTs, as a function of tube radius, results from diameter-dependent effects, and can be understood as follows. For very small nanotubes, a large cylindrical curvature exists, which results in a radially diffuse distribution of the potential associated with the surface charge density. As the radius of the tube increases, the overall charge on the tube increases, and distribution of the potential becomes less diffuse. At large enough tube radii, the potential will ultimately approach the flat plate limit, and the relative reactivity will reach a constant value. The potential at the surface is enhanced by excluded volume effects in the vicinity of the surfactant layer, which limit counterion condensation, and cause the potential to reach higher values than it would in the absence of these effects. This allows the exponential term to overcome the $1/r$ dependence in the denominator of equation 3.3. Because the diazonium interaction with CTAB is repulsive, the inherent reaction rate is slow, and small increases in surface potential can result in noticeable changes in fluorescence quenching response.

Interestingly, if the diffusion-limited model is applied to the case of SDS, the observed experimental trend is also predicted. This result can likely be attributed to the continuous excitation of SWCNT electrons during laser illumination, which serves to decrease the energy barrier for electron transfer from SWCNT to the diazonium ion. From a kinetic standpoint, the

behavior can be explained as follows. The reactions of diazonium salts with carbon nanotubes proceed via a two-step mechanism in which the aryl diazonium molecule, A, first adsorbs to the SWCNT-surfactant complex, and subsequently reacts with the nanotube sidewall to form a covalent bond[30]:

$$A + \theta_{(n,m)} \underset{k_D^{(n,m)}}{\overset{k_A^{(n,m)}}{\rightleftarrows}} A_{ads}\theta_{(n,m)} \xrightarrow{k_R^{(n,m)}} A\theta_{(n,m)} \tag{3.12}$$

Here, $k_A^{(n,m)}$ and $k_D^{(n,m)}$ are adsorption and desorption rate constants, respectively, and $k_R^{(n,m)}$ is the rate of covalent reaction. Under electron-transfer limited conditions ($k_R << k_D$), covalent bond formation is the rate determining step, and the first step of the reaction can be assumed to be in equilibrium. This gives rise to the following kinetic expression:

$$\frac{d[A\theta_{(n,m)}]}{dt} = \frac{k_R^{(n,m)} k_A^{(n,m)}}{k_D^{(n,m)}}[A][\theta_{(n,m)}] = k_R^{(n,m)} K_1^{(n,m)}[A][\theta_{(n,m)}] \tag{3.13}$$

where $K_1^{(n,m)}$ is defined as $k_A^{(n,m)} / k_D^{(n,m)}$. For SDS-SWCNTs, if this ratio is presumed to be independent of nanotube species, then the rate constant associated with SWCNT reaction is directly proportional to $k_R^{(n,m)}$, which is associated with electron transfer from SWCNT to the diazonium molecule. Alternatively, as is seen in this study, it is possible to decrease the activation energy associated with electron transfer by supplying excited-state electrons to the reaction. Here, this is done through constant laser excitation at 785 nm. If the rate of electron transfer is significantly enhanced (k_R becomes large), a pseudo-steady-state approximation can be made on the concentration of the adsorbed intermediate. Such a treatment leads to the following kinetic expression:

$$\frac{d[A\theta_{(n,m)}]}{dt} = \frac{k_R k_A}{k_R + k_D}[A][\theta_{(n,m)}] \tag{3.14}$$

In the case that $k_R >> k_D$, the reaction appears to be equivalent to the one shown below, and the reaction is adsorption, or diffusion, limited:

$$A + \theta_{(n,m)} \xrightarrow{k_A^{(n,m)}} A\theta_{(n,m)} \tag{3.15}$$

Because diazo groups are stable to irradiation at red wavelengths[136], the increased reactivity most likely stems from excitation of electrons within the nanotube species, rather than irradiative decomposition of the aryl diazonium moiety. It is interesting to note that in the cases of both

CTAB and SDS, similar species tend to lie above or below the predicted, theoretical curves. This may be due to species-dependent differences in surfactant adsorption, where slight differences in surfactant surface coverage could alter the potential experienced by the diazonium ion. However, if the variation were adsorption-dependent, we would expect to observe a correlation with species diameter, since previous results have indicated that SDS binds more strongly to small diameter species[163]. In the present case, the scattering in the data may more likely be attributable to differences in exciton diffusion length[155], which would cause certain species to experience a greater degree of quenching for a similar extent of functionalization. However, due to the limited data that are currently available, it is difficult to correct for these differences. In sodium deoxycholate, there appears to be a correlation between the apparent exciton range and the diameter of the nanotube, with smaller diameter tubes displaying a shorter exciton mobility[155]. However, it is unlikely that these species-dependent values can be directly applied to the case of linear chain surfactants, since an alternative study has demonstrated that the surfactant, alone, can induce variations in exciton diffusion length[131].

For SDS, the obtained results are in contrast with the previous observation that the reaction proceeds via a two-step mechanism in which the first, adsorption step is selective[30]. Rather, we observe that the attraction of diazonium molecules to the SWCNT surface in the initial, adsorption step, is not necessarily selective, but is largely influenced by the surfactant which encapsulates the nanotube. Therefore, selectivity is necessarily imparted in the second step, where electron transfer and covalent bond formation occurs.

Bile Salts – Effects of Surface Packing and Diazonium-Surfactant Interactions

In the case of bile salt-suspended nanotubes, both the structure of the hydrophilic face and the anionic functional group have a significant influence on the reaction behavior of the SWCNT-surfactant complex. These two characteristics alter the SWCNT reactivity by a combination of reagent exclusion effects, which arise due to the dense packing of the adsorbed layer, and diazonium-surfactant coupling, which alters the form of the reactive diazonium species.

With the exception of SC-SWCNTs, the structural packing of the bile salt surfactants on the nanotube surface results in a diameter-dependent reaction in which only a small subset of

nanotube species are affected. Among three of the four bile salts that were examined (SDC, STDC, and STC), a similar trend in reactivity is observed, which in all cases, results in some degree of quenching of the (10,2), (9,4), and (7,6) fluorescence at 785nm excitation. This trend is most pronounced in the cases of the deoxycholate bile salts, where a degree of quenching occurs which exceeds 50%. Interestingly, these affected species occupy a narrow range of diameters between d = 0.88 and 0.92 nm. The preferential reaction of these nanotubes likely stems from an inability of the surfactant to effectively coat these species, allowing diazonium molecules to access the SWCNT surface. Indeed, it has previously been observed that sodium cholate tends to bind more weakly to the (10,2) nanotube than other chiralities[163, 164]. Here, it is observed that, while the (10,2) chirality exhibits the highest extent of reaction, there is also a significant quenching response among other species with similar diameters. Besides these packing effects, the ionic group of the surfactant also significantly influences the observed reaction trend.

Bile salts that contain carboxylate moieties, such as sodium cholate and sodium deoxycholate, are likely to affect the diazonium-derivatization of carbon nanotubes by altering the reactive diazonium intermediate. This can occur through diazonium-carboxylate coupling, which results in the formation of highly reactive diazoesters[139]. The formation of such species is supported by the observation of an enhanced decomposition of aryl diazonium in the case of SDC when compared to a structurally similar bile salt analog, sodium taurodeoxycholate. Since diazoesters have been shown to exhibit an enhanced selectivity toward metallic nanotubes[139], the formation of these intermediates explains the high selectivity of the aryl diazonium ion for metallic species in the case of SC-SWCNT. However, if the carboxylate moiety facilitates diazoester formation, it would also be expected that nanotubes suspended in sodium deoxycholate would demonstrate a similar, band-gap selective reaction trend, which is not the case. This may be attributed to the formation of secondary micelles around the SWCNT surface, which has been previously proposed for sodium deoxycholate[165]. In such a case, the secondary layer would assist in maintaining the reactive diazoester at distances greater than those required for electron transfer, and only those species which are poorly coated by the surfactant would predominantly react, which is consistent with experimental results.

3.6 Conclusions

The properties of the surfactant shell have a significant influence on the reactions of aryl diazonium ions with single-walled carbon nanotubes. First, the adsorbed layer, being charged, plays an integral role in defining how the diazonium ion approaches and interacts with the SWCNT-surfactant complex. This is most apparent in the diffusion-limited reactions of linear-chain surfactants, where the charge of the adsorbed layer results in substantially different reaction behavior in the cases of CTAB and SDS-suspended nanotubes. Here, it was found that, under laser illumination, all species react equivalently in the case of SDS, while small diameter species react preferentially in the case of CTAB-SWCNT. The observed small-diameter selectivity of aryl diazonium salts toward CTAB-SWCNTs arises due to diameter-dependent electrostatic effects, which result in a decreased coulombic barrier to functionalization for smaller nanotubes. Further, these data demonstrate that, contrary to previous findings, the adsorption of diazonium ions onto the SWCNT surface is not necessarily selective, but is largely influenced by the surfactant which encapsulates the nanotube. Therefore, selectivity must be imparted in the second step, where electron transfer and covalent bond formation presumably occurs.

Surfactants can also influence the reactions of carbon nanotubes by physically excluding the diazonium ion from the SWCNT surface, or by chemically modifying the reactive diazo species. This result was analyzed using four bile salts: sodium cholate, sodium taurocholate, sodium deoxycholate, and sodium taurodeoxycholate. Here, surfactant packing effects result in either very minimal reaction (STC), or reaction among a small population of carbon nanotubes (SDC and STDC), including (10,2), (9,4), (7,6), (10,3), (11,1). Therefore, especially for the deoxycholate species, it appears to be an inefficiency in surfactant packing, on a narrow range of tube diameters (0.88-0.92 nm), which determines reaction selectivity. In addition, the presence of carboxylate ions on the surfactant appears to facilitate diazoester formation and aryl diazonium decomposition in solution. The formation of such species is likely to be responsible for the highly selective reaction of metallic species in the case of SC-SWCNT.

4 Charge-Transfer Structure-Reactivity Relationships for Fullerene/Carbon Nanotube Heterojunctions

4.2 Introduction

Interfacing fullerenes with single-walled carbon nanotubes (SWCNTs) is desirable for a variety of applications, including carbon-based photovoltaics[166] and near-infrared fluorescence sensors[51]. Due to their resistance to photodamage[36] and high carrier mobilities[37], semiconducting SWCNTs hold great potential for utilization in near-infrared harvesting photovoltaic devices. This is evidenced by emerging efforts in developing "all-carbon" photovoltaics[38-41], and it has recently been demonstrated that SWCNT-based photovoltaics outperform polymeric analogues in device lifetime measurements[39]. However, while a large body of work has been directed at fabricating SWCNT-based devices, little work has been expended toward elucidating the kinetics of electron transfer at the SWCNT-fullerene interface. Such a study is beneficial, as a combination of factors, including morphology[39] and active-layer impurities[38], can limit the quantum efficiency of photovoltaic devices. This is evidenced by the fact that the efficiencies of current, SWCNT-based active layer devices falls much lower than the theoretical value of 13% [39]. In addition, $PC_{60}BM$ is not an ideal electron acceptor for SWCNT-based photovoltaics, since the LUMO level lies close to the SWCNT valence band, and therefore, the SWCNT-fullerene heterojunction has been predicted to switch from type II to type I in going from SWCNT diameters of 0.9-1.3nm[39]. The same is true of $PC_{70}BM$, due to similarity in electronic structure. However, C_{84} has a deeper LUMO level than C_{60} and C_{70}[44], as well as a higher photostability[45], making it a potential candidate for SWCNT-based photovoltaics. Because of this, it is of interest to compare across different fullerenes and interfaces in order to optimize photoinduced electron transfer in the absence of complicating factors associated with device fabrication.

In addition to photovoltaic devices, SWCNT-fullerene junctions hold potential for utilization in SWCNT fluorescence-based sensors. SWCNT sensors have demonstrated potential for the detection of a variety of small molecule analytes, including direct detection of nitric oxide[46, 47] and hydrogen peroxide[48], as well as indirect detection of sugars[49] and adenotriphosphate [50]. However, in order to observe molecular adsorption events, it is

necessary that the adsorbing molecule possess redox properties which are capable of modulating the nanotube fluorescence[51]. For the detection of proteins and other biomacromolecules, which do not have redox properties, divalent ions such as Ni^{2+} near the nanotube surface have been utilized as an intermediate species in modulating nanotube fluorescence[52]. Fullerenes are expected to interact with SWCNT by accepting excited-state electrons from the SWCNT conduction band, thereby quenching the SWCNT fluorescence signal. Because this process is distance dependent, it is possible that fullerenes could be employed as a distance-dependent proximity quencher for transducing protein-SWCNT interactions in fluorescence-based SWCNT sensors.

In this study, we examine the structure-reactivity relationships for electron transfer at the interface between SWCNTs and fullerenes by synthesizing a series of fullerene amphiphiles. These amphiphiles give stable suspensions of individual carbon nanotubes, thereby allowing for direct observation of the electronic interactions between these two species. The nature of the interface between the carbon nanotubes and fullerene molecules is probed by a solvatochromism model, and electron transfer characteristic are monitored by relative fluorescence quantum yields. We find that the extent of electronic interaction is dependent upon both the fullerene species that is utilized and the nature of the interface between the SWCNT and the fullerene. We are able to describe experimental observations using a Marcus theory model for electron transfer.

4.3 Methods

Nanotube Suspensions

For mixed chirality suspensions, HiPCO nanotubes (Unidym, Inc.) were initially suspended in 2% sodium cholate (SC). Nanotubes were dispersed at 1mg SWCNT/mL of 2% SC solution (~30mL total volume) via 30 minutes of homogenization using a T-10 Ultra-Turrax (IKA Works, Inc.) dispersion element at approximately 11,400 min^{-1}. These dispersions were then sonicated in an ice bath at 10W for 1 hour using a 6mm probe tip (Cole-Parmer). Samples were subsequently centrifuged at 30,000 rpm (153,720 rcf) and 22°C for 4 hours, and the supernatant collected. 2%SC solutions were exchanged to the desired amphiphile by dialysis (3500 MWCO, Thermo Scientific). This pore size has previously been shown to remove sodium cholate while retaining the PEGylated surfactants[167]. For dialysis, equal volumes of 2% SC suspension (abs(625) ~ 1.08) and amphiphile (2mg/mL) were mixed, resulting in a final

amphiphile concentration of 1mg/mL. This suspension mixture was dialyzed against water for 4 days, with 2 water exchanges per day (V_{H2O} > 200 x V_{SWCNT}), to ensure removal of sodium cholate.

Spectral Characterization

Photoluminescence spectra were acquired using a Zeiss AxioVision inverted microscope which was coupled to a Princton Instruments 1-D array InGaAs detector, operating at -100°C, through a PI-Acton SP150 spectrograph. A 785nm laser was used for photoexcitation. UV-vis-nIR absorbance measurements were carried out on a Shimadzu UV-310PC spectrometer.

4.4 Results

Influence of SWCNT-Fullerene Interface

In order to study the influence of the fullerene-SWCNT interface on electron transfer, five surfactants were synthesized (fig. 4.1). In particular, we wanted to study how the nature of the interface influenced excited-state electron transfer from the nanotube to the fullerene molecule. Therefore, we synthesized molecules that would facilitate interfaces containing aliphatic (lipid-C_{61}-PEG) and polyaromatic (pyrene-C_{61}-PEG) domains, as well as a molecule that would facilitate direct contact between SWCNT and fullerene (methyl-C_{61}-PEG). As control molecules, lipid and pyrene surfactants were synthesized which lacked the intermediate, methanofullerene moiety. All nanotube suspensions were obtained by dialysis, starting from an initial, 2% sodium cholate nanotube suspension. In the case of the methyl-C_{61}-PEG derivative, visible aggregates were formed during the dialysis process, and bundles were observed by AFM (Appendix A). Therefore, the methyl-C_{61}-PEG suspensions were omitted from analysis. All other amphiphiles produced individually dispersed tubes, as evidenced by AFM (Appendix A),

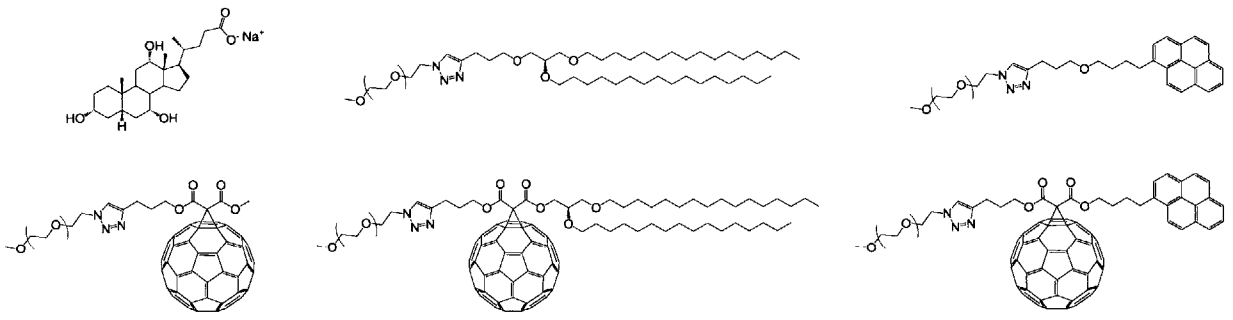

Figure 4.1 Surfactant systems utilized for analyzing interfacial effects on electron transfer.

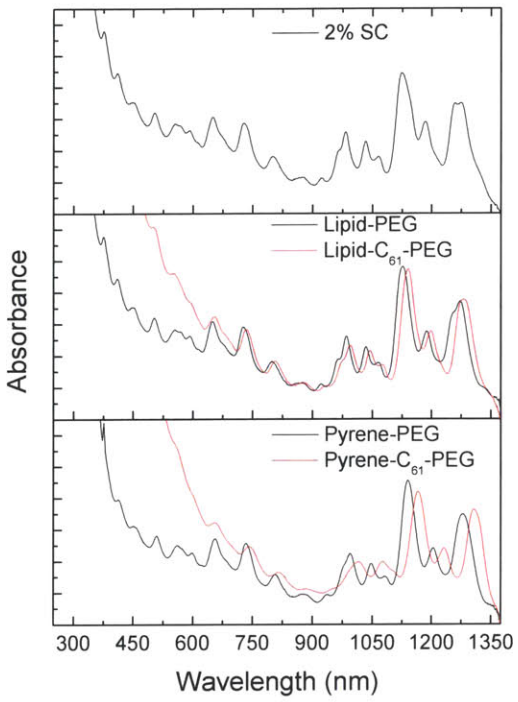

Figure 4.2 UV-vis-nIR absorbance spectra of five of the surfactant systems analyzed in this study (excluding methyl-C_{61}-PEG). The retention of high peak-to-valley ratios is indicative of high quality SWCNT dispersions, in agreement with AFM observations of individually dispersed nanotubes.

and the retention of large peak-to-valley ratios in the photoabsorbance spectra (Fig. 4.2).

We attempted to remove excess, free surfactant by centrifugal filtration. While 100kDa MWCO centrifugal filters were unable to remove excess surfactant molecule from the suspensions, 1000kDa MWCO centrifugal filters proved successful at retaining SWCNTs while having enough porosity to pass the unbound amphiphiles (Appendix A). However, the removal process resulted in visible aggregation in the case of pyrene-PEG, and very slight changes in chirality distribution among the other solutions, which likely resulted from small degrees of aggregation in the removal process. Therefore, all data presented in this manuscript are for SWCNT solutions which did not undergo additional processing after surfactant exchange.

UV-vis-nIR absorbance spectra for the initial sodium cholate suspension, as well as the four amphiphilic surfactant systems (without methyl-C_{61}-PEG) are shown in Figure 4.2. All suspensions have been diluted to similar concentrations, and are plotted on the same scale. From visual inspection of these spectra, it is apparent that high peak-to-valley ratios are maintained during the exchange process, in agreement with the observation of individually dispersed tubes by AFM. In going from the lipid-PEG and pyrene-PEG control molecules to their methanofullerene analogues, a red-shift in peak position is observed across all species. In the case of pyrene-C_{61}-PEG, the red-shift is greater than that observed in the case of the lipid-C_{61}-PEG derivative, indicating that there may be different degrees of interaction between the SWCNT and fullerene molecules in the cases of these two amphiphiles. This will be discussed in more detail later on.

Excitation-emission spectra for the lipid-PEG, lipid-C_{61}-PEG, pyrene-PEG, and pyrene-C_{61}-PEG suspensions are shown in Fig 4.3. As would be expected for a system in which electron

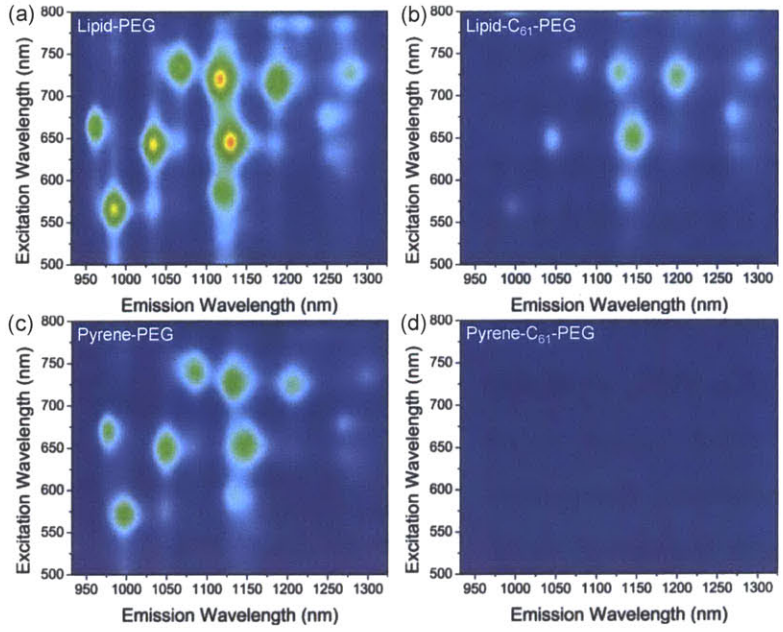

Figure 4.3. Excitation-emission plots for SWCNTs suspended in (a) lipid-PEG, (b) lipid-C61-PEG, (c) pyrene-PEG, and (d) pyrene-C61-PEG. All suspensions are plotted on the same scale.

transfer occurs between SWCNT and C_{61}, these suspensions indicate a general quenching of nanotube fluorescence upon incorporation of C_{61} into the surfactant structure. These plots also allowed for the determination of emission wavelengths for spectral deconvolution of fluorescence emission, as discussed in the next paragraph.

In order to evaluate the extent to which each nanotube species is quenched by C_{61}, we sought to minimize the degree of C_{61} excitation by utilizing 785nm excitation, where absorbance by the C_{61} moiety is minimal. This maximizes the likelihood of observing electron transfer from photoexcited SWCNT to C_{61}, while minimizing ground-state transfer from SWCNT to the photoexcited fullerene. Near-infrared fluorescence spectra, acquired with an excitation wavelength of 785nm, are shown in Figure 4.4(a). Using peak locations from the excitation-emission spectra in Fig. 4.3, these spectra were further deconvoluted into the emission contributions of 10 chiralities of carbon nanotubes, and the relative intensities of these species, normalized to the fluorescence intensity of the initial sodium cholate solution, are presented in figures 4.4(b)-4.4(c). For the pyrene-C_{61}-

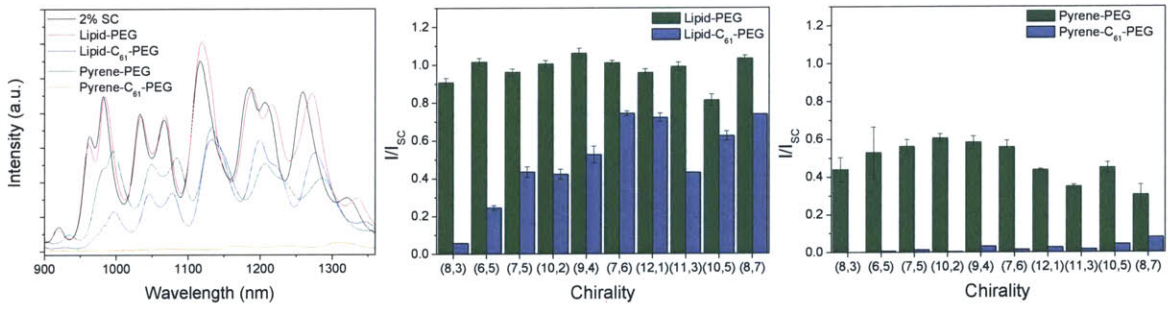

Figure 4.4. Fluorescence results of the surfactant systems analyzed in this study. (a) Raw fluorescence spectra, representing an average of four suspensions for each amphiphile. (b) Fractional quenching results, relative to the intensity of SC-SWCNT, for the lipid-PEG and lipid-C_{61}-PEG systems. (c) Fractional quenching results, relative to SC-SWCNT, for the pyrene-PEG and pyrene-C_{61}-PEG systems.

PEG derivative, it was necessary to estimate peak positions due to the absence of clear fluorescence features in the excitation-emission spectra. In going from left to right the nanotube chiralities are arranged from large to small band-gap. From figure 4.4(b), it is apparent that the lipid-PEG derivative produces solutions of similar fluorescence intensity as the initial sodium cholate solution, while in the case of lipid-C_{61}-PEG, a variable degree of quenching is observed, which appears to be greater for large band-gap semiconductors. For pyrene-PEG, a fluorescence quenching pattern is observed which does not have an apparent band-gap dependence. This quenching is substantially enhanced on the addition of the methanofullerene moiety, resulting in near-complete quenching of the fluorescence across all species.

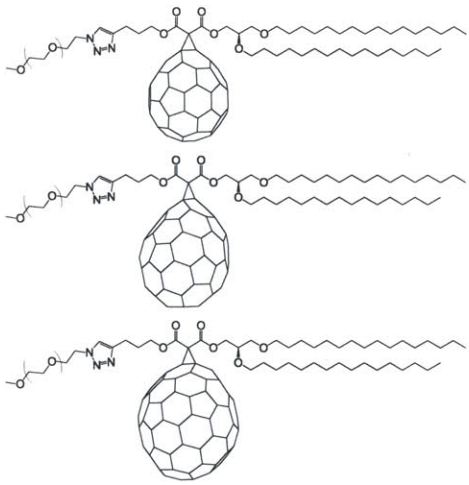

Figure 4.5. Fullerene family analysis. Top to bottom – methanofullerenes based on C_{60}, C_{70}, and C_{84}.

Fullerene Family Analysis

In addition to analyzing the influence of the fullerene-SWCNT interface on the relative fluorescence quantum yield, two additional lipid-fullerene amphiphiles were synthesized based on C_{71} and C_{85} methanofullerenes (figure 4.5). Using these species, we sought to investigate how the SWCNT quantum yield is influenced by the energy states of the fullerene derivative.

Excitation-emission spectra for the C_{71} and C_{85} fullerene systems are shown in Fig. 4.6. Here it is apparent that, like the C_{61} derivative, the C_{71} moiety produces incomplete fluorescence

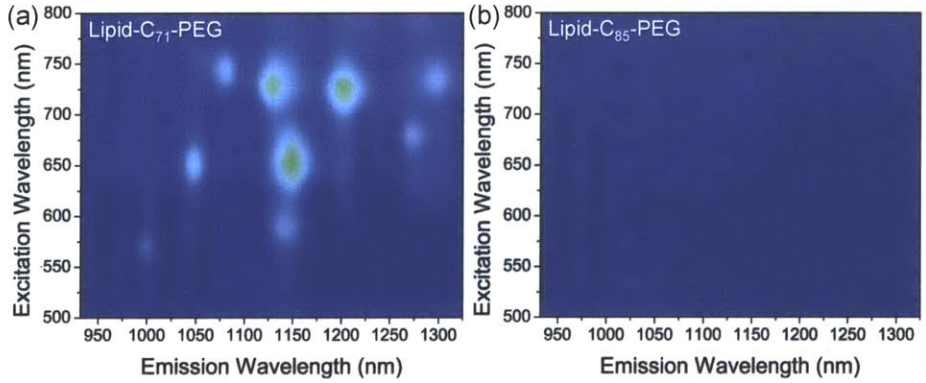

Figure 4.6 Excitation-emission plots for SWCNTs suspended in (a) lipid-C_{71}-PEG and (b) lipid-C_{85}-PEG. Plots are depicted on the same scale. In the case of Lipid-C_{85}-PEG, no significant fluorescence was observed above background.

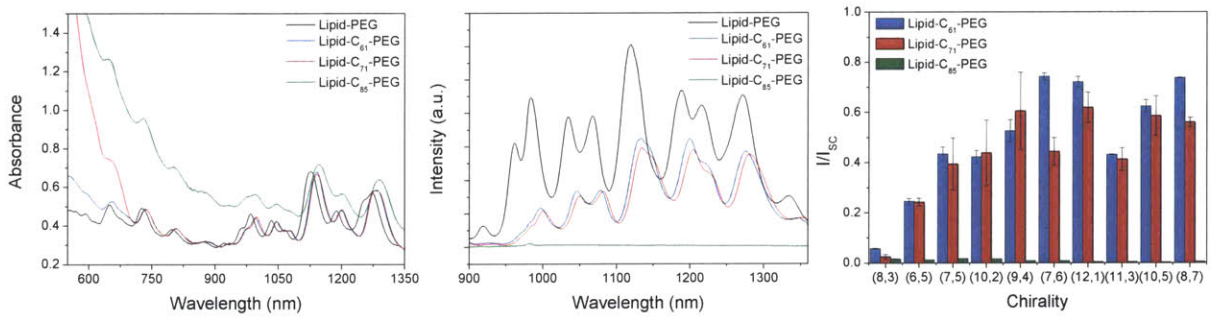

Figure 4.7. Absorbance and fluorescence results from fullerene family analysis. (a) Absorbance spectra of SWCNT suspensions in lipid-PEG, as well as the C_{61}, C_{71}, and C_{85} methanofullerenes. (b) Averaged fluorescence spectra (3 samples) for these amphiphilic systems, acquired at an excitation wavelength of 785nm. (c) Deconvoluted relative intensities, normalized to the intensities of SC-SWCNT, for the three lipidic methanofullerenes.

quenching across all species. In contrast, the introduction of C_{85} to the surfactant results in complete fluorescence quenching across all species. Absorbance and fluorescence spectra for the three lipidic methanofullerene derivatives are presented in Figure 4.7. While the C_{61} and C_{71} adducts display similar absorbance spectra, it is apparent that the absorbance of C_{85} methanofullerene extends into the nIR region, resulting in an increased sample baseline. In addition, the C_{85} sample exhibits a higher degree of peak broadening compared to the other methanofullerene species, which we attribute to inhomogeneous broadening that results from the presence of multiple isomers of C_{85} monoadducts. The fluorescence spectra in figure 4.7(b), acquired at an excitation wavelength of 785nm, show similar degrees of quenching for the C_{61} and C_{71} methanofullerenes, but a complete quenching of nanotube fluorescence across all species in the case of the C_{85} adduct. These results are shown more quantitatively in the deconvoluted relative intensities, which are presented in figure 4.7(c).

4.5 Discussion

Evaluating the SWCNT-Surfactant Interface

In an aqueous surfactant system, SWCNTs that are exposed to water can be quenched by a variety mechanisms, including sidewall protonation[168], or interaction with oxygen[169] and reactive oxygen species[48, 170]. Therefore, in order to better understand the observed differences in fluorescence behavior for these amphiphilic systems, we sought to quantify the percentage of the SWCNT surface that is exposed to the aqueous environment.

It has previously been shown that the solvatochromic shifts of the SWCNT optical transitions are dependent upon the local SWCNT dielectric environment by the following relation[171]:

$$\Delta E_{ii} = -L\frac{\Delta\alpha_{ii}}{R^3}\left[\frac{2(\varepsilon-1)}{2\varepsilon+1}-\frac{2(n^2-1)}{2n^2+1}\right] \tag{4.1}$$

in which L is a fluctuation factor, ε is the local dielectric constant, n is the refractive index, R is the nanotube radius, and $\Delta\alpha_{11}$ is the change in polarizability of SWCNTs upon excitation from the ground to excited state. This difference in polarizability is predominantly determined by the longitudinal polarizability of the exciton, allowing for $\Delta\alpha_{11}$ to be approximated by $\alpha_{11,\|}$[171]. Using a longitudinal polarizability of the form $\alpha_{11} \propto 1/(RE_{11}^2)$, the following equation is obtained[171]:

$$(E_{ii})^2\Delta E_{ii} = -K\left[\frac{2(\varepsilon-1)}{2\varepsilon+1}-\frac{2(n^2-1)}{2n^2+1}\right]\left(\frac{1}{R^4}\right)=\frac{c}{R^4} \tag{4.2}$$

In order to quantify surface coverages, it is necessary to utilize a single-component system, with a known dielectric constant and refractive index, as a reference. We utilized n-methyl-2-pyrrolidone (NMP) as a reference system, which has a dielectric constant of 32.2 and a refractive index of 1.47. From Choi et. al.[171], we know that for NMP, the plot of $(E_{11})^2\Delta E_{11}$ vs. $1/d^4$ gives a slope of c = 0.053 eV^3nm^4.

Using this reference system, we first analyzed the surface coverage in the lipid-PEG and pyrene-PEG suspensions. From the excitation-emission map of the lipid-PEG SWCNT dispersion, we plotted $(E_{11})^2\Delta E_{11}$ vs. $1/d^4$ to obtain a slope of 0.0517 eV^3nm^4. Using this value, along with the information from NMP, and assuming that the refractive index of surfactant-dispersed SWCNTs is equal to that of water (1.333), it is possible to evaluate the local dielectric constant of the lipid-PEG SWCNT system using the following relation:

$$\frac{c_2}{c_1}=\frac{\left(\frac{2(\varepsilon_2-1)}{2\varepsilon_2+1}-\frac{2(n_2^2-1)}{2n_2^2+1}\right)}{\left(\frac{2(\varepsilon_1-1)}{2\varepsilon_1+1}-\frac{2(n_1^2-1)}{2n_1^2+1}\right)} \tag{4.3}$$

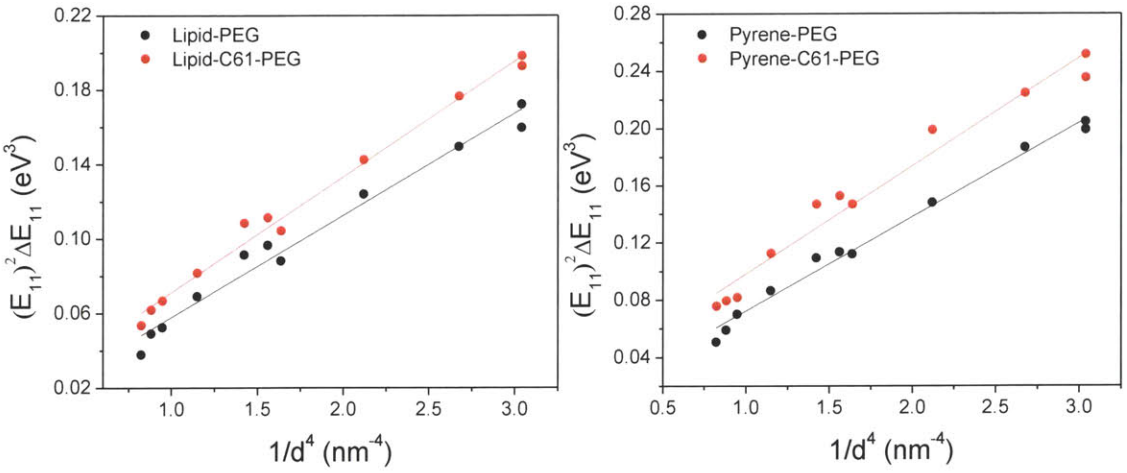

Figure 4.8 Plots of $(E_{11})^2\Delta E_{11}$ versus $1/d^4$, evaluated from deconvoluted absorbance spectra, for the lipid-PEG, lipid-C_{61}-PEG, pyrene-PEG, and pyrene-C_{61}-PEG. The slopes of these curves were used to predict the fractional coverage of methanofullerene on the SWCNT surface.

Here, subscripts 1 and 2 refer to properties associated with the NMP and lipid-PEG systems, respectively. Solving this equation, we get a local dielectric constant of 6.56 for the lipid-PEG suspension. Assuming that the local dielectric constant in this system is comprised of contributions from the lipid segment and water:

$$\bar{\varepsilon} = x_1\varepsilon_{lipid} + (1-x_1)\varepsilon_{H_2O} \tag{4.4}$$

we can evaluate the surface coverage of the lipid molecule on the SWCNT surface. For the lipidic segment, we assumed a lipidic dielectric constant of 2.08, which corresponds to that of hexadecane[172]. This value gives a 94.3% surface coverage of the lipidic moiety, corresponding to a 5.7% surface coverage of water. These values are very close to the recently estimated surfactant surface coverage for sodium cholate suspended SWCNTs of 93 ± 15% [173], explaining the similarity in fluorescence intensity for these two systems. For the pyrene-PEG system, ε_{pyrene} was taken to be 3.19, which is the average of the three primary tensor components in pyrene crystals[174]. Using this value, the surface coverages of pyrene and water were determined to be 89.2% and 10.8%, respectively. In this system, the similarity in water surface coverage to that of sodium cholate indicates that the pyrene moiety appears to be responsible for partial quenching of the SWCNT fluorescence.

Due to the fact that the lipid-C_{85}-PEG and pyrene-C_{61}-PEG systems have complete or near-complete quenching of the SWCNT fluorescence, we then utilized the local dielectric constant of the lipid-PEG system, along with solvatochromic shifts in the absorbance spectra (as

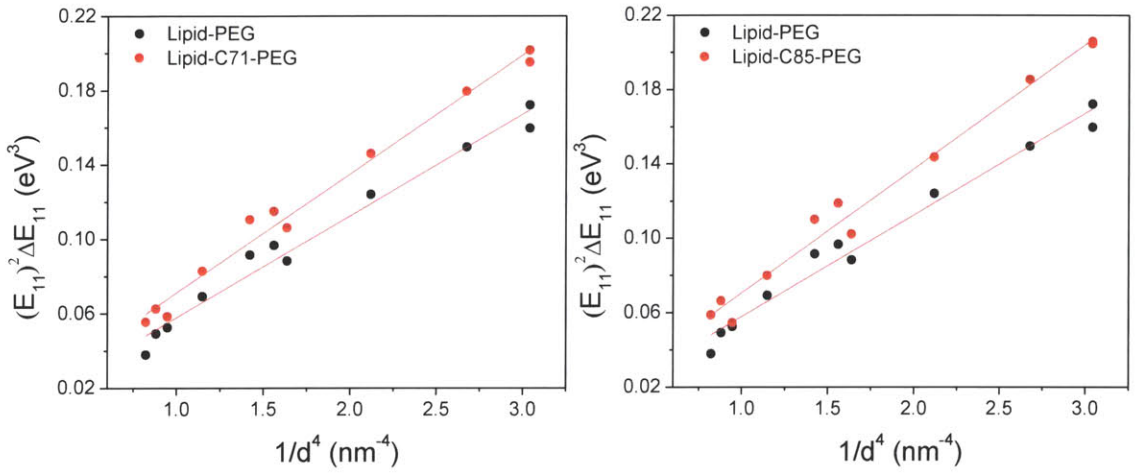

Figure 4.9 Plots of $(E_{11})^2\Delta E_{11}$ versus $1/d^4$ for the lipid-C_{71}-PEG and lipid-C_{85}-PEG, with lipid-PEG shown for reference. The slopes of these curves were used to predict the fractional coverage of methanofullerene on the SWCNT surface.

opposed to fluorescence spectra) to deduce information about the surface coverage of water in each surfactant system. Plots of $(E_{11})^2\Delta E_{11}$ vs. $1/d^4$, obtained by deconvoluting absorbance data, are provided in Figures 4.8 and 4.9. In order to verify that the utilization of absorption spectra produces similar results to those obtained via fluorescence, we also evaluated the pyrene surface coverage using solvatochromic shifts from absorbance data. This analysis yielded a pyrene surface coverage of 89.0%, which is in close agreement with the results from fluorescence measurements. Because there are three components in all of the other surfactant systems: lipid-C_{61}-PEG, lipid-C_{71}-PEG, lipid-C_{85}-PEG, and pyrene-C_{61}-PEG, we were unable to solve for each of the components, directly, but were able to bound the quantity of water on the surface, due to its high static dielectric constant. For example, in order to do this for the lipid-C_{61}-PEG system, in which the local dielectric constant is specified by:

$$\bar{\varepsilon} = x_1\varepsilon_{lipid} + x_2\varepsilon_{C60} + (1 - x_1 - x_2)\varepsilon_{H_2O} \tag{4.5}$$

we sequentially set x_1 and x_2 to zero, and then solved for the coverage of the other two components. In performing the analysis, the dielectric constants of C_{61}, C_{71}, and C_{85} were taken to be 3.6 [175], 3.75 [176], and 5.5 [177], respectively.

The resulting bounds for the surface coverage of water, in each surfactant system, are given in Table 4-1. These results indicate similar coverages of water in the cases of lipid-C_{61}-PEG, lipid-C_{71}-PEG, and lipid-C_{85}-PEG, suggesting that water cannot be responsible for the differences in fluorescence quenching observed among these surfactant systems. In the case of the pyrene-PEG system, the similarity in water surface coverage to that of sodium cholate

Table 4-1 Quantifying Exposed Surface Area

Surfactant System	Estimated Water Coverage
2%SC [3]	7%
Lipid-PEG	5.7%
Pyrene-PEG	10.8%
Pyrene-C_{61}-PEG	39.0-39.3%
Lipid-C_{61}-PEG	7.3-9.1%
Lipid-C_{71}-PEG	8.8-10.8%
Lipid-C_{85}-PEG	9.8-13.7%

indicates that the pyrene moiety partially quenches the SWCNT fluorescence. In comparing the lipid-C_{61}-PEG and pyrene-C_{61}-PEG systems, the pyrene-C_{61}-PEG system has a much higher surface coverage of water. Therefore, it is likely a combination of both the pyrene moiety and increased water coverage that results in enhanced fluorescence quenching for the pyrene-C_{61}-PEG derivative. In the cases of lipid-C_{61}-PEG, pyrene-C_{61}-PEG, and lipid-C_{71}-PEG, the observed band-gap dependent quenching behavior, arises from the fact that, as the band-gap of the nanotube decreases, the energy offset that drives electron transfer from SWCNT to the fullerene also decreases[39].

Quantifying Donor-Acceptor Energy Offsets

In order to verify that electron transfer is responsible for SWCNT fluorescence quenching, we attempted to fit the lipid-C_{61}-PEG and lipid-C_{71}-PEG fluorescence data using a Marcus theory model. Due to the incomplete fluorescence quenching in the cases of the lipid-C_{61}-PEG and lipid-C_{71}-PEG derivatives, it was possible to utilize the relative degrees of quenching to infer information about the relative rates of electron transfer between excited-state SWCNTs and fullerenes. This is because, among competing excited-state decay pathways in SWCNT, the selectivity toward a particular pathway – in this case electron transfer to fullerene – will be proportional to the rate constant associated with that pathway. Since energy transfer ultimately diverts an electron from the radiative decay pathway, fractional quenching results can be utilized as an approximation for the rate constant of electron transfer. If the fractional quenching is normalized to a particular chirality, such as (6,5), it is possible to approximate relative rate constants for electron transfer as:

$$\left(\frac{k_{et}^{(n,m)}}{k_{et}^{(6,5)}}\right)_{expt} = \frac{1-(I/I_o)_{(n,m)}}{1-(I/I_o)_{(6,5)}} \tag{4.6}$$

According to Marcus theory, the rate constant associated with electron transfer from SWCNT to the LUMO level of fullerene can be represented as[55]:

$$k_{et} = \frac{2\pi}{\hbar\sqrt{4\pi\lambda k_b T}} V_R^2 \exp\left(-\Delta G^{\ddagger}_{(n,m)} / kT\right) = \frac{2\pi}{\hbar\sqrt{4\pi\lambda k_b T}} V_R^2 \exp\left(-\frac{\left(\lambda + \Delta G^{o}_{(n,m)}\right)^2}{4\lambda kT}\right) \tag{4.7}$$

In which V_R^2 is an electronic coupling term between the initial and final states, λ is the reorganization energy, and $\Delta G^{o}_{(n,m)}$ is total change in Gibbs free energy for the electron transfer event. The change in Gibbs free energy is related to the energy difference between the SWCNT conduction band and the LUMO level of the methanofullerene by the following relation:

$$\Delta G^{o}_{(n,m)} = -\left(E^{c}_{(n,m)} - E^{LUMO}\right) \tag{4.8}$$

If we assume that the electronic coupling term is invariant across nanotube species, relative rate constants of electron transfer can be evaluated, allowing for direct comparison with experimental fractional quenching results:

$$\left(\frac{k_{et}^{(n,m)}}{k_{et}^{(6,5)}}\right)_{theory} = \frac{\exp\left(-\Delta G^{\ddagger}_{(n,m)} / kT\right)}{\exp\left(-\Delta G^{\ddagger}_{(6,5)} / kT\right)} \tag{4.9}$$

The Marcus theory expression in this equation is only dependent upon the reorganization energy of electron transfer and the energy offsets between the fullerene LUMO and the SWCNT conduction bands. SWCNT conduction band energies, referenced to the standard hydrogen electrode (SHE), have been reported in the literature for several chiralities[56]. These values were converted to absolute potential using the relation: $E_{\text{abs}}(\text{V}) = -(E_{SHE}(\text{V}) + 4.44\ \text{V})$ [178], and are reported in the second column of Table 4-2. Additionally, reorganization energies for fullerene-based electron transfer systems have been reported to be between 0.23-0.77eV[57-60]. Here, we sought to bound the energy offset $\Delta G^{o}_{(n,m)}$ between SWCNTs and the fullerenes in this

Table 4-2 Predicted Donor-Acceptor Energy Offsets for Different Fullerenes and Reorganization Energies

			Energy Offset, ΔG_o (eV)					
			C_{61}		C_{71}		C^{*}_{85}	
Chirality	$E_c^{(n,m)}$ †	$E_b^{(n,m)}$ ‡	$E^{LUMO}_{\lambda=0.23}$ = -3.95	$E^{LUMO}_{\lambda=0.51}$ = -4.05	$E^{LUMO}_{\lambda=0.23}$ = -4.00	$E^{LUMO}_{\lambda=0.51}$ = -4.14	$E^{LUMO}_{\lambda=0.23}$ = -4.30	$E^{LUMO}_{\lambda=0.51}$ = -4.40
(8,3)	-3.83	0.38	0.12	0.22	0.17	0.31	0.47	0.57
(6,5)	-3.85	0.40	0.10	0.20	0.15	0.29	0.45	0.55
(7,5)	-3.86	0.36	0.09	0.19	0.14	0.28	0.44	0.54
(10,2)	-3.86	0.34	0.09	0.19	0.14	0.28	0.44	0.54
(9,4)	-3.90	0.33	0.05	0.15	0.10	0.24	0.40	0.50
(7,6)	-3.90	0.34	0.05	0.15	0.10	0.24	0.40	0.50
(12,1)	-3.93	0.30	0.02	0.12	0.07	0.21	0.37	0.47
(11,3)	-3.90	0.30	0.05	0.15	0.10	0.24	0.40	0.50
(10,5)	-3.91	0.29	0.04	0.14	0.09	0.23	0.39	0.49
(8,7)	-3.91	0.29	0.04	0.14	0.09	0.23	0.39	0.49

†E_c values were utilized from Tanaka et. al.[56]. ‡The exciton binding energy of SWCNTs was approximated by $E_b = 0.3/d_t$ where d_t is the diameter of the nanotube [184]. *LUMO levels of C_{85} were approximated by assuming a 0.35eV energy offset relative to C_{61} [44].

study using the Marcus theory equation above. To do so, we utilized a reorganization energy of 0.23eV [60] as a lower limit, with an upper limit of 0.51eV, which has specifically been observed for fullerene-based dyads with short donor-acceptor linkages[57]. Using experimental fractional quenching results, we then fit the effective fullerene LUMO level, E^{LUMO}, thereby allowing for determination of $\Delta G^{o}_{(n,m)}$. The fitted LUMO levels for C_{61} and C_{71} are provided in Table 4-2 for assumed reorganization energies of both 0.23 and 0.51eV. The LUMO level of C_{85} was then deduced, using the values from C_{61}, by assuming that the LUMO level of C_{85} is 0.35eV lower than that of C_{61}[44].

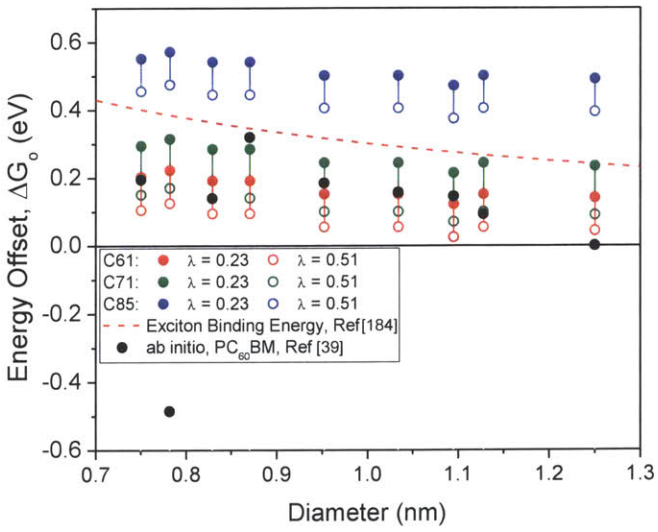

Figure 4.10 Predicted energy offsets between SWCNT conduction bands and the C_{61} LUMO level. Offsets were evaluated using the C_{61} LUMO level determined from Marcus theory. The data are compared with *ab initio* values reported in Ref [39] for $PC_{61}BM$.

The predicted LUMO levels for C_{61} (-3.95 to -4.05 eV) deviate slightly from the values of -1.028 to -1.08 V vs. Fc/Fc+ or approximately -3.85 to -3.8 eV (using the conversion, $\mathrm{LUMO} = -e(4.88\ \mathrm{V} + E^{Fc/Fc+}_{\mathrm{red}})$ [179]) that have been previously reported for C_{60} monoadducts[44, 180, 181]. However, as shown in Figure 4.10, the fitted LUMO levels result in

Table 4-3. Comparison Between Experimental and Theoretical Relative Rate Constants of Electron Transfer

Summary of Relative Rate Constant Results, $k^{(n,m)}_{ET} / k^{(6,5)}_{ET}$

		C_{61}			C_{71}		
			Marcus Theory			Marcus Theory	
Chirality	Diameter	Experimental	$E^{LUMO}_{\lambda=0.23}$ = -3.96	$E^{LUMO}_{\lambda=0.51}$ = -4.06	Experimental	$E^{LUMO}_{\lambda=0.23}$ = -3.99	$E^{LUMO}_{\lambda=0.51}$ = -4.12
(8,3)	0.782	1.25 ± 0.01	1.21	1.25	1.22 ± 0.01	1.15	1.19
(6,5)	0.757	1.00 ± 0.05	1.00	1.00	1.00 ± 0.02	1.00	1.00
(7,5)	0.829	0.76 ± 0.03	0.90	0.89	0.77 ± 0.14	0.92	0.91
(10,2)	0.884	0.79 ± 0.03	0.90	0.89	0.76 ± 0.17	0.92	0.91
(9,4)	0.916	0.53 ± 0.04	0.53	0.53	0.62 ± 0.14	0.60	0.60
(7,6)	0.895	0.53 ± 0.04	0.53	0.53	0.62 ± 0.14	0.60	0.60
(8,6)	0.965	0.45 ± 0.03	0.46	0.47	0.53 ± 0.08	0.53	0.54
(11,3)	1.014	0.65 ± 0.02	0.53	0.53	0.74 ± 0.06	0.60	0.60
(10,5)	1.050	0.46 ± 0.02	0.46	0.47	0.51 ± 0.07	0.53	0.54
(8,7)	1.032	0.46 ± 0.02	0.46	0.47	0.51 ± 0.07	0.53	0.54

SWCNT-fullerene energy offsets, $\Delta G^{o}_{(n,m)}$, that are in good agreement with *ab initio* results which incorporate polarization effects at the SWCNT-fullerene interface[39]. Therefore, we anticipate that electronic interactions are also responsible for the deviation in the current case. Experimentally, nearly identical LUMO levels to C_{61} have been observed for C_{71}[44, 181], due to the similarity in electronic properties of these two fullerenes[182], and this is consistent with the overlap in the offsets which results from our model.

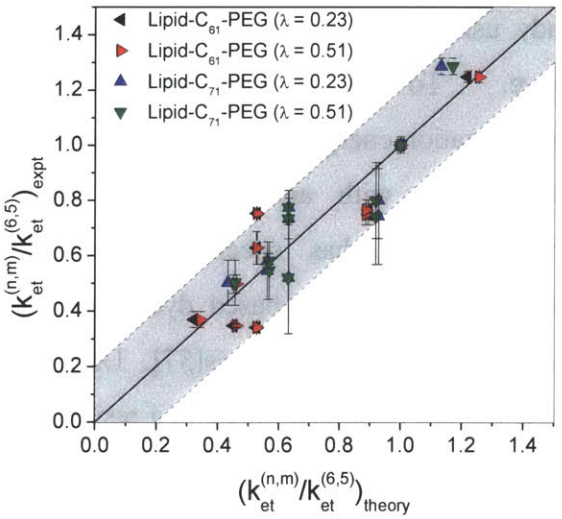

Figure 4.11. Parity plot showing the agreement between experimental and theoretical relative rate constants for different values of the reorganization energy.

In organic photovoltaics, it is generally accepted that LUMO-LUMO offsets greater than the exciton binding energy are necessary in order to enable efficient interfacial energy transfer[183]. As shown in Fig 4.10, in the case of C_{61} and C_{71} derivatives, both systems possess energy offsets that fall below the exciton binding energy of SWCNTs, which was approximated by $E_b = 0.3/d_t$[184]. This is likely the reason for inefficient fluorescence quenching of nanotubes in these two systems. In contrast, the deeper LUMO level of C_{85} results in energy offsets greater than the exciton binding energy, resulting in energetically favorable electron transfer, and complete fluorescence quenching across all nanotube species. However, the results for the C_{85} derivative are complicated by the fact that this fullerene adduct has an absorbance component that extends beyond 785nm, which is the excitation wavelength utilized in this study. Therefore, follow-up work on the dynamics of this interface will provide greater insight into the electronic coupling between these species.

In order to assess the validity of applying a Marcus theory model to this system, we plotted the experimentally determined relative rate constants of electron transfer versus those predicted by theory. The resulting parity plot is presented in Fig. 4.11, and a direct comparison of experimental and theoretical values is provided in Table 4-3. As can be seen from the plot, good agreement is observed between experimental and theoretical results.

4.6 Conclusions

In order to examine electron transfer at the interface between SWCNTs and fullerenes, we synthesized a series of methanofullerene surfactants. For all amphiphiles studied here, with the exception of the methyl-C_{61}-PEG derivative, high quality dispersions of individual nanotubes were obtained upon surfactant exchange from 2% sodium cholate. In the cases of lipid-C_{61}-PEG and lipid-C_{71}-PEG, which are predicted to similar surfactant surface coverages, band-gap dependent, incomplete quenching was observed across all semiconducting species. In the case of pyrene-C_{61}-PEG, near-complete quenching was observed, which could be attributed to partial quenching by the pyrene moiety, as well as significant exposure of the SWCNT surface to the aqueous environment. The incomplete quenching in the cases of lipid-C_{61}-PEG and lipid-C_{71}-PEG indicate that the driving force for excited-state electron transfer is small in these systems. This is further supported by a Marcus theory model, which predicts that the energy offsets between the SWCNT conduction bands and the fullerene LUMO levels are less than the SWCNT exciton binding energy. In contrast, the lipid-C_{85}-PEG derivative shows complete quenching of all SWCNT species utilized in this work. This enhancement in quenching efficiency is consistent with the fact that the LUMO level of C_{85} methanofullerene is approximately 0.35eV lower than that of the smaller fullerene adducts, resulting in energy offsets which exceed the exciton binding energy. This result, combined with the fact that C_{85} has much higher photo-stability than C_{61} and C_{71}, makes this larger fullerene adduct a promising candidate for SWCNT-based sensors and photovoltaics.

4.7 Synthesis

Synthesis of ***3-oxo-3-(pent-4-yn-1-yloxy)propanoic acid (1)***

To a thoroughly dried reaction vessel, equipped with a reflux condenser, was added 4.65g (0.032 moles) of Meldrum's acid. The ambient atmosphere was replaced with nitrogen before adding 3 mL of 4-pentyn-1-ol (0.032 moles), followed by 120 mL of anhydrous toluene. The solution was refluxed for 2 hours, or until TLC indicated completion of the reaction. Toluene was then removed under reduced pressure, and the resulting residue was purified by column chromatography (DCM:MeOH), eluting on a gradient from 40:1 to 20:1. Removal of solvent yielded a clear liquid which solidified upon standing. Yield: 4.25g (77%).

Synthesis of ***(R)-2,3-bis(hexadecyloxy)propyl pent-4-yn-1-yl malonate (2)***

0.315 g (1.849mmol) of compound (1), 1.0 g (2.218mmol) of 1,2-O-dihexadecyl-sn-glycerol, and 47 mg (0.388mmol) of DMAP were dissolved in anhydrous dichloromethane (8mL) and cooled in an ice bath. The ambient atmosphere was replaced with N_2, and a solution of *N,N'*-dicyclohexylcarbodiimide (0.381g, 1.849mmol) in 4mL anhydrous DCM was added dropwise. The solution was reacted at 0°C for 2 hours, allowed to warm to room temperature, and reacted

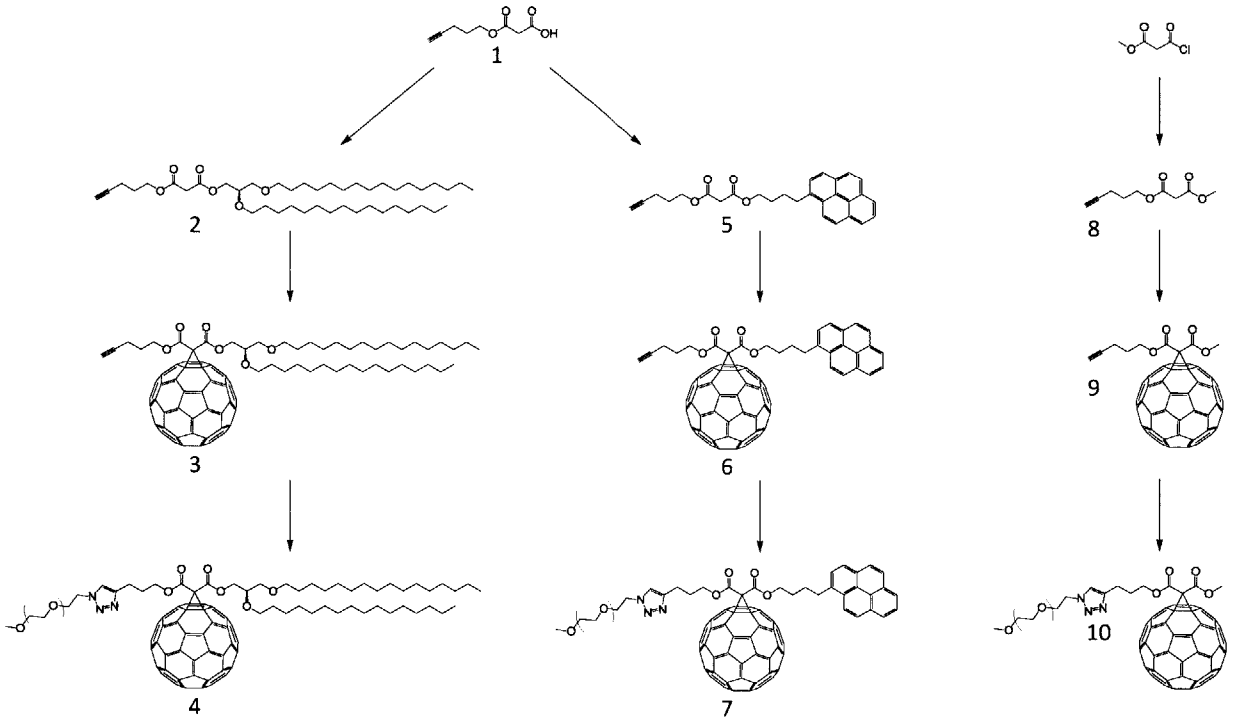

Scheme 4-1 Synthetic scheme for PEGylated methanofullerenes 4, 7, and 10.

overnight. The insoluble urea was filtered off, solvent removed, and the crude product purified by column chromatography, eluting with dichloromethane, to give the product as a white solid. Yield: 1.02g (80%).

Synthesis of ***(3)***

Anhydrous toluene (75mL) was added to 0.39g (541 μmol) of C60-fullerene and 0.25g (361 μmol) of compound **(2)**, and the resulting suspension was bubbled with nitrogen. The reaction vessel was surrounded with foil, and iodine (0.101g, 398μmol) was added. Under a nitrogen atmosphere, a solution of 1,8-diazabicyclo[5.4.0]undec-7-ene (DBU) – 70uL DBU (466μmol) in 50mL anhydrous toluene – was added dropwise over 1-2 hours. After complete addition, the solution was allowed to stir 24 hours. Solvent was removed in the presence of silica gel and the product purified by column chromatography, eluting on a gradient from 3:1 to 1:1 Hexanes:Toluene. Removal of solvent gave the product as a brown solid (211mg, 41%). The C71 and C85 analogues were synthesized in a similar manner.

Synthesis of methanofullerene ***(4)*** *- Lipid-C61-PEG*

Compound **(3)** (25mg, 17.7μmol) and mPEG-N_3-5kDa (177mg, 35.4 μmol) were dissolved in 1mL of dichloromethane, and 1mL of water was subsequently added. Then Cu(0) – 1-2 pieces – was added, followed by $CuSO_4$ (1.1mg, 4.4μmol) and sodium ascorbate (1.75mg, 8.83μmol). The resulting mixture was allowed to react at room temperature overnight under vigorous stirring. The reaction mixture was diluted with dichloromethane and washed with water. The organic layer was then dried and filtered through a short plug of regular-phase silica gel (DCM). Eluting with DCM, the PEGylated product remains immobilized, while unreacted **(3)** is eluted. The crude PEGylated product can then be eluted using 4:1 DCM:MeOH. After removal of unreacted **(3)**, the PEGylated product was purified by reversed-phase chromatography, eluting on a gradient from 4:1 to 3:2 MeOH:DCM. Removal of solvent gave the product as a brown solid (73mg, 64%). The C71 and C85 analogues were synthesized in a similar manner.

Synthesis of ***pent-4-yn-1-yl (4-(pyren-1-yl)butyl) malonate (5)***

0.372 g (2.187mmol) of compound (1), 0.6 g (2.624mmol) of 1-Pyrenebutanol, and 56 mg (0.459mmol) of DMAP were dissolved in anhydrous dichloromethane (10mL) and cooled in an

ice bath. The ambient atmosphere was replaced with N_2, and a solution of *N,N'*-dicyclohexylcarbodiimide (0.451g, 2.187mmol) in 5mL anhydrous DCM was added dropwise. The solution was reacted at 0°C for 2 hours, allowed to warm to room temperature, and reacted overnight. The insoluble urea was filtered off, and the solvent removed in the presence of silica gel. The product-containing silica gel was carefully added to the top of a pre-packed column, and purified by eluting with 6:1 Hexanes:Ethyl Acetate to give the product as a white to off-white solid (0.81g, 87%).

Synthesis of ***(6)***

Anhydrous toluene (75mL) was added to 0.38g (0.527 mmol) of C60-fullerene and 0.15g (0.352 mmol) of compound **(5)**, and the resulting suspension was bubbled with nitrogen. The reaction vessel was surrounded with foil, and iodine (0.098g, 0.386mmol) was added. Under a nitrogen atmosphere, a solution of 1,8-diazabicyclo[5.4.0]undec-7-ene (DBU) – 68uL DBU (0.460mmol) in 50mL anhydrous toluene – was added dropwise over 1-2 hours. After complete addition, the solution was allowed to stir 24 hours. Solvent was removed in the presence of silica gel and the product purified by column chromatography, eluting on a gradient from 3:1 to 1:1 Hexanes:Toluene. Removal of solvent gave the product as a brown solid (181mg, 45%).

Synthesis of ***(7)*** *- Pyrene-C61-PEG*

Compound **(6)** (20mg, 17.5μmol) and mPEG-N_3-5kDa (175mg, 35μmol) were dissolved in 1mL of dichloromethane, and 1mL of water was subsequently added. Then Cu(0) – 1-2 pieces – was added, followed by $CuSO_4$ (1.1mg, 4.4μmol) and sodium ascorbate (1.73mg, 8.73μmol). The resulting mixture was allowed to react at room temperature overnight under vigorous stirring. The reaction mixture was diluted with dichloromethane and washed with water. The organic layer was then dried and filtered through a short plug of regular-phase silica gel (DCM). Eluting with DCM, the PEGylated product remains immobilized, while unreacted **(6)** is eluted. The crude PEGylated product can then be eluted using 4:1 DCM:MeOH. After removal of unreacted **(6)**, the PEGylated product was purified by reversed-phase chromatography, eluting on a gradient from 8:1 to 4:1 MeOH:DCM. Iodine vapor was used as a TLC developing agent. Removal of solvent gave the product as a brown solid (63mg, 59%).

Synthesis of ***methyl pent-4-yn-1-yl malonate (8)***

4-pentyn-1-ol (0.607mL, 6.5mmol) and triethylamine (1.09mL, 7.83mmol) were added to 15mL of anhydrous dichloromethane. The ambient atmosphere was replaced with N_2 and the solution was cooled in an ice bath. Methyl-3-chloro-3-oxopropionate (0.70mL, 6.52mmol) was added dropwise, and the reaction solution was stirred at 0°C for 30 minutes, then warmed to room temperature and stirred an additional 24 hours. Water was added, the organic layer collected, and the aqueous layer extracted with 3 volumes of ethyl acetate. The combined organic fractions were washed with sodium bicarbonate and brine, dried over $MgSO_4$, and the solvent removed under vacuum. The crude product was purified by column chromatography (DCM) to give the product as a colorless to light yellow oil (0.972g, 81%).

*Synthesis of **(9)***

Anhydrous toluene (120mL) was added to 0.646g (0.896 mmol) of C60-fullerene and 0.11g (0.597 mmol) of compound **(8)**, and the resulting suspension was bubbled with nitrogen. The reaction vessel was surrounded with foil, and iodine (0.167g, 0.776mmol) was added. Under a nitrogen atmosphere, a solution of 1,8-diazabicyclo[5.4.0]undec-7-ene (DBU) – 116uL DBU (0.775mmol) in 90mL anhydrous toluene – was added dropwise over 1-2 hours. After complete addition, the solution was allowed to stir 24 hours. Solvent was removed in the presence of silica gel and the product purified by column chromatography, eluting on a gradient from 3:1 to 1:1 Hexanes:Toluene. Removal of solvent gave the product as a brown solid (189mg, 35%).

*Synthesis of methanofullerene **(10)** - Methyl-C61-PEG*

Compound **(9)** (15mg, 16.6μmol) and mPEG-N_3-5kDa (166mg, 33.2μmol) were dissolved in 1mL of dichloromethane, and 1mL of water was subsequently added. Then Cu(0) – 1-2 pieces – was added, followed by $CuSO_4$ (1.04mg, 4.2μmol) and sodium ascorbate (1.65mg, 8.33μmol). The resulting mixture was allowed to react at room temperature overnight under vigorous stirring. The reaction mixture was diluted with dichloromethane and washed with water. The organic layer was then dried and filtered through a short plug of regular-phase silica gel (DCM). Eluting with DCM, the PEGylated product remains immobilized, while unreacted **(9)** is eluted. The crude PEGylated product can then be eluted using 4:1 DCM:MeOH. After removal of unreacted **(9)**, the PEGylated product was purified by reversed-phase chromatography, eluting on

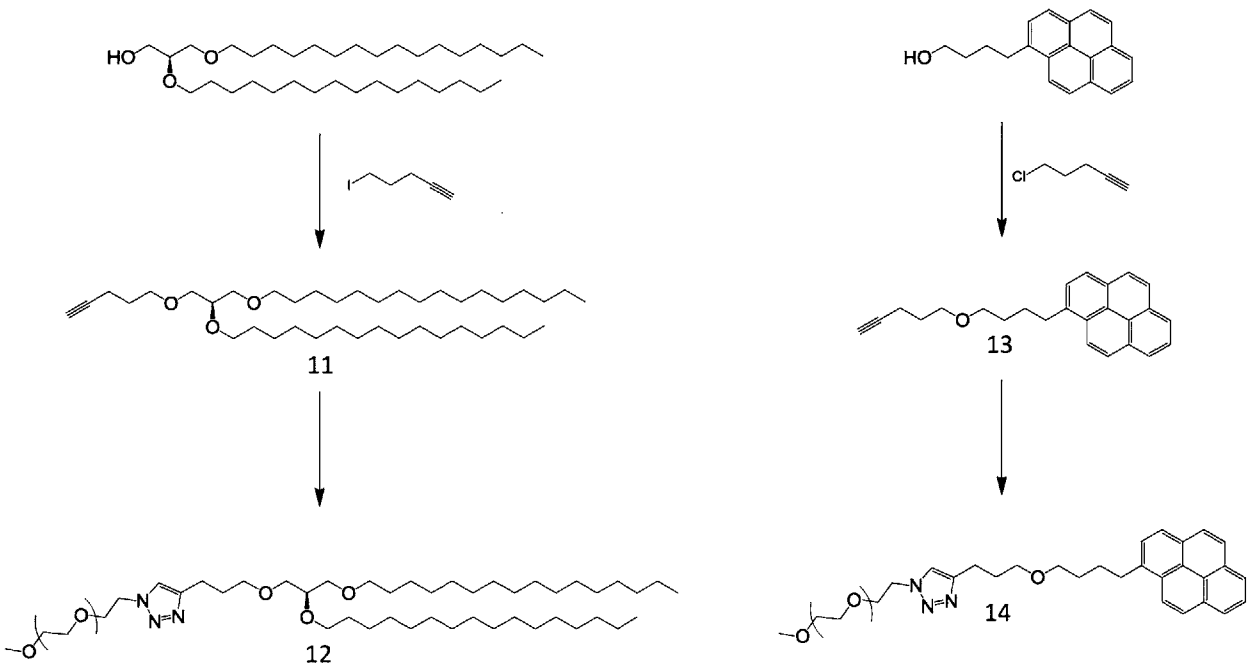

Scheme 4-2 Synthetic scheme for control molecules 12 and 14.

a gradient from 8:1 to 5:1 MeOH:DCM. Iodine vapor was used as a TLC developing agent. Removal of solvent gave the product as a brown solid (50mg, 51%).

Synthesis of ***(R)-1-((1-(hexadecyloxy)-3-(pent-4-yn-1-yloxy)propan-2-yl)oxy)hexadecane (11)***

Sodium hydride (44.4mg, 1.85mmol) was placed in a reaction flask, and the ambient atmosphere replaced with nitrogen. A solution of 1,2-O-dihexadecyl-sn-glycerol (0.50g, 0.924mmol) in anhydrous THF (5mL) was then added. After 30 minutes, a solution of 1-Iodo-4-pentyne (0.210mL, 1.85mmol) in anhydrous THF (5mL) was added. The solution was heated to reflux, and allowed to react for 2 hours. The reaction was quenched with water (10mL), and the crude product extracted with DCM (3x). The combined organic layers were dried, and the solvent removed under reduced pressure. The residue was purified by column chromatography (20:1 Hexanes:Ethyl Acetate) to give the product as a colorless, viscous oil (65mg, 12%).

Synthesis of ***(12)*** *– Lipid-PEG*

Compound **(11)** (21.2mg, 0.035mmol) and mPEG-N_3-5kDa (262mg, 0.052mmol) were dissolved in 1mL of dichloromethane, and 1mL of water was subsequently added. Then Cu(0) – 1-2 pieces – was added, followed by $CuSO_4$ (2.18mg, 8.7μmol) and sodium ascorbate (3.46mg, 17.4μmol). The resulting mixture was allowed to react at room temperature overnight under vigorous

stirring. The reaction mixture was diluted with dichloromethane and washed with water. The organic layer was then dried, and the solvent removed under reduced pressure. The crude product was purified by reversed phase chromatography, eluting with 9:1 MeOH:DCM. Iodine vapor was used as a TLC developing agent. Removal of the solvent gave the product as a white solid (96mg, 49%).

*Synthesis of **1-(4-(pent-4-yn-1-yloxy)butyl)pyrene (13)***

Sodium hydride (70mg, 2.92mmol) was placed in a reaction flask, and the ambient atmosphere replaced with nitrogen. A solution of 1-pyrenebutanol (0.40g, 1.46mmol) in anhydrous DMF (4mL) was then added. After 30 minutes, a solution of 1-Chloro-4-pentyne (0.463mL, 4.4mmol) in anhydrous DMF (4mL) was added. The solution was heated to 80°C, and allowed to react for 2 hours. The reaction was quenched with water (10mL), and the crude product extracted with DCM (3x). The combined organic layers were dried, and the solvent removed under reduced pressure. The residue was purified by column chromatography (20:1 Hexanes:Ethyl Acetate) to give the product as a white solid (176mg, 35%).

*Synthesis of **(14)** – Pyrene-PEG*

Compound **(13)** (12mg, 0.035mmol) and mPEG-N_3-5kDa (264mg, 0.053mmol) were dissolved in 1mL of dichloromethane, and 1mL of water was subsequently added. Then Cu(0) – 1-2 pieces – was added, followed by $CuSO_4$ (2.2mg, 8.8μmol) and sodium ascorbate (3.49mg, 17.6μmol). The resulting mixture was allowed to react at room temperature overnight under vigorous stirring. The reaction mixture was diluted with dichloromethane and washed with water. The organic layer was then dried, and the solvent removed under reduced pressure. The crude product was purified by reversed phase chromatography, eluting with MeOH:DCM. Iodine vapor was used as a TLC developing agent. Removal of the solvent gave the product as a white solid (150mg, 80%).

5 Formation of High-Aspect Ratio Nanorods via Peptide-Driven Helical Self-Assembly of Fullerodendrimers

5.2 Introduction

The ability to self-assemble fullerene molecules into well-defined nanostructures is desirable for applications in polymer photovoltaics and organic electronics[61-64]. Fullerenes are excellent electron acceptors for utilization in organic photovoltaics[65], and have remained the electron-acceptor of choice since their usage in the first bulk-heterojunction photovoltaic, 18 years ago[66]. However, the ability to obtain high efficiency devices is highly dependent upon the morphology of the fullerenes molecules in the active layer[67, 68]. In the area of organic electronics, confined arrays of C_{60} fullerenes have been shown to possess highly delocalized electronic states[69, 70], and superconducting properties have been observed in intercalated C_{60} networks[71-73]. Therefore, C_{60}-based electronics and photovoltaics could greatly benefit from controllable assembly and patterning of fullerenes.

The self-assembly of pristine C_{60} has been accomplished through a number of methods[61] including liquid-liquid interfacial precipitation (LLIP), template-assisted drying, and drop drying. In addition to pristine C_{60}, functionalized fullerenes have been shown to form a variety of bilayer structures, depending upon solvent conditions[74]. However, the dimensions of these assemblies are on the order of several hundred nanometers to a few microns. In contrast, only a few instances of nanometer-scale, high-aspect ratio fullerene assembles have been reported, and these have relied on surface-based assembly methods[75-78], including Langmuir-Blodgett techniques[75], or HOPG-driven self-assembly[76, 77], thereby limiting their scalability.

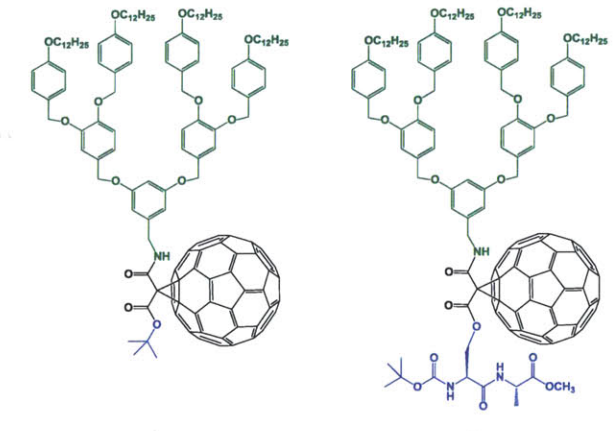

1 2

Figure 5.1 Molecular structures of the fullerodendrimers studied in this work.

Here, we report the synthesis of a novel pair of fullerodendrimers (Fig. 5.1) which self-assemble into one-dimensional fibers

in cyclohexane. We find that high-aspect ratio fullerene nanowires, with diameters of 3.76 ± 0.52nm, can be formed by utilizing peptide-driven self-assembly. These wires appear to consist of interwoven, helical assemblies of peptidic methanofullerenes.

5.3 Results and Discussion

In order to construct these molecules, second generation, benzyl dendrons of the form, [4-3,4-3,5]12G_2CH_2CN, were generally synthesized according to the scheme of Percec et. al.[82], with the only exception being the usage of 3,5-dihydroxybenzonitrile in the formation of the second apex, allowing for the introduction of an amine functionality at this terminus. Treatment of the cyano adduct with $LiAlH_4$ gave the aminated dendron [4-3,4-3,5]12$G_2CH_2NH_2$. Reaction of the aminated second generation dendron with mono-tert-butyl malonate via DCC/DMAP coupling yielded the dendritic precursor to **1**, which was then conjugated to C_{60} fullerene by Bingel addition[185]. For the formation of **2**, the aminated second generation dendron was coupled to methyl 3-chloro-3-oxopropionate, after which the methyl ester was cleaved under basic conditions[80], thereby allowing for the conjugation of the dipeptide sequence, Boc-L-Ser-L-Ala-OMe. This intermediate was coupled to C_{60} using Bingel conditions to yield fullerodendrimer **2**.

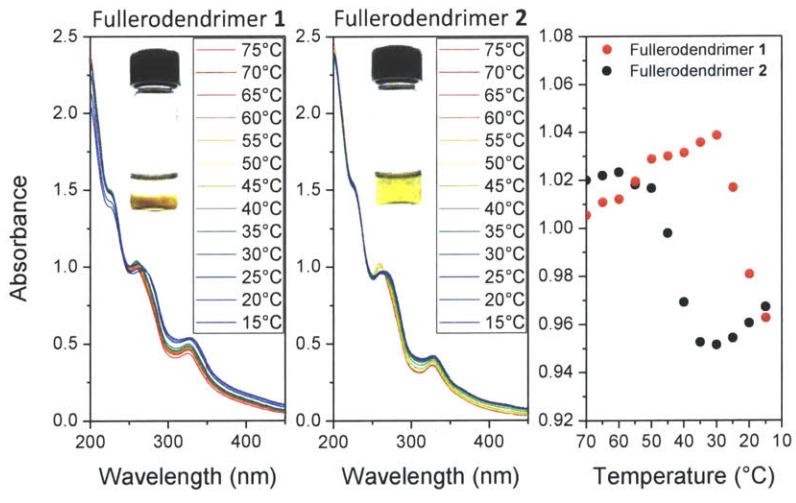

Figure 5.2 Temperature-dependent absorbance data for fullerodendrimers 1 (left) and 2 (middle) in cyclohexane at concentrations of 80μM. The rightmost figure follows the absorbance at 259nm as a function of temperature. Upon cooling from an isotropic state, the fullerene peak at 259nm decreases, with the evolution of a new peak near 267nm. The transition temperature occurs approximately 20°C higher in the case of fullerodendrimer 2.

While fullerodendrimers **1** and **2** are structurally similar, they display substantially different assembly behavior in the solution phase. This was first evidenced by their disparate behavior in variable-temperature absorbance measurements. Upon heating, both molecules could be dissolved in cyclohexane to yield homogeneous light-yellow to light-red solutions at 75-80°C. Figure 5.2 shows

temperature-dependent absorbance results for the two fullerodendrimers. Upon cooling, the fullerene absorbance feature at 259nm undergoes a decrease, while there is an increase in a red-shifted absorbance feature at approximately 267nm. The emergent feature is broader in the case of fullerodendrimer **1**, likely indicating a greater degree of inhomogeneity in the structure of the formed assemblies, which is in agreement with morphological results. In addition, the assembly transition of the two molecules occurs at different temperatures for the two species. As shown in Fig 5.2(c), assembly of the dipeptide derivative begins to occur near 50°C, while the onset of assembly for t-Butyl derivative does not occur until the sample has been cooled another 20°C. In addition, upon sitting for 24 hours, the resulting aggregates sediment out in the case of the t-Butyl derivative, while the dipeptide species remains dispersed (Figure 5.2). Together, these results indicate that there are differences in the assembled structures, formed by these two molecules, and that the dipeptide moiety plays an integral role in the assembly of fullerodendrimer **2.**

We hypothesize that the first step in the assembly process involves a wrapping of the fullerene moiety by the benzyl ether dendron, resulting in an initial, gradual increase in the absorbance feature at 259nm. In the absence of the dipeptide, these complexes are stable to 30°C, at which point non-specific aggregation occurs. In the presence of the dipeptide, the onset of intermolecular hydrogen bonding drives the assembly of the fullerodendrimer at a much higher temperature. Solution-phase assembly is further supported by variable temperature NMR experiments (Appendix B), which show a broadening and decrease in proton signal intensities, upon cooling, until the only observable signal is that attributable to the terminal, aliphatic chains of the dendron.

Differences in assembly behavior were further observed through morphological analysis of the suspensions. Figure 5.3(a) and 5.3(d) show SEM images of drop-dried solutions of the t-butyl and dipeptide derivatives, respectively. Here, it is evident that the dipeptide derivative forms high aspect ratio fibers, which pack into densely matted regions in the solid state. In contrast, the t-butyl derivative shows a less ordered assembly behavior, which prohibits the formation of dense regions. These results are confirmed by AFM (Fig. 5.3). Here, it is observed that the dipeptide derivative forms self-assembled wires with diameters of 3.76 ± 0.52nm, with lengths that can exceed 10μm. In contrast, the t-butyl derivative forms poorly-assembled fibers,

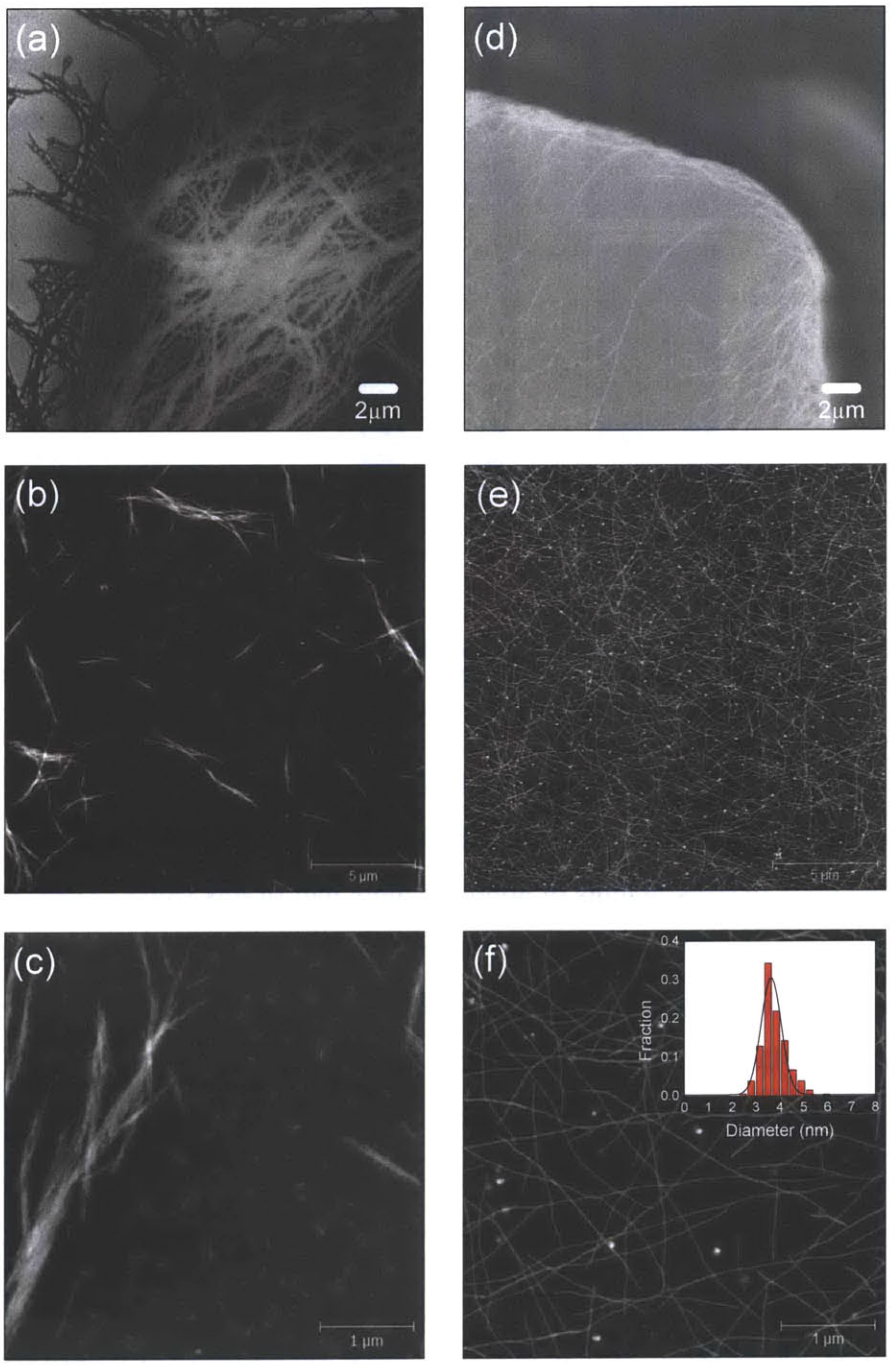

Figure 5.3 SEM (a),(d) and AFM (b),(c),(e),(f) images of self-assembled morphology. (d) SEM of a drop-cast solution of 1 shows the formation of densely matted regions of aligned fibers, while (a) SEM of a drop-cast solution of 2 shows randomly oriented domains. (e-f) AFM on spin-cast assemblies of 2 show structurally homogeneous fibers with average diameters of 3.76 ± 0.52nm, and lengths of a few hundred nanometers to > 10μm. (b-c) AFM on spin-cast assemblies of 1 show the formation of aggregated fibrils, rather than well-formed wires.

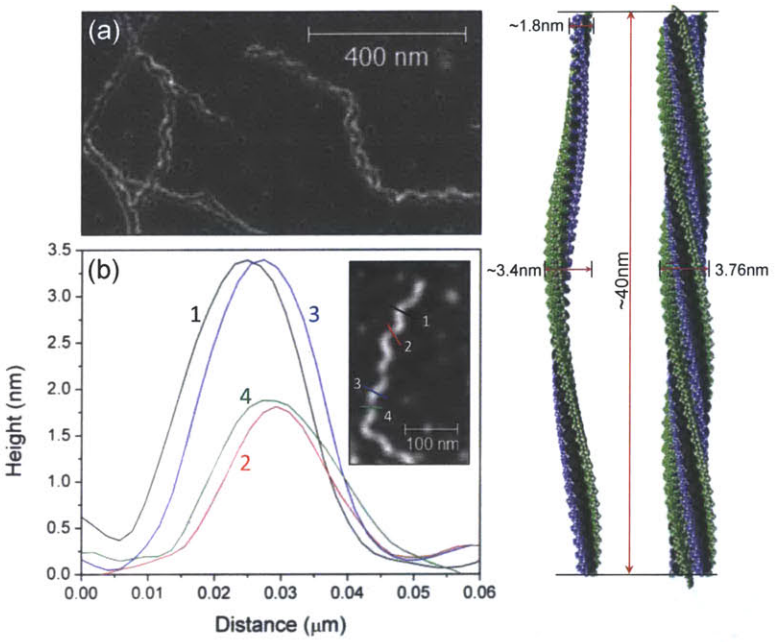

Figure 5.4 AFM (a) phase image, and (b) height profiles obtained from helical assemblies of fullerodendrimer (2). The inset of (b) shows a height image of an isolated, helical fiber, along with the positions at which height traces were evaluated.

which further aggregate into larger fibrils. Interestingly, the morphology of these nanowires changes over time. Upon standing for several weeks, AFM reveals that the initial, straight fullerene wires transform into a combination of straight wires and helical assemblies, with clear junctions between the two types of structures. AFM phase and height images of these helical assemblies are presented in Figure 5.4. As can be seen from the height traces in Figure 5.4(b), the peaks of these helices occur at heights close to 3.5nm, which is consistent with the diameter distribution of the initial fullerene wires. In contrast, the valleys along the helix possess heights of approximately half of this value. These results seem to indicate that the initially formed fullerene wires consist of multiple, interwoven strands of fullerodendrimer **1**, which unravel over time. This hypothesis is further supported by phase images of in-tact fullerene nanorods, which show helical striations along the length of the fiber (Fig. 5.5). From AFM images, the helical pitch of these fibers appears to be approximately 40 ± 4nm.

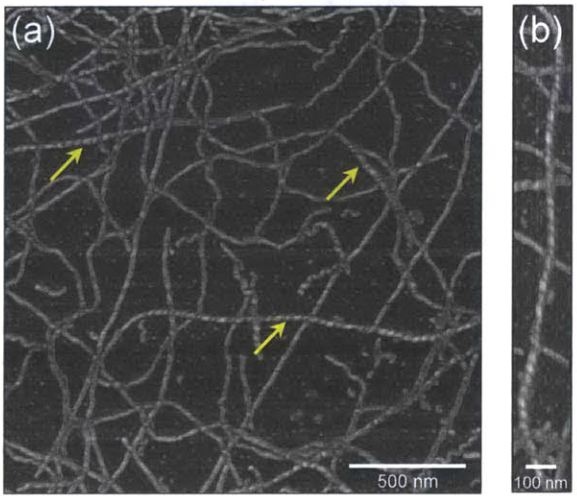

Figure 5.5 AFM phase images of assembled fullerodendrimer (2) showing helical striations along the length of the assembled nanorods. (b) Zoomed-in phase image of one of these assemblies.

The direct observation of helicity in these structures led us to question whether a racemic mixture of left and right-handed assemblies are formed, or if the chirality of the peptide drives the selective formation of a particular supramolecular structure. To

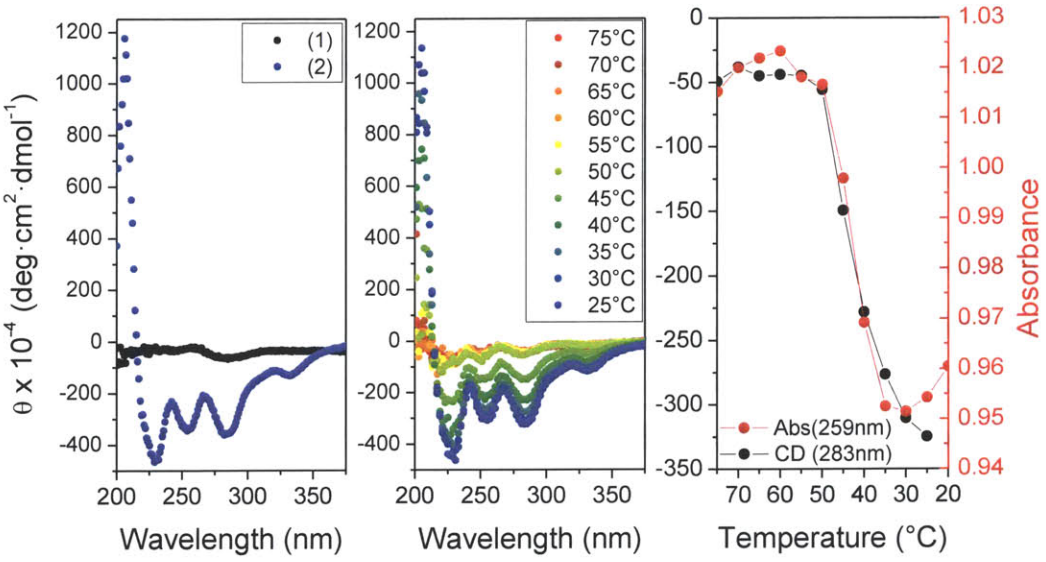

Figure 5.6 Left: Room-temperature CD spectra of fullerodendrimers 1 and 2. Fullerodendrimer 1, which lacks the dipeptide sequence, shows no significant CD features, whereas fullerodendrimer 2 shows clear spectral features, indicating selectivity toward a particular handedness during self-assembly. Middle: temperature-dependent CD spectra of fullerodendrimer 2. CD features emerge upon cooling from an isotropic state, indicating that these features emerge during the self-assembly of the nanorods, and are not intrinsic to the molecule, itself. Right: comparison between temperature dependent absorbance (259nm) and the temperature dependent CD signal at 283nm.

examine this, we conducted circular dichroism (CD) measurements on the two fullerodendrimers.

The results of CD measurements are shown in Figure 5.6. The figure on the left shows room-temperature CD spectra for both fullerodendrimers **1** and **2**. From these spectra, two properties of the assembly can be deduced. The first is that the self-assembly of fullerodendrimer **2** favors a particular handedness of helical arrangement. In combination with AFM results, it appears that left-handed helices are selectively formed in this system. In addition, the lack of CD features in the case of fullerodendrimer **1** indicates that the dipeptide molecule plays an integral role in the handedness of the resulting nanorod. In addition to room temperature measurements, variable temperature CD spectra were acquired for fullerodendrimer **2** (fig. 5.6-middle). From variable-temperature measurements, it is clear that, upon heating the assembled molecules to an isotropic state, no significant CD features are observed. However, these features reappear upon cooling of the sample to room temperature. These results indicate that it is not the chirality of the molecule, itself, that imparts the CD signal, but the handedness of the supramolecular assembly. On the right of Figure 5.6, we plot the change in CD signal at 289nm as a function of temperature, and overlay the response with that observed during variable-

temperature absorbance measurements. From the plot, it is evident that there is very good agreement between these two experimental measurements. This result indicates that the onset of self-assembly, near 50°C, is driven by the dipeptide sequence, which simultaneously imparts chirality to the resulting supramolecular assembly.

5.4 Conclusions

In conclusion, we have synthesized two novel, asymmetric fullerodendrimers, and have analyzed their self-assembly behavior. Through the introduction of a dipeptide sequence to one terminus of the dendritic methanofullerene, we show that it is possible to change the self-assembly behavior from the formation of poorly-ordered aggregates to high aspect ratio nanorods. The formation of these nanorods is driven by interactions between the dipeptide moieties, and this interaction simultaneously imparts helicity to the resulting supramolecular structure. The resulting nanorods appear to be comprised of interwoven helices of dendritic methanofullerenes.

5.5 Synthesis

The synthesis of the fullerodendrimers employed in this work was generally carried out according to Scheme 5-1. Specific synthetic details are provide, below.

[4-3,4-3,5]12G$_2$CN (2): [4-3,4]12G$_1$CH$_2$Cl (**1**) was synthesized according to the method of Percec et al[82]. To a degassed suspension of K_2CO_3 (5.02g, 36mmol) in anhydrous DMF (35mL) was added 3,5-dihydroxybenzonitrile (1.23g, 9mmol). The mixture was heated to 70°C, and [4-3,4]12G$_1$CH$_2$Cl (13.48g, 19mmol) was added while stirring. The atmosphere was replaced with nitrogen, and the reaction was allowed to react at 70°C for 8 hours. Completion of the reaction was monitored by TLC (7:1 Hexanes:EtOAc). The reaction mixture was cooled to r.t. and precipitated into cold water. The resulting solid was collected by suction filtration and

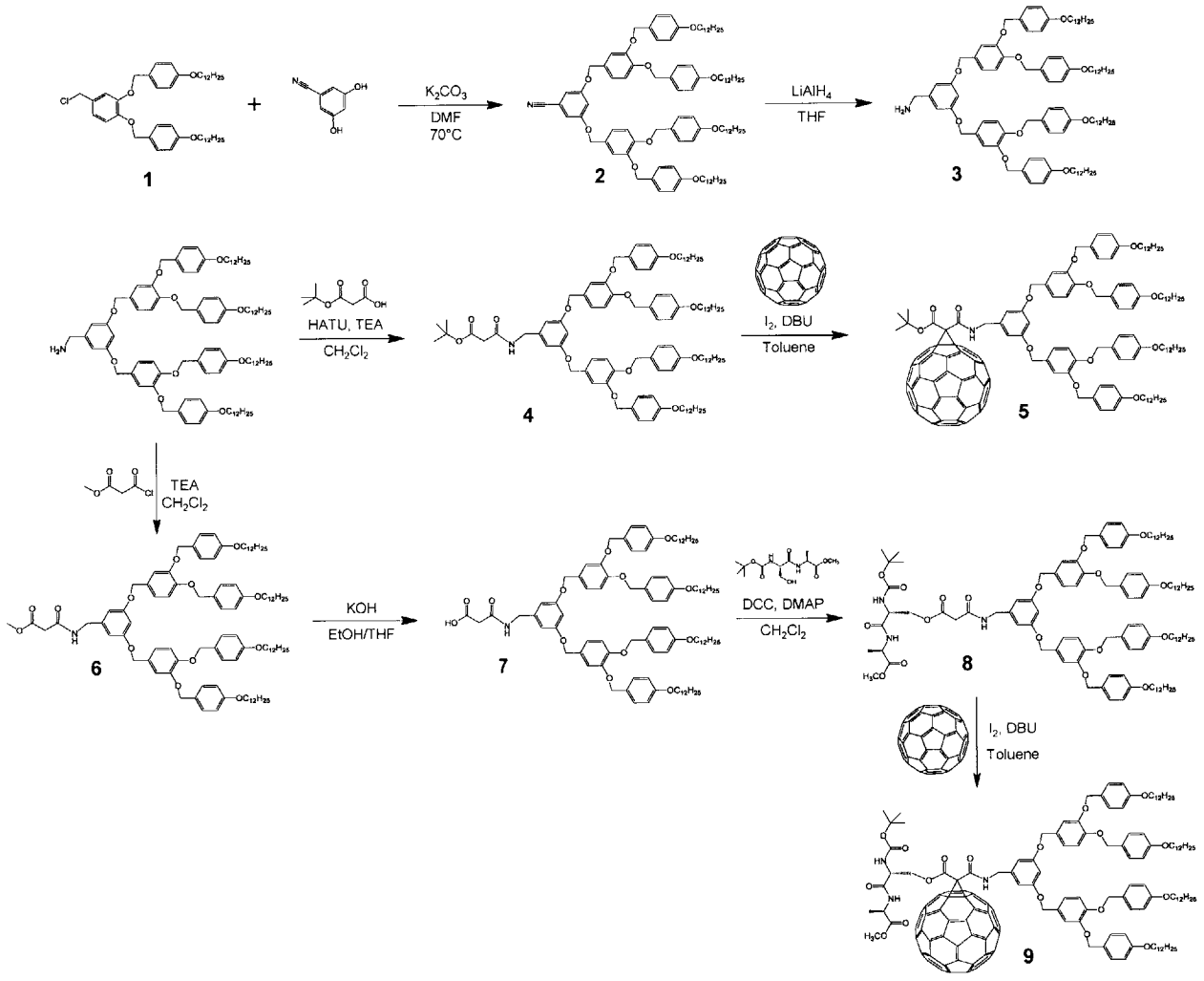

Scheme 5-1 Synthesis of fullerodendrimers.

purified by column chromatography (silica gel/CH_2Cl_2) followed by recrystallization from acetone to yield the product (12.9g, 96%) as a white solid.

[4-3,4-3,5]12G$_2$CH$_2$NH$_2$ (3): To a cooled (0°C), stirred slurry of $LiAlH_4$ (0.15g, 4mmol) in anhydrous THF (5mL) was slowly added a solution of [4-3,4-3,5]12G$_2$CN (2g, 1.3mmol) in anhydrous THF (4mL). After complete addition, the mixture was allowed to warm to r.t. and stirred an additional hour. Reaction progress was monitored by TLC (CH_2Cl_2). After completion, the mixture was again cooled to 0°C, and the reaction was carefully quenched by sequential additions of water (0.15mL), 15% NaOH (0.15mL), and water (0.46mL). This mixture was allowed to stir until H_2 evolution ceased, and then filtered to remove lithium salts, which were extensively rinsed with CH_2Cl_2. The filtrate was dried, and the solvent removed to give the crude product, which was purified by column chromatography (silica gel, 20:1 CH_2Cl_2:MeOH) to give the product as a white solid (1.76g, 87.6%).

[4-3,4-3,5]12G$_2$CH$_2$NH-COCH$_2$CO-OC(CH$_3$)$_3$ (4): [4-3,4-3,5]12G$_2$CH$_2$NH$_2$ (5g, 3.38mmol) and mono-*tert*-butyl malonate (0.433mL, 2.82mmol) were dissolved in deoxygenated, anhydrous DCM (120mL). Triethylamine (0.588mL, 4.22mmol) and HATU (1.28g, 3.38mmol) were then added, and the reaction was allowed to proceed overnight under a nitrogen atmosphere. The resulting solution was transferred to a separatory funnel, washed with 10% citric acid and saturated sodium bicarbonate, and then dried, and concentrated under reduced pressure. Purification by silica gel chromatography (4:1 Hexanes:EtOAc) gave the product as a white solid (1.58g, 29%).

Methanofullerene (5): Dendritic malonate **4** (0.50g, 0.308mmol) and C_{60} (0.44g, 0.616mmol) were dissolved in anhydrous toluene (150mL), and the solution bubbled with nitrogen. After surrounding the reaction vessel with foil to exclude ambient light, iodine (86mg, 0.339mmol) was added. Under N_2, 1,8-diazabicyclo[5.4.0]undec-7-ene (DBU) (60μL, 0.401mmol) in anhydrous toluene (100mL) was then added dropwise over 1 hour. The resulting solution was allowed to react for 24 hours at r.t., after which the reaction solution was concentrated under reduced pressure, and purified by silica gel chromatography, first eluting unreacted C_{60} with toluene, and subsequently eluting the mono-adduct with DCM. The resulting solid was redissolved in a minimal amount of DCM, precipitated into MeOH, and collected by suction

filtration using a 0.45μm Teflon membrane to yield the product as a brown solid (177mg, 25%). MALDI-TOF for $C_{164}H_{149}NO_{13}$ *m/z* cald: 2364.8 $[M+Na]^+$; found: 2364.1.

[4-3,4-3,5]12G$_2$CH$_2$NH-COCH$_2$CO-OCH$_3$ (6): [4-3,4-3,5]12G$_2$CH$_2$NH$_2$ (276mg, 0.186mmol) was dissolved in anhydrous dichloromethane, and triethylamine (31.2uL, 0.224mmol) was added. The atmosphere was replaced with nitrogen, and the solution was cooled in an ice bath. Methyl 3-chloro-3-oxopropionate (20uL, 0.186mmol) was added at 0°C. The solution as stirred at 0°C for 30 minutes, warmed to r.t., and allowed to react an additional 24 hours. The reaction solution was diluted with DCM and transferred to a separatory funnel. The organic phase was washed with saturated sodium bicarbonate solution, brine, dried and the solvent removed by rotovap. The resulting solid was purified by column chromatography (~0.5% MeOH in DCM) to give the product as a white to off-white solid (184mg, 63.4%).

[4-3,4-3,5]12G$_2$CH$_2$NH-COCH$_2$COOH (7): Cleavage of the methoxy group was procedure adapted from reference [80]. To a round-bottom flask was added malonate derivative **6** (0.4g, 0.246mmol), potassium hydroxide (97mg, 1.73mmol), THF (8.1mL), and 95% ethanol (3.5mL). The mixture was heated to reflux, and monitored for completion by TLC (3-4 hours). The mixture was cooled to r.t., neutralized with 50% aqueous acetic acid, and the precipitate collected using a 0.45μm PVDF membrane to yield the product as a white solid (337mg, 87.3% yield).

[4-3,4-3,5]12G$_2$CH$_2$NH-COCH$_2$CO-Boc-L-Ser-L-Ala-OMe (8): Boc-L-Ser-L-Ala-OMe was synthesized using the protocol of Alam et al.[186]. For the synthesis of **8**, malonic acid derivative **7** (337mg, 0.215mmol), Boc-L-Ser-L-Ala-OMe (125mg, 0.43mmol), and DMAP (5.5mg, 0.045mmol) were dissolved in a minimal amount of anhydrous DCM, and the resulting solution cooled in an ice bath. The ambient atmosphere was replaced with N_2, and a solution of DCC (53mg, 0.258mmol) in DCM was added dropwise. The solution was allowed to react at 0°C for 2 hours, allowed to warm to r.t., and reacted overnight. Insoluble dicyclohexylurea was removed by filtration. The solution was concentrated under reduced pressure and then purified by silica gel chromatography eluting on a gradient from 0.5-1.0% MeOH in DCM, giving the product as a white solid (214mg, 54%). Dicyclohexylurea was difficult to completely remove by chromatography, and DIC was a better coupling reagent for this reaction. However, residual dicyclohexylurea did not interfere with the subsequent coupling to C_{60}.

Peptidic Methanofullerene (9): Dendritic dipeptide **8** (0.21g, 0.114mmol) and C_{60} (0.126g, 0.175mmol) were dissolved in anhydrous toluene (42mL), and the solution bubbled with nitrogen. After surrounding the reaction vessel with foil to exclude ambient light, iodine (32mg, 0.126mmol) was added. Under N_2, 1,8-diazabicyclo[5.4.0]undec-7-ene (DBU) (23μL, 0.151mmol) in anhydrous toluene (10.5mL) was then added dropwise over 1 hour. The resulting solution was allowed to react for 24 hours at r.t., after which the reaction solution was concentrated under reduced pressure, and purified by silica gel chromatography, first eluting unreacted C_{60} with toluene, and subsequently eluting the mono-adduct with 100:3 toluene:acetone. The resulting solid was redissolved in a minimal amount of DCM, precipitated into MeOH, and collected by suction filtration using a 0.45μm Teflon membrane to yield the product as a brown solid (127mg, 43%). MALDI-TOF for $C_{172}H_{163}N_3O_{18}$ *m/z* cald: 2581.0 $[M+Na]^+$; found: 2580.4.

6 Conclusions and Outlook

The central objective of my thesis was to engineer and analyze interfaces for electron transfer in nanocarbon systems. In Chapters 2 and 3 of this thesis, I examined ground-state electron transfer, from SWCNTs to aryl diazonium salts, in the diazonium derivatization of carbon nanotubes. There, it was found that, due to heterogeneous chiral populations of SWCNT in solution, it not feasible to stoichiometrically control the extent of covalent functionalization in the low conversion limit.

I then sought to examine whether adsorbed surfactants could be utilized to impart an additional degree of control over SWCNT reactivity. There, it was shown that the surfactant can influence the reactions of carbon nanotubes in a variety of ways, including electrostatics, steric exclusion, and direct chemical modification of the reacting species. Therefore, surfactants represent promising candidates for modulating the reactivity of carbon nanotubes. However, thus far, only ensemble measurements have been performed, and there is little information on the number and spatial distribution of defect sites. Therefore, future directions for this work should focus on tagging and quantifying covalent defect sites. Such a study could potentially lead to the demonstration of surfactant-induced, site-directed functionalization of carbon nanotubes. For example, in the case of gold nanorods, electrostatic effects, driven by cationic surfactants, have been proposed to be responsible for preferential end growth[187]. In those systems, curvature effects at the nanorod ends decrease the electrostatic barrier for ion penetration, resulting in preferential axial growth. Analogously, in the case of carbon nanotubes, it may be possible to utilize cationic surfactants to direct diazonium functionalization to the termini of the carbon nanotube. In Chapter 3, it was already demonstrated that the barrier to reactivity in cationic systems is high, and especially in the case of large diameter nanotubes, the reaction kinetics associated with derivatization of the nanotube sidewall are very slow. This may provide a window of opportunity for selective end functionalization to occur. However, better labeling and characterization techniques are required in order to evaluate statistical distributions of diazonium induced defects along the SWCNT length.

Additionally, in the case of the bile salt surfactants, reactivity is controlled by the steric exclusion of the diazonium ion from the SWCNT surface. In these systems, it is possible that existing defect sites along the SWCNT length could disrupt the surfactant packing near that

location, resulting in preferential functionalization in the vicinity of existing defects. Experimentally, in the case of completely random functionalization of the nanotube sidewall, one would expect that it would be possible to obtain high degrees of fluorescence quenching (due to the delocalization of the exciton) without significantly changing the absorbance spectrum. This type of behavior is observed in figs 3.2(a) and 3.2(b) for the SDS surfactant. In contrast, if functionalization propagates from existing defects sites, one would expect to see concurrent modulation of both absorbance and fluorescence. Indeed, this type of behavior appears to be observed for the sodium cholate system in figs 3.4(a) and 3.5(a). In addition, the Raman spectra for this system shows an initial, sharp increase in D/G ratio, followed by a slower increase with added diazonium thereafter. Such behavior is consistent with previous observations of defect-site propagation along carbon nanotubes[188]. However, further characterization needs to be performed in order to validate such a mechanism.

In Chapter 4, we developed Marcus theory-based structure-reactivity relationships for excited-state electron transfer from semiconducting SWCNTs to a series of methanofullerenes. There, it was shown that, due to the small energetic driving force for electron transfer in the cases of C_{61} and C_{71}, only partial fluorescence quenching is observed across all species. In contrast, even at low surface coverages of C_{85}, SWCNT fluorescence is quenched across all species that were analyzed in this work. This is likely due to the deeper LUMO level of the C_{85} methanofullerene, which results in energy offsets that exceed the exciton binding energy in SWCNT. This result, combined with the fact that C_{85} has much higher photo-stability than C_{61} and C_{71}, makes this larger fullerene adduct a promising candidate for SWCNT-based sensors and photovoltaics.

For SWCNT fluorescence-based sensor applications, the ability to describe the these systems using Marcus theory informs us that the rate constant associated with electron transfer should decay exponentially with the distance from the SWCNT surface. Therefore, a small displacement of the fullerene, such as that which could result from a protein binding event, could cause a substantial modulation of SWCNT fluorescence. This characteristic could make these SWCNT-C_{85} heterojunctions useful candidates for applications in label-free protein detection.

For photovoltaic devices, experimental results appear to indicate that the energetics for electron transfer from photo-excited SWCNTs to C_{85} is highly favorable. However, the direct

usage of this fullerene derivative in SWCNT-based photovoltaics is hindered by the fact that C_{84} exists as multiple isomers, the presence of which could reduce device performance. Therefore, the utilization of this fullerene in SWCNT-based photovoltaics will benefit from advances in isomer separation of fullerenes.

Finally, in Chapter 5, we demonstrated that, through the introduction of a dipeptide sequence to one terminus of a C_{61} fullerodendrimer, it is possible to change the self-assembly behavior from the formation of poorly-ordered aggregates to high aspect ratio nanorods. The formation of these nanorods is driven by interactions between the dipeptide moieties, and this interaction simultaneously imparts helicity to the resulting supramolecular structure.

If there is substantial inter-fullerene interaction in these systems, it is possible that these self-assembled fibers could find use in molecular electronics and organic photovoltaics. In particular, the large band-gap of fullerenes could enable applications in molecular field-effect transistors. In addition, fullerenes are excellent electron acceptors for use in organic photovoltaics, and the ability to self-assemble fullerenes in a controlled manner could improve device efficiencies by aiding in the control of active layer morphology.

7 Appendix A: Molecular Characterization of Water-Soluble Fullerene Derivatives

7.2 Excess Surfactant Removal by Centrifugal Filtration

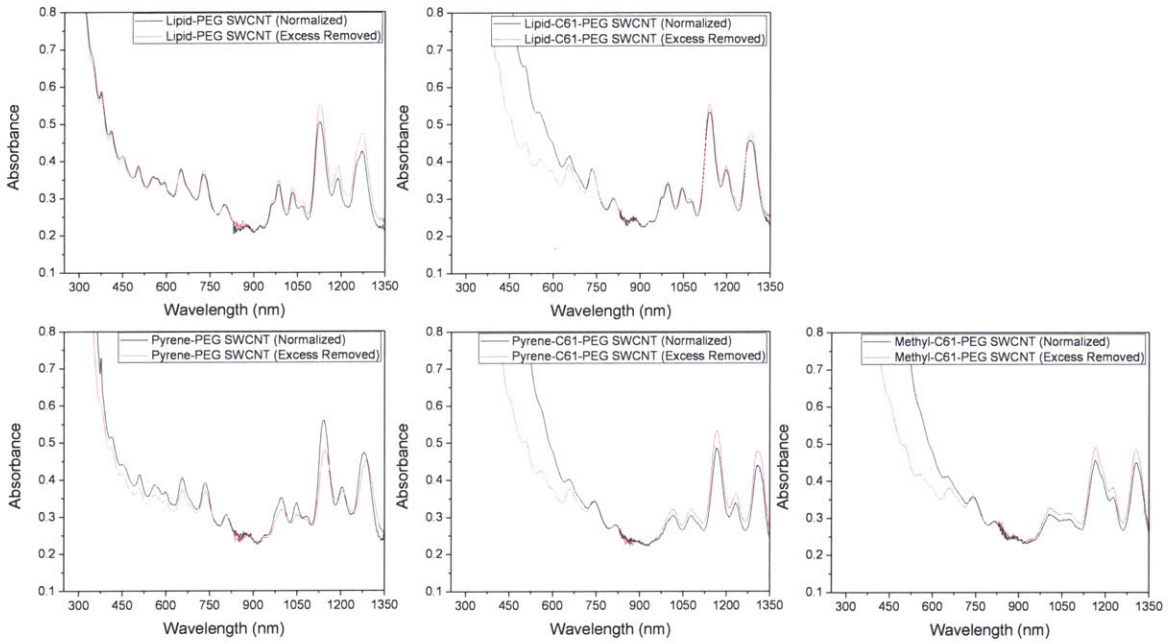

Figure 7.1 Absorbance spectra of SWCNT suspensions in amphiphiles (4), (7), (10), (12), and (14) – from Schemes 4-1 and 4-2 – before (black) and after (red) removal of free amphiphile. In order to account for slight concentration differences, absorbance spectra have been adjusted by a constant such that their absorbance values near 900nm are similar. Despite small redistributions in chirality, most spectra taken before and after removal are fairly consistent. However, the pyrene-PEG sample shows evident decrease in peak-to-valley ratio, as well as slight peak shifting, indicating that aggregation is occurring. Visible aggregates were also observable the pyrene-PEG system after the removal of excess surfactant.

7.3 MALDI-TOF

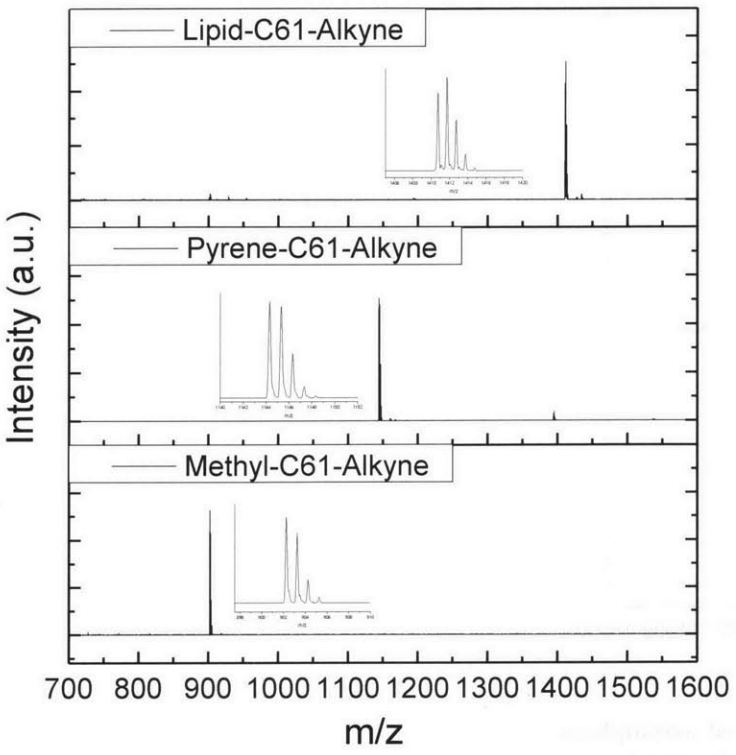

Figure 7.2 MALDI-TOF for the three methanofullerene intermediates, (3), (6), and (9) from Scheme 4-1.

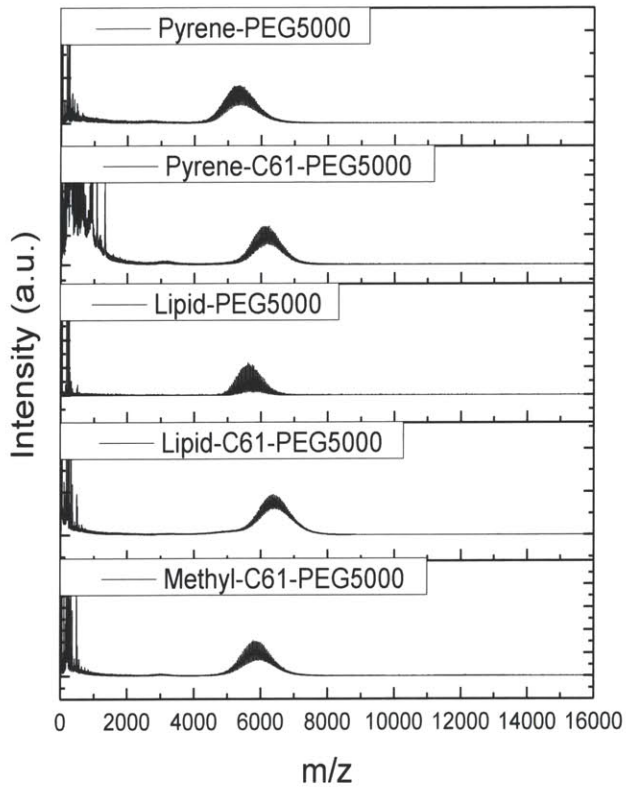

Figure 7.3 MALDI-TOF on the PEGylated amphiphiles (4), (7), (10), (12) and (14) from Schemes 4-1 and 4-2.

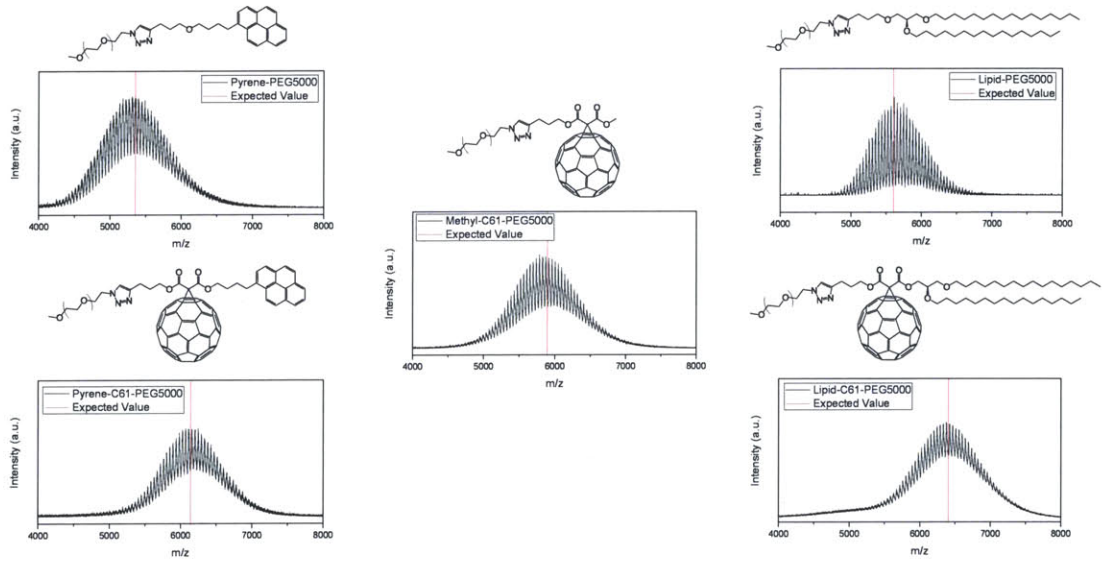

Figure 7.4 Zoomed-in MALDI-TOF on the PEGylated amphiphiles (4), (7), (10), (12) and (14), from Schemes 4-1 and 4-2, along with expected values.

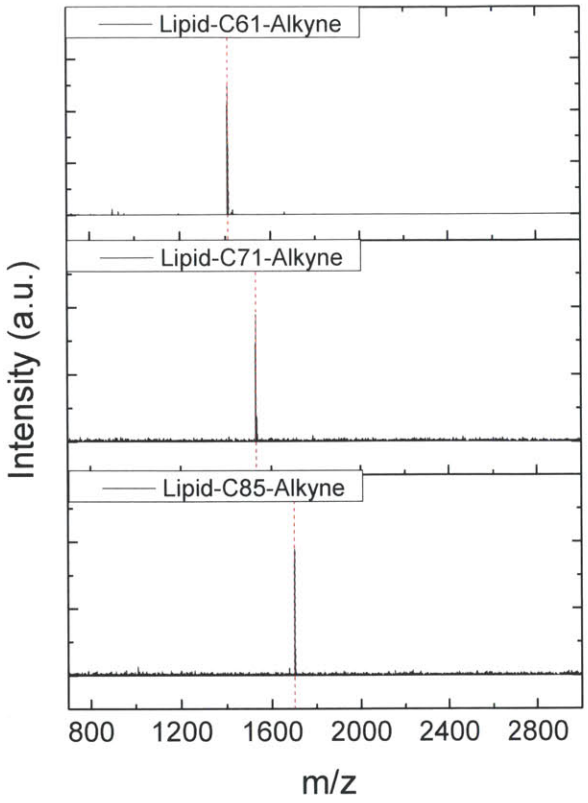

Figure 7.5 MALDI-TOF comparing the three methanofullerenes intermediates used for the fullerene family analysis.

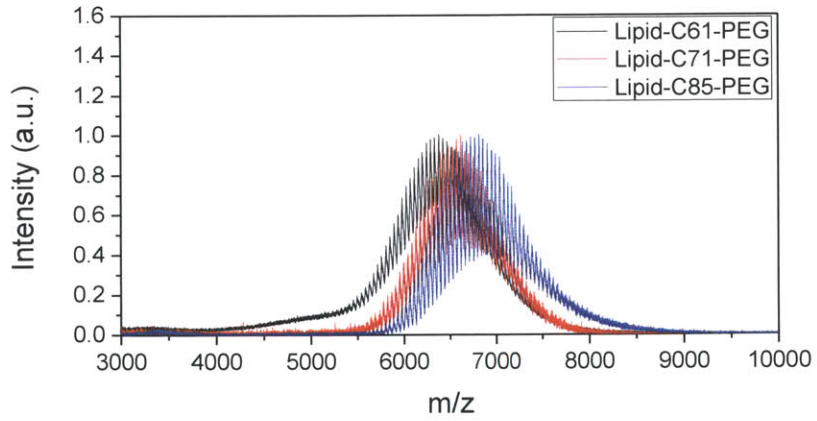

Figure 7.6 MALDI-TOF comparing the three PEGylated methanofullerenes used for the fullerene family analysis.

7.4 AFM

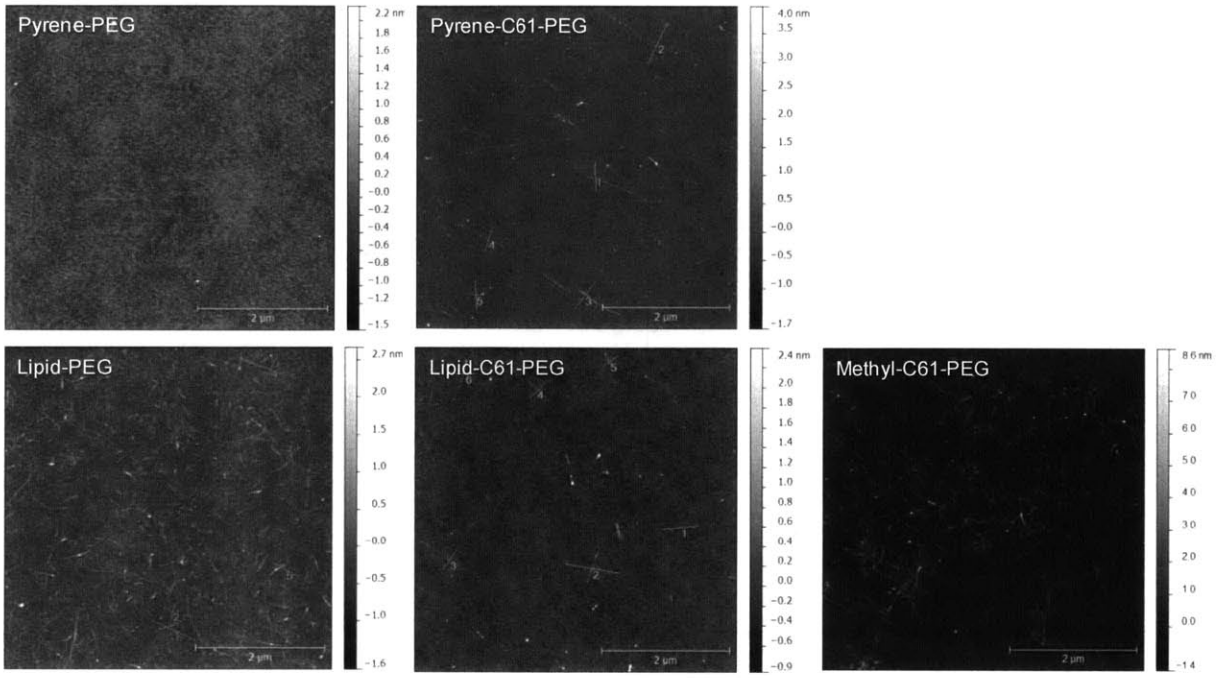

Figure 7.7 AFM images showing individually dispersed nanotubes in the cases of pyrene-PEG, pyrene-C61-PEG, lipid-PEG, and lipid-C61-PEG. SWCNT suspensions using methyl-C61-PEG displayed bundles of nanotubes.

7.5 NMR

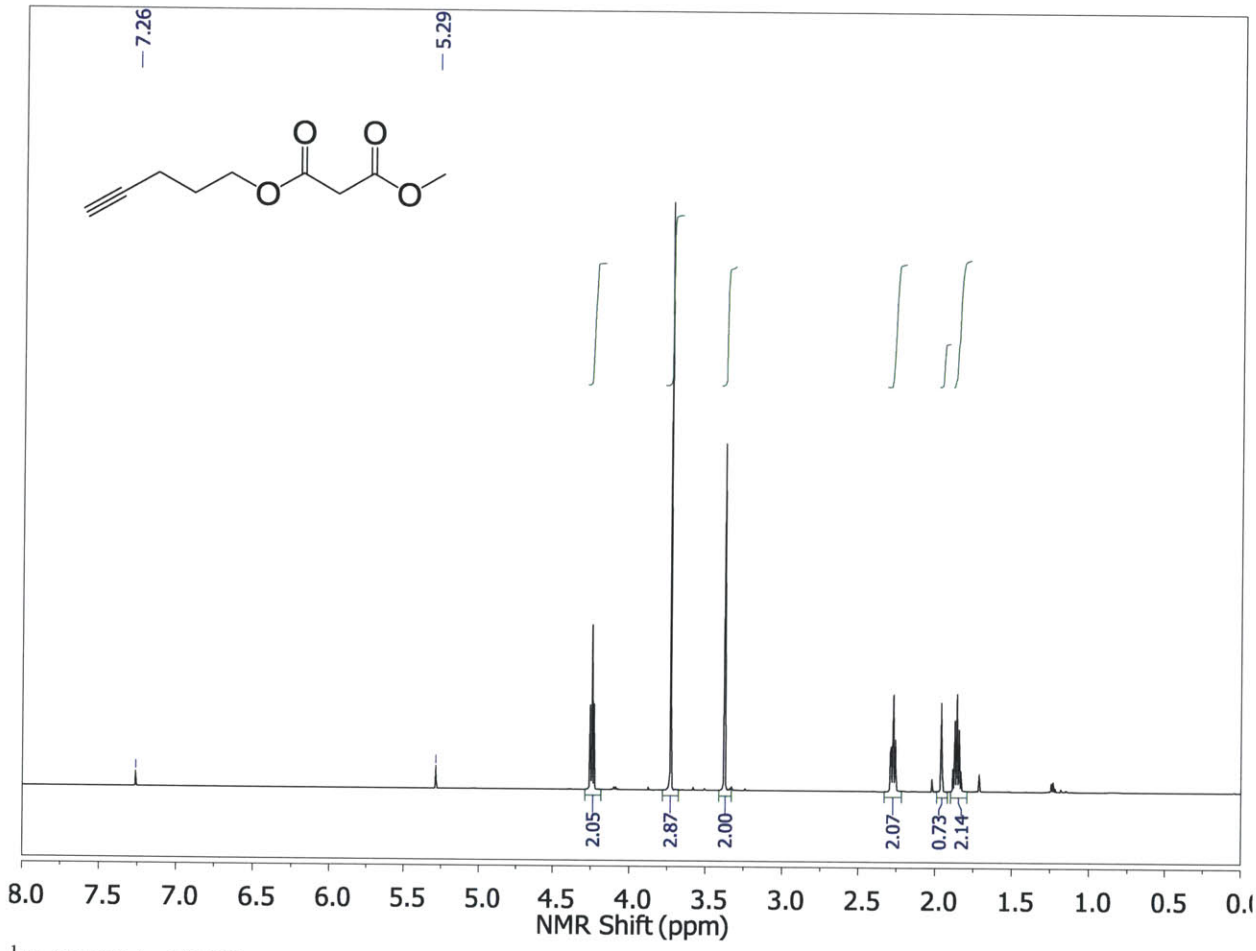

^{1}H-NMR in $CDCl_3$

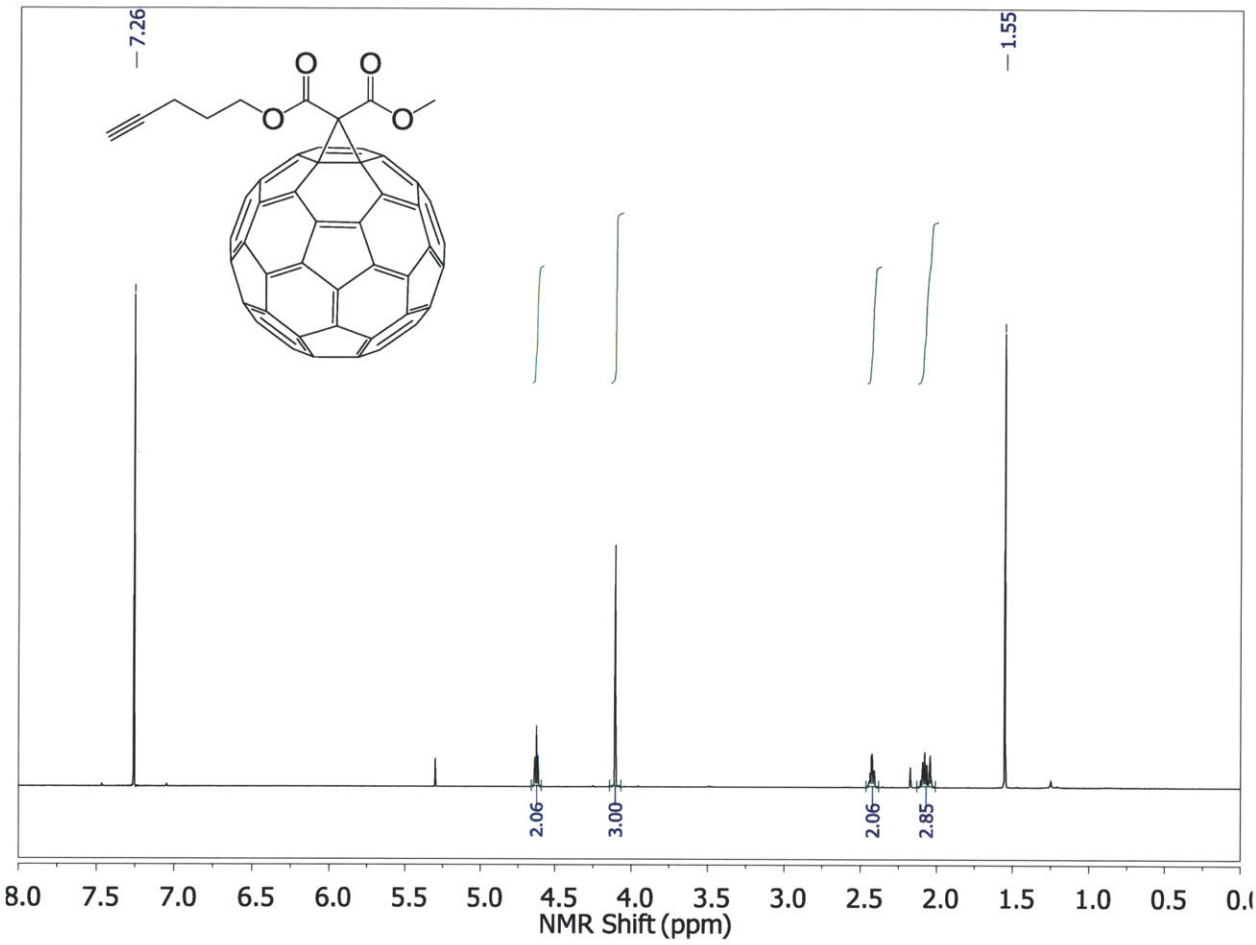

^{1}H-NMR in $CDCl_3$

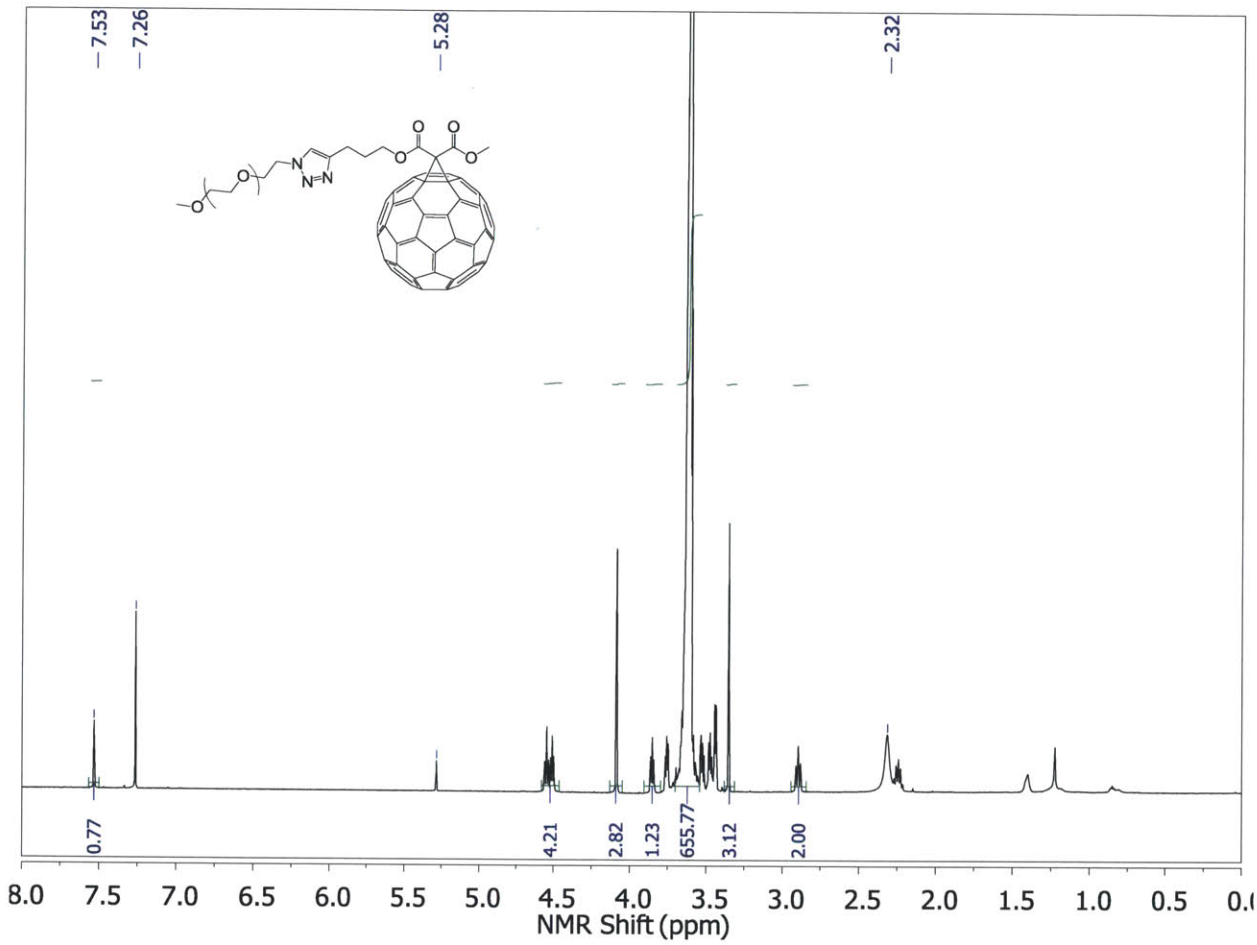

^{1}H-NMR in $CDCl_3$

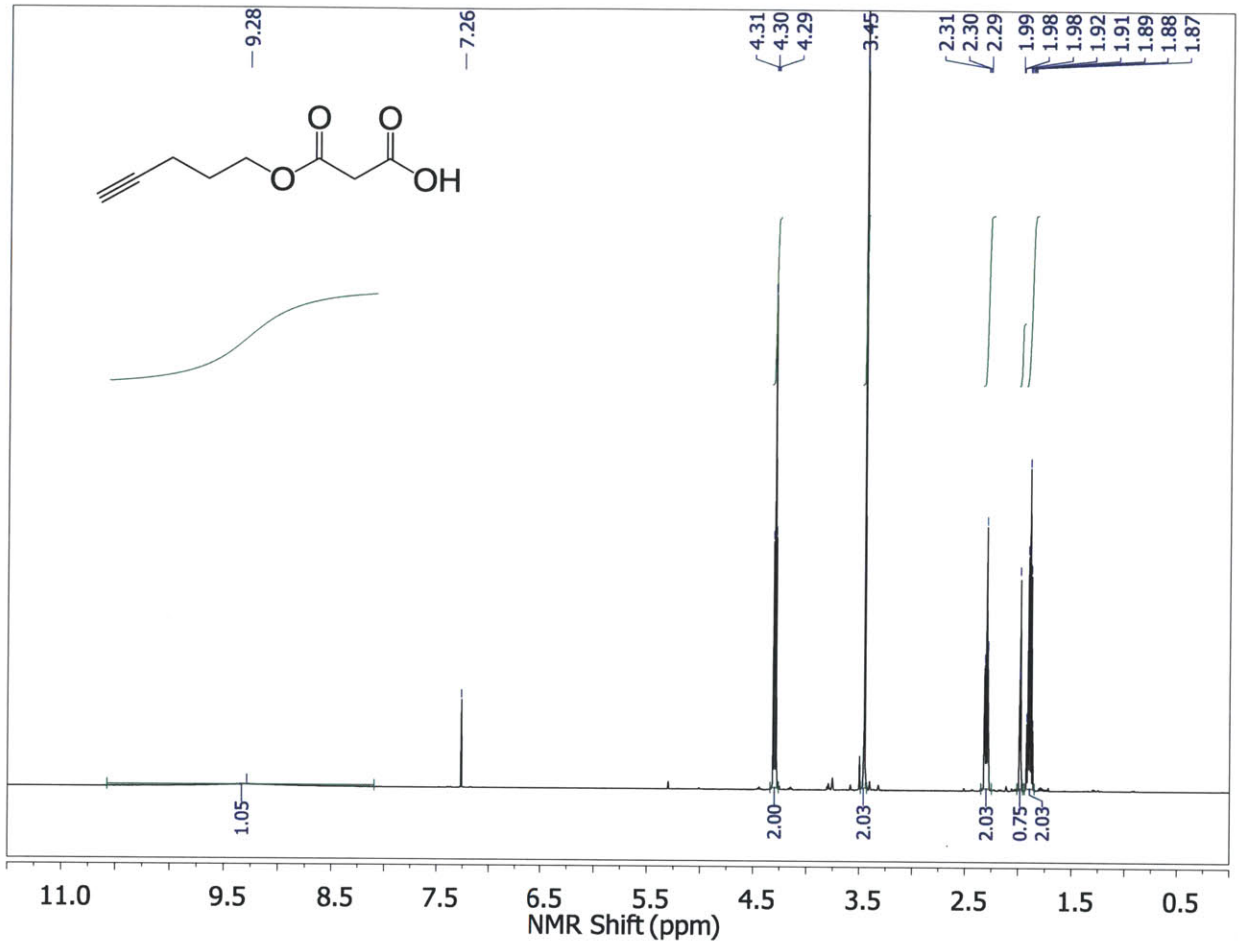

^{1}H-NMR in $CDCl_3$

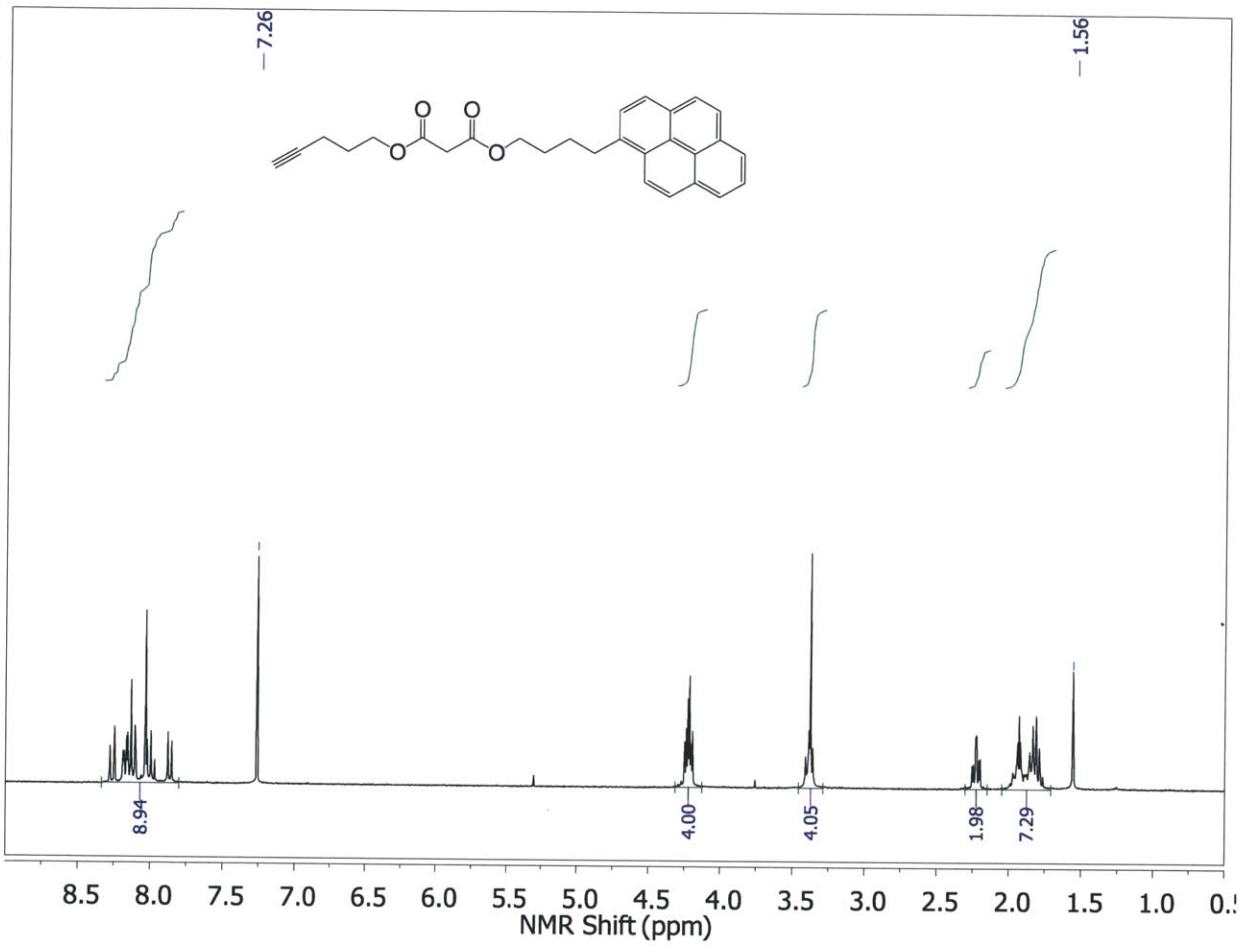

^{1}H-NMR in $CDCl_3$

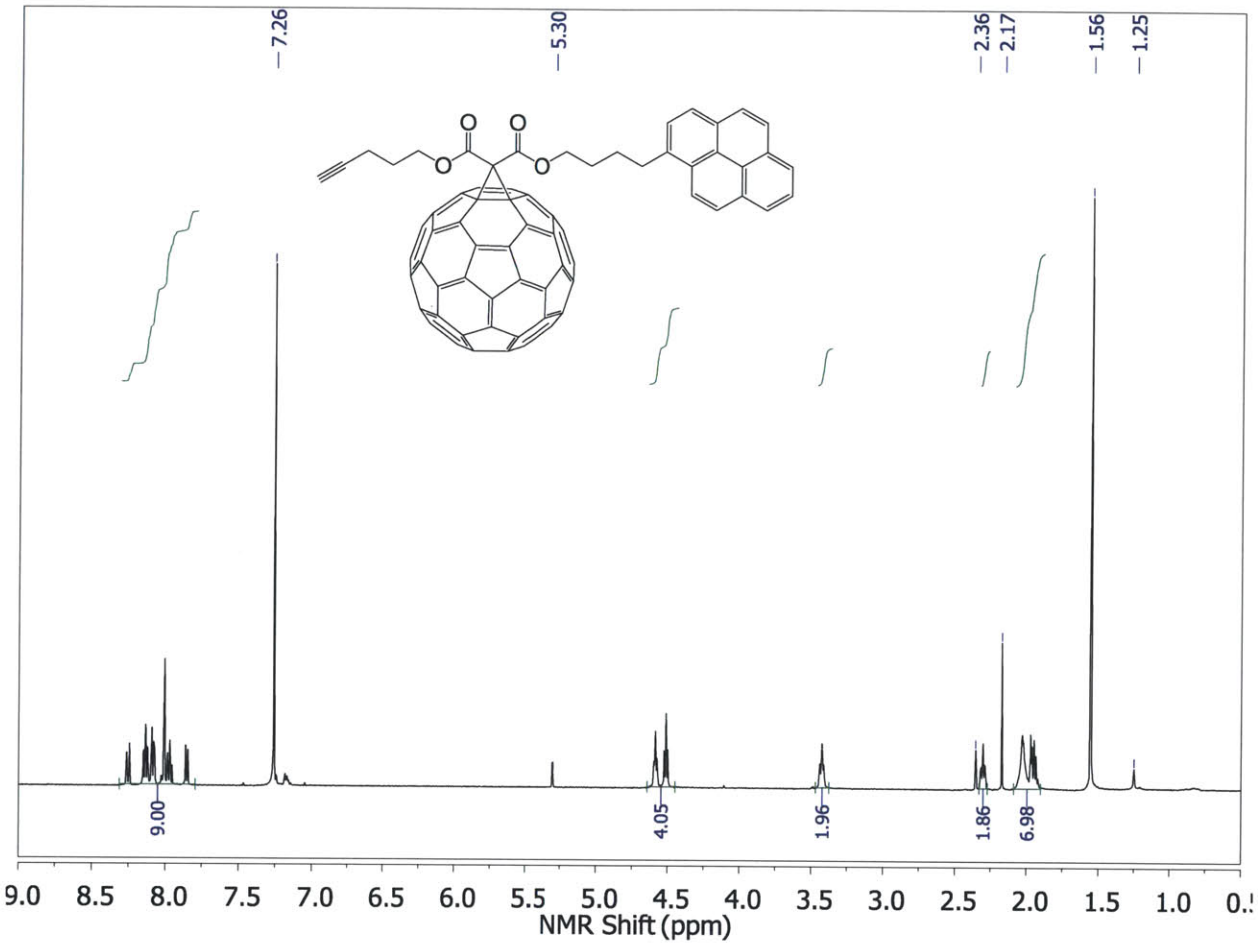

^{1}H-NMR in $CDCl_3$

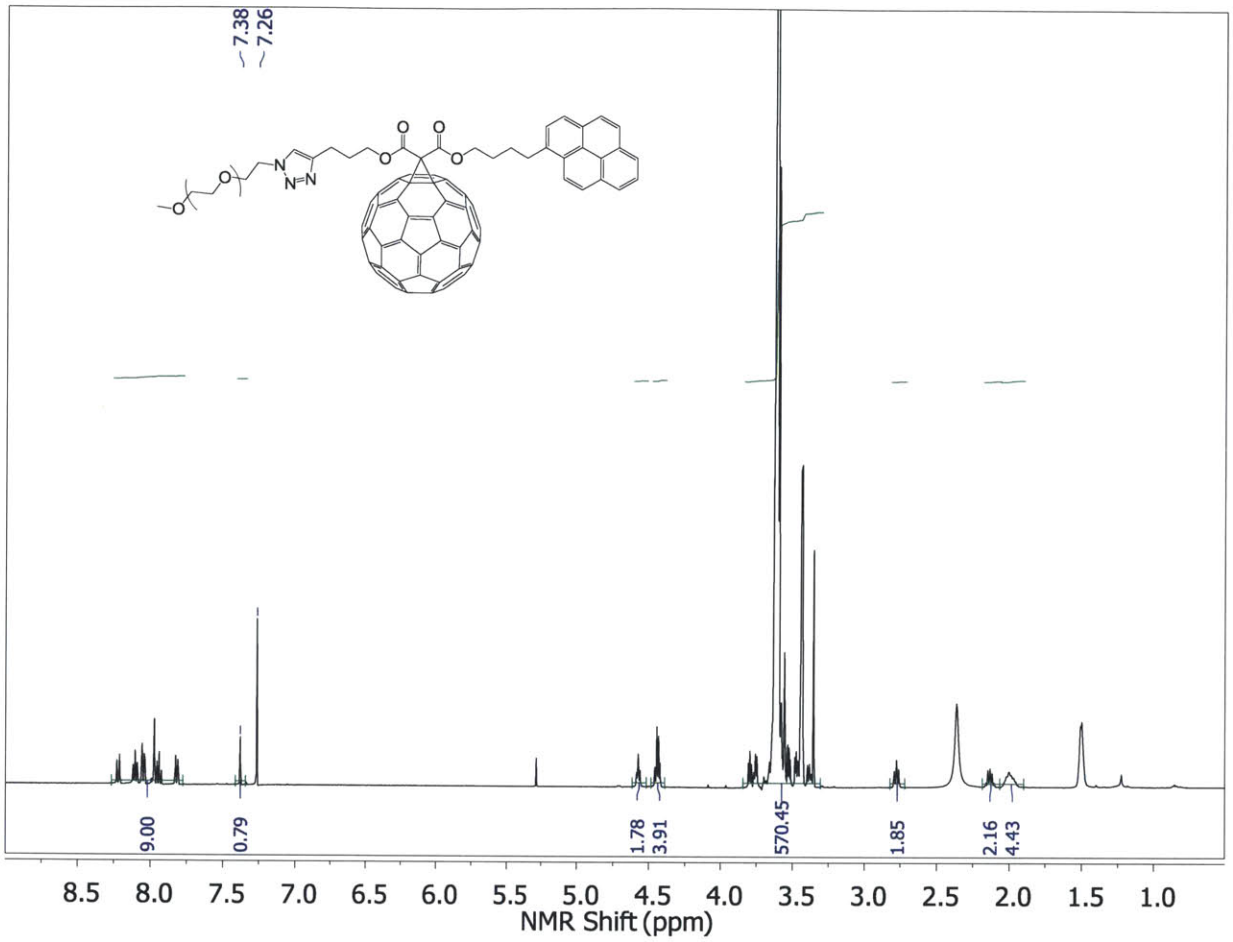

^{1}H-NMR in $CDCl_3$

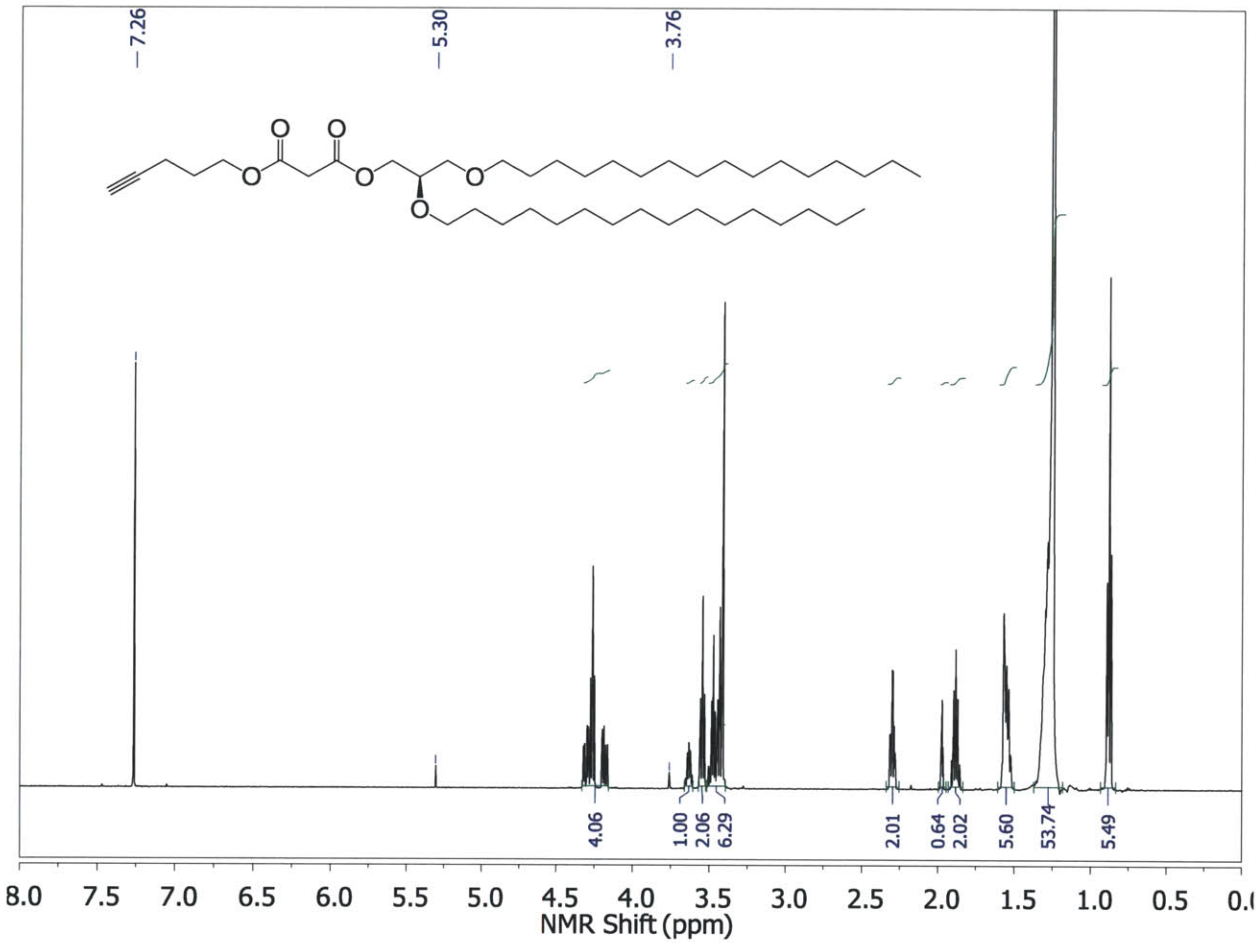

^{1}H-NMR in $CDCl_3$

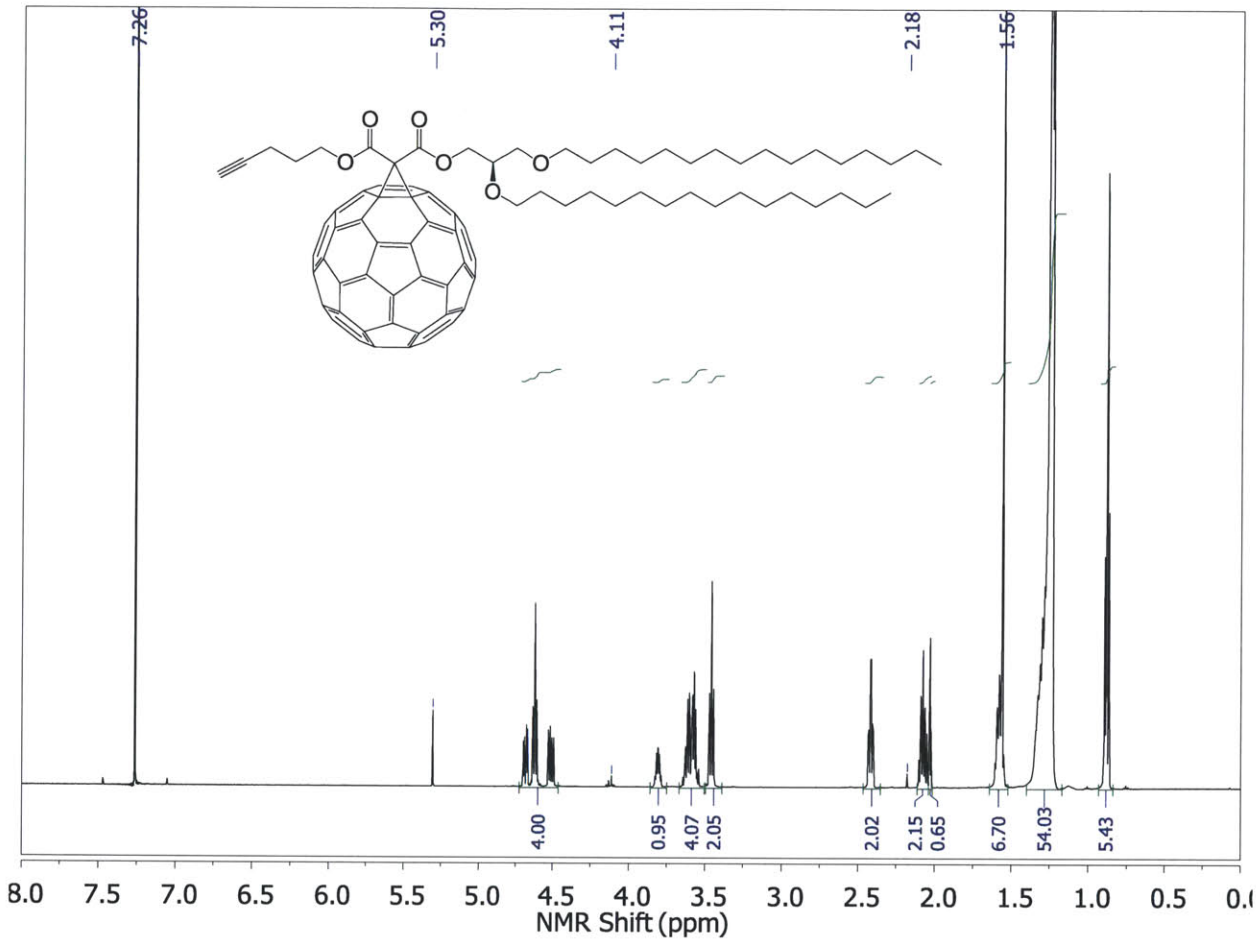

^{1}H-NMR in $CDCl_3$

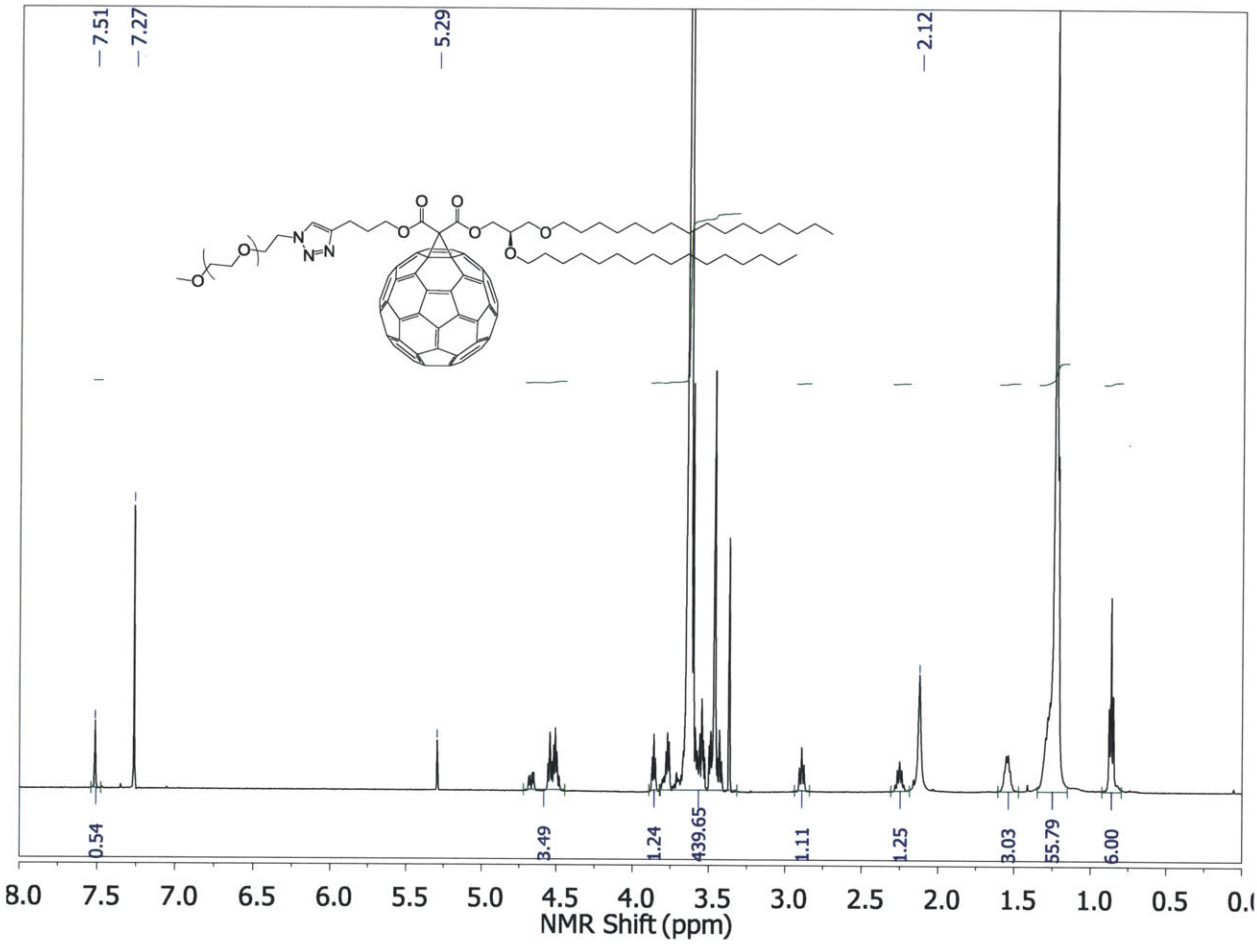

^{1}H-NMR in $CDCl_3$

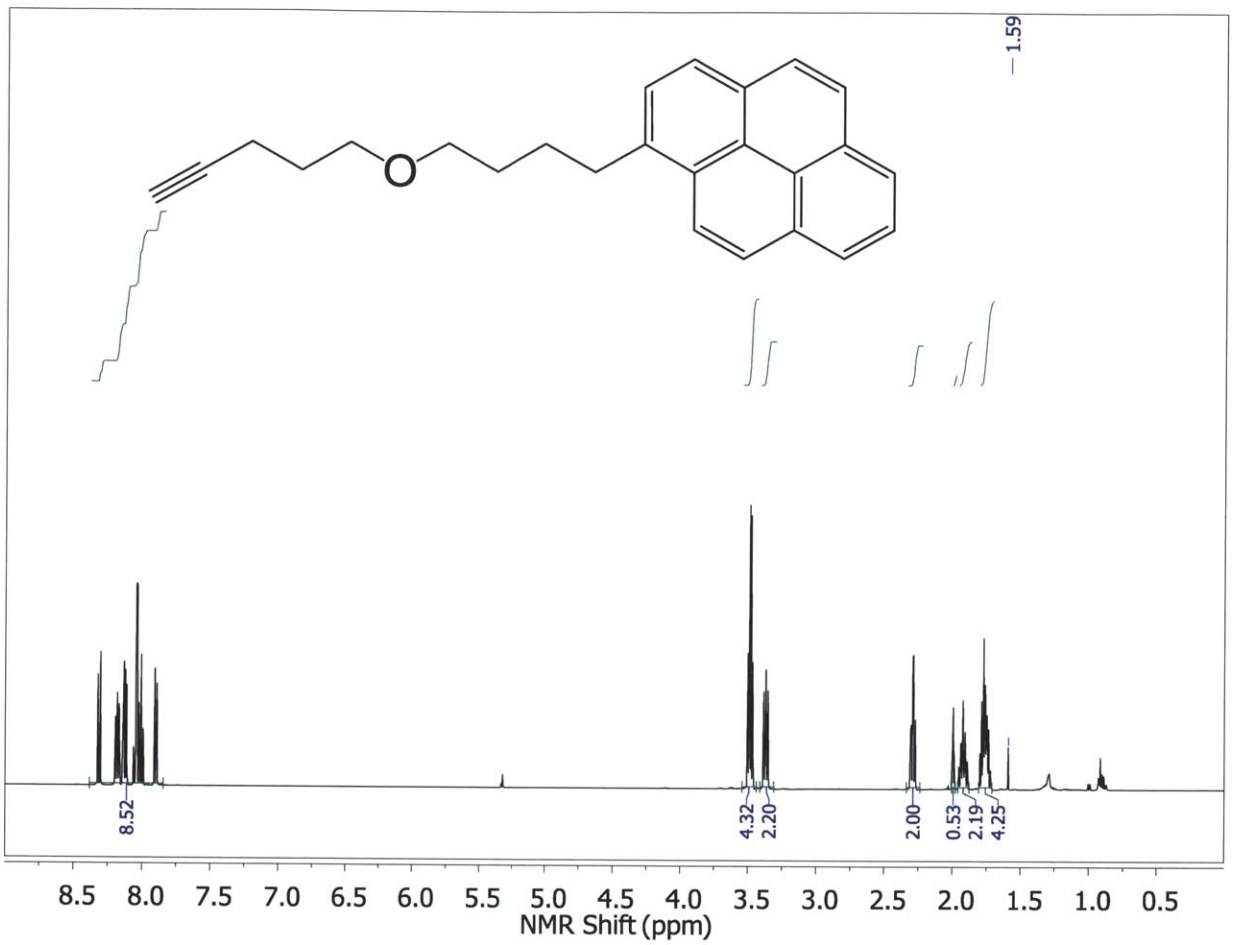

^{1}H-NMR in CD_2Cl_2

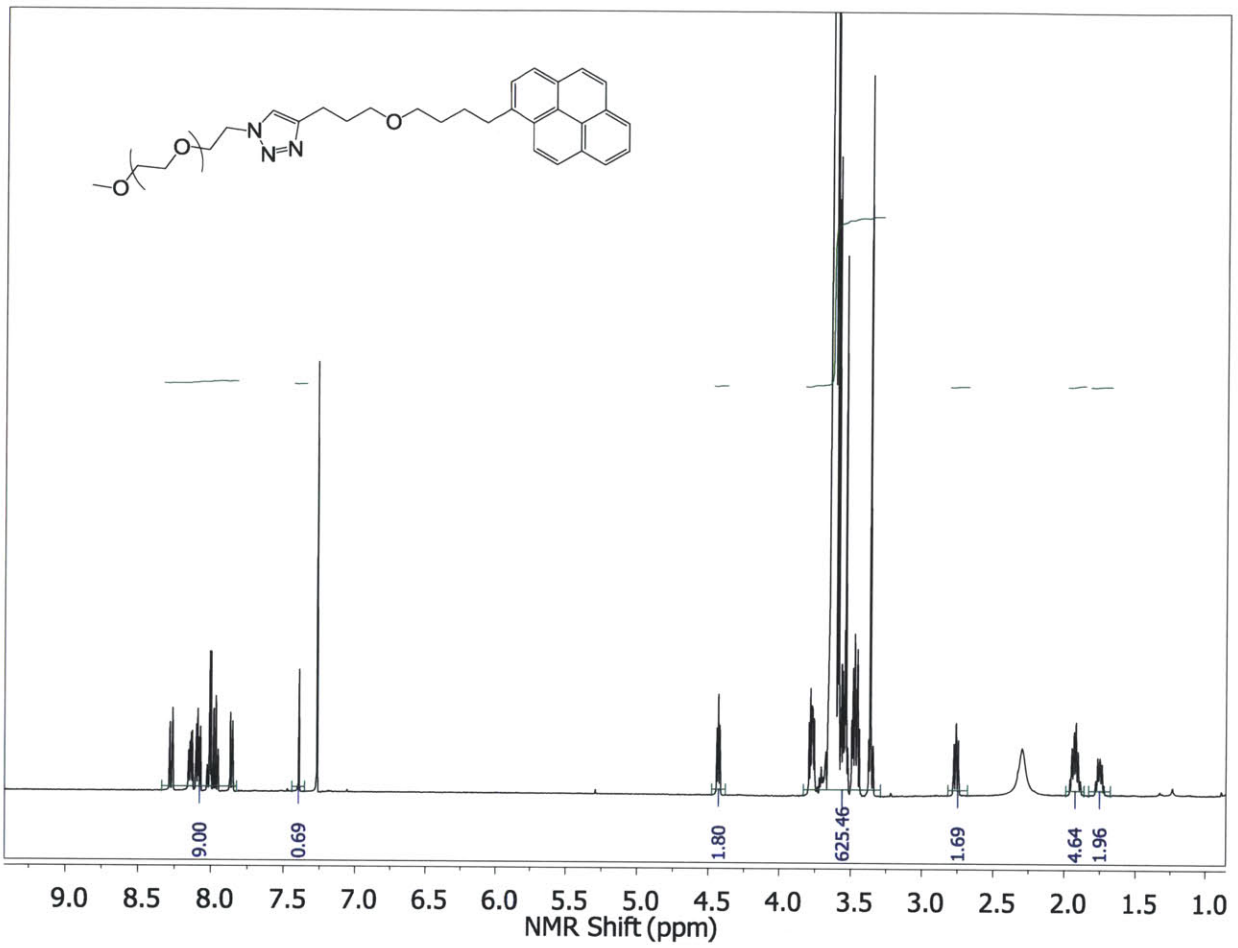

^{1}H-NMR in $CDCl_3$

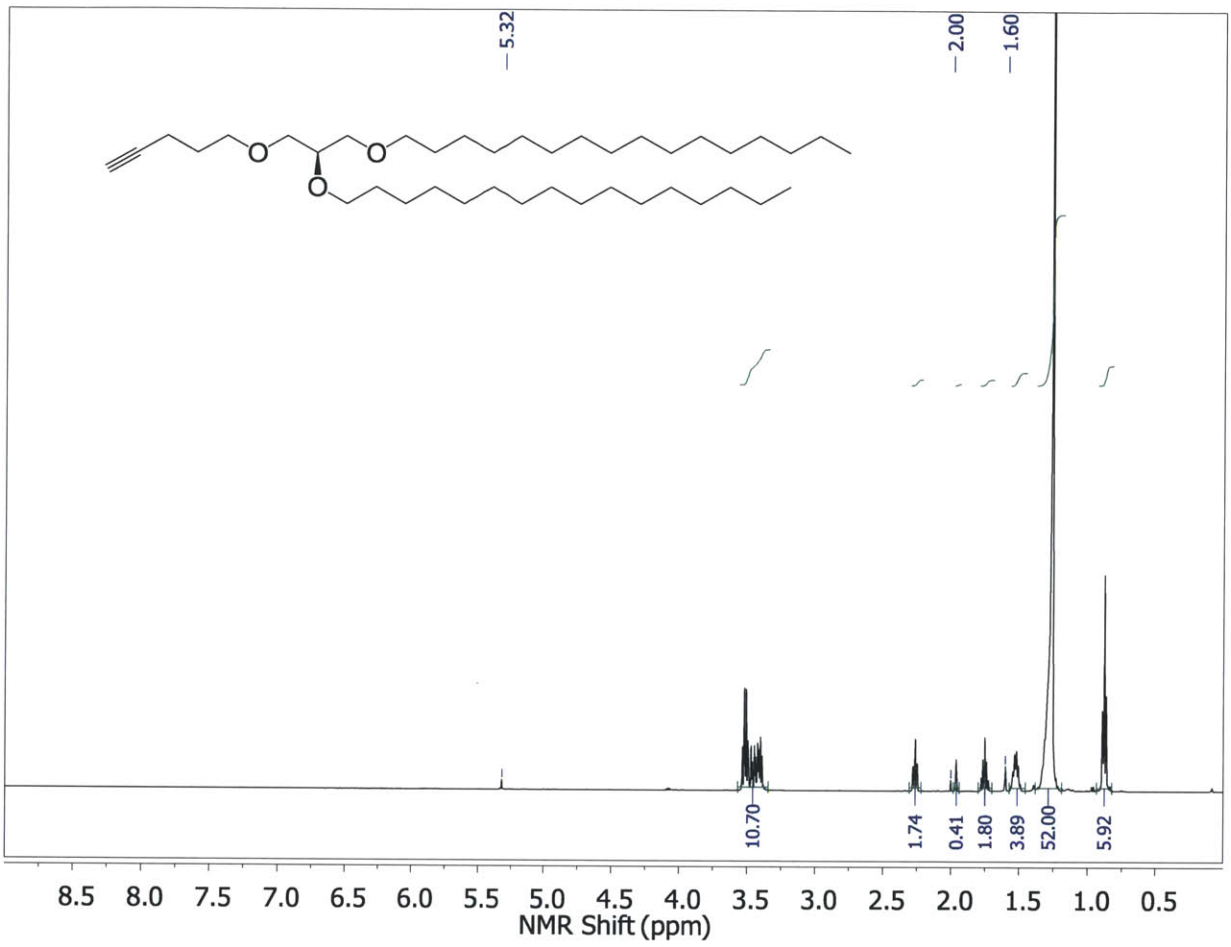

^{1}H-NMR in CD_2Cl_2

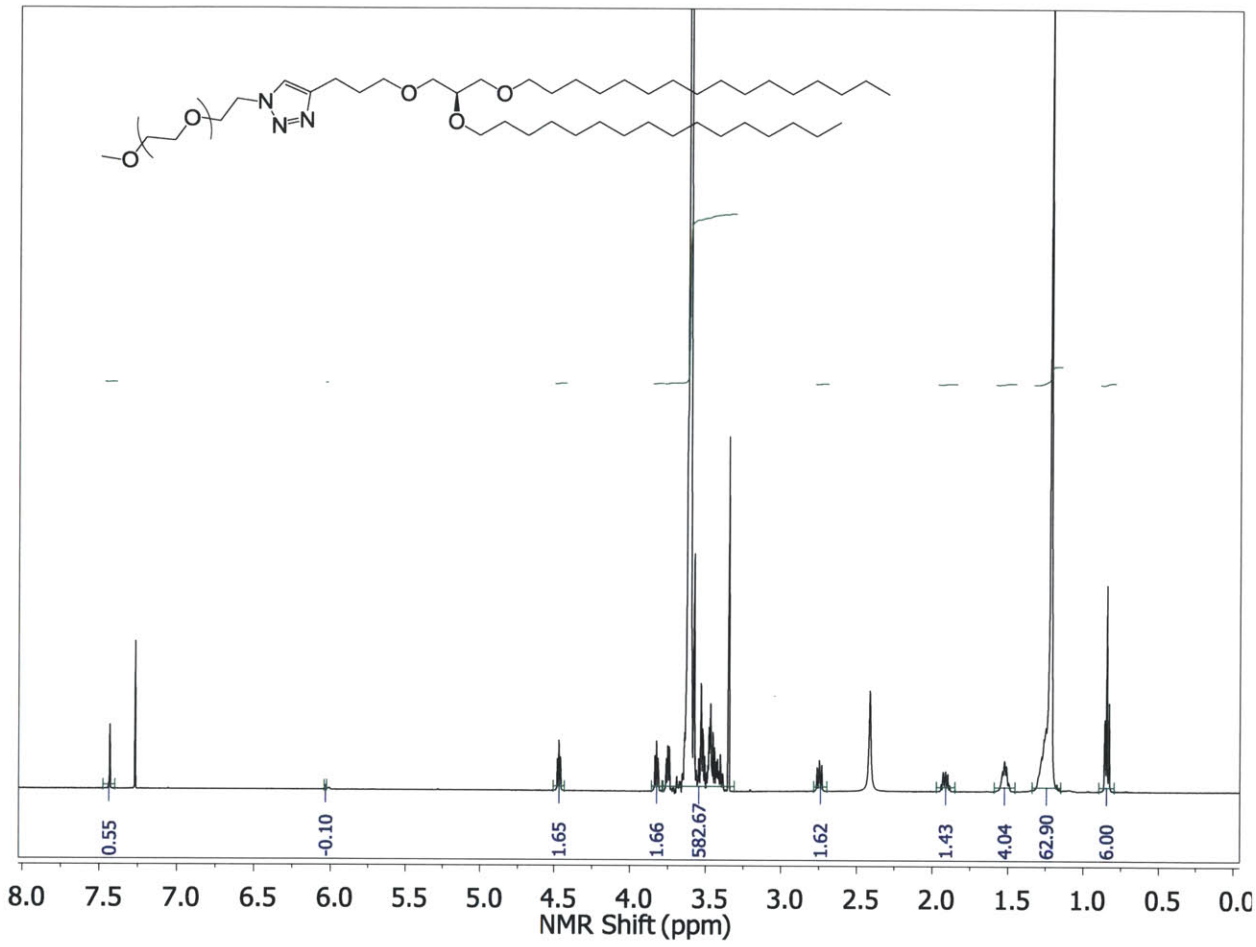

^{1}H-NMR in $CDCl_3$

8 Appendix B: Molecular Characterization of Fullerodendrimers

8.2 MALDI-TOF

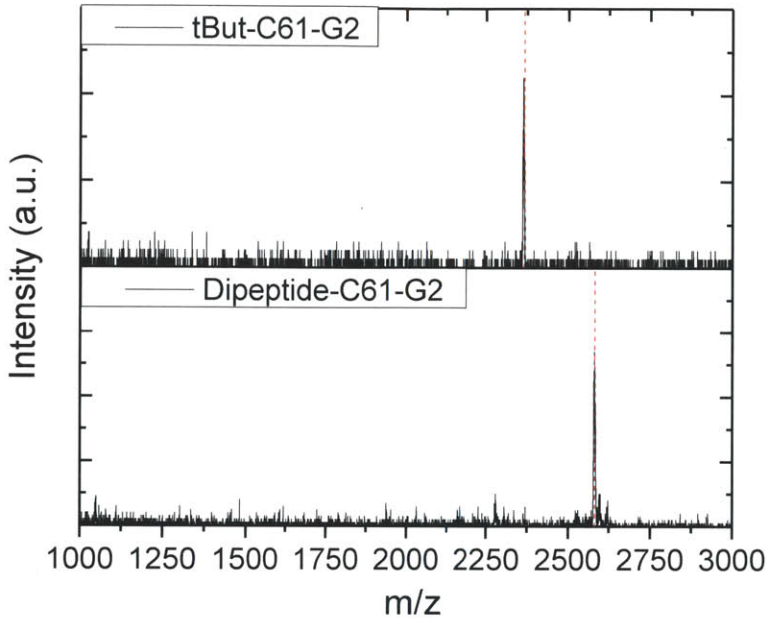

Figure 8.1 MALDI-TOF data for the two fullerodendrimers used in the self-assembly study.

8.3 Variable-Temperature NMR (VT-NMR)

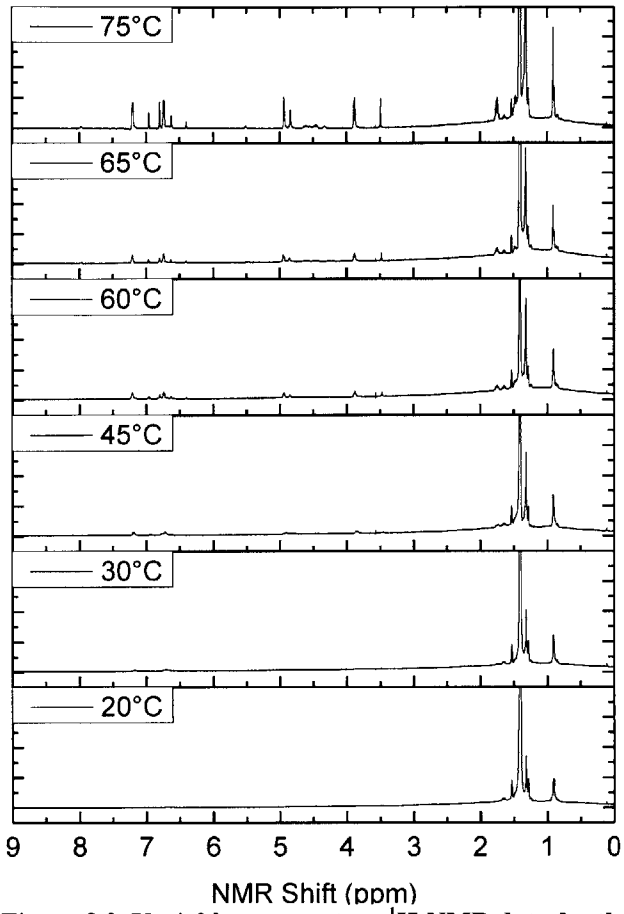

Figure 8.2 Variable temperature ^{1}H-NMR data for the peptidic fullerodendrimer in C_6D_{12}.

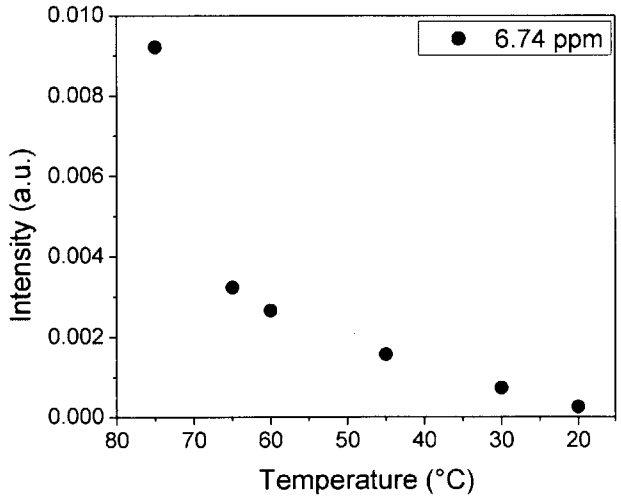

Figure 8.3 Intensity of the aromatic NMR feature at ~6.74ppm as a function of temperature. The magnitude of the feature shows a monotonic decrease as the sample is cooled. Due to the higher concentration of the sample, the assembly transition is shifted to higher temperatures in comparison with the variable-temperature absorbance and circular dichroism datasets.

8.4 NMR

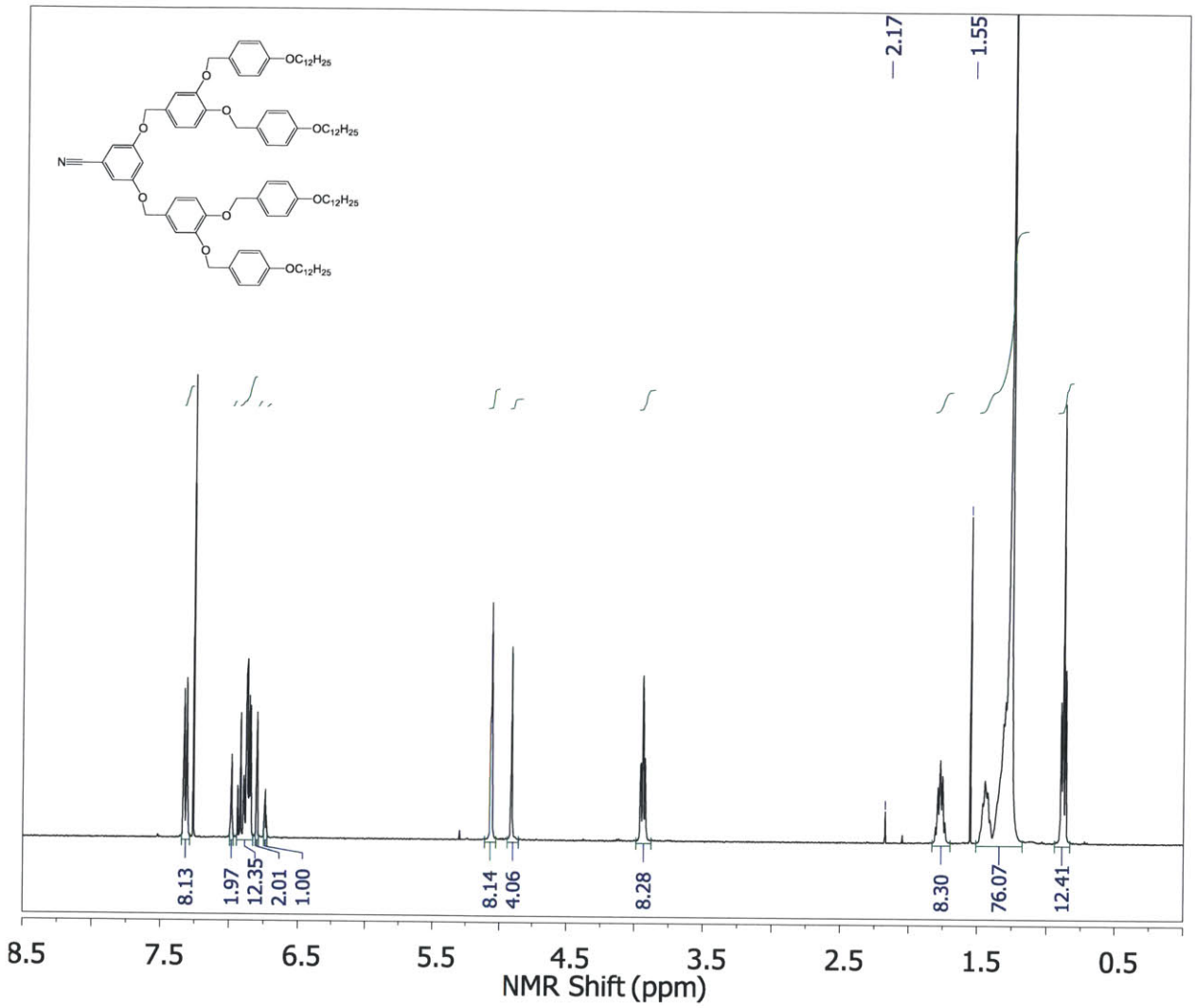

^{1}H-NMR in $CDCl_3$

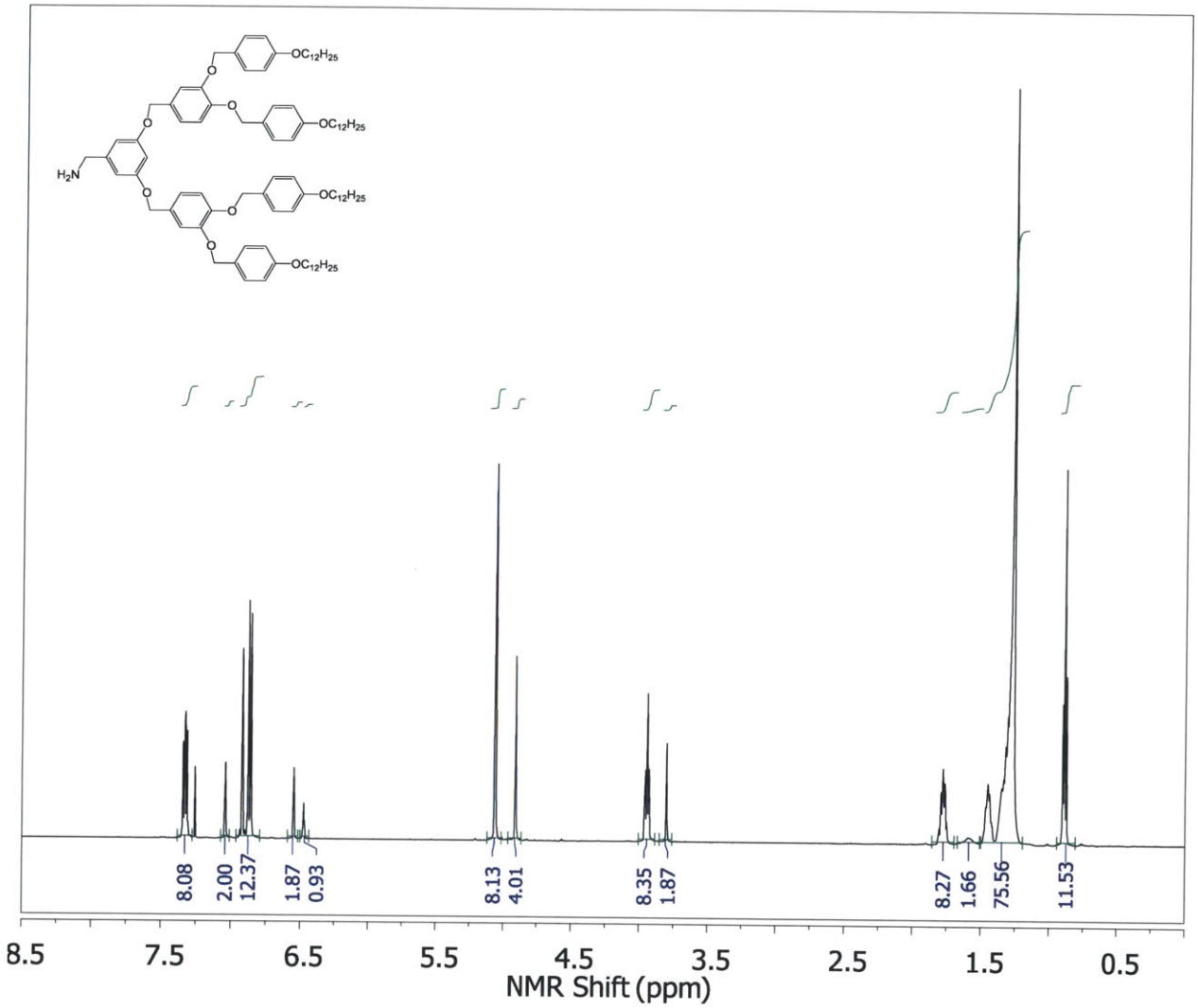

^{1}H-NMR in $CDCl_3$

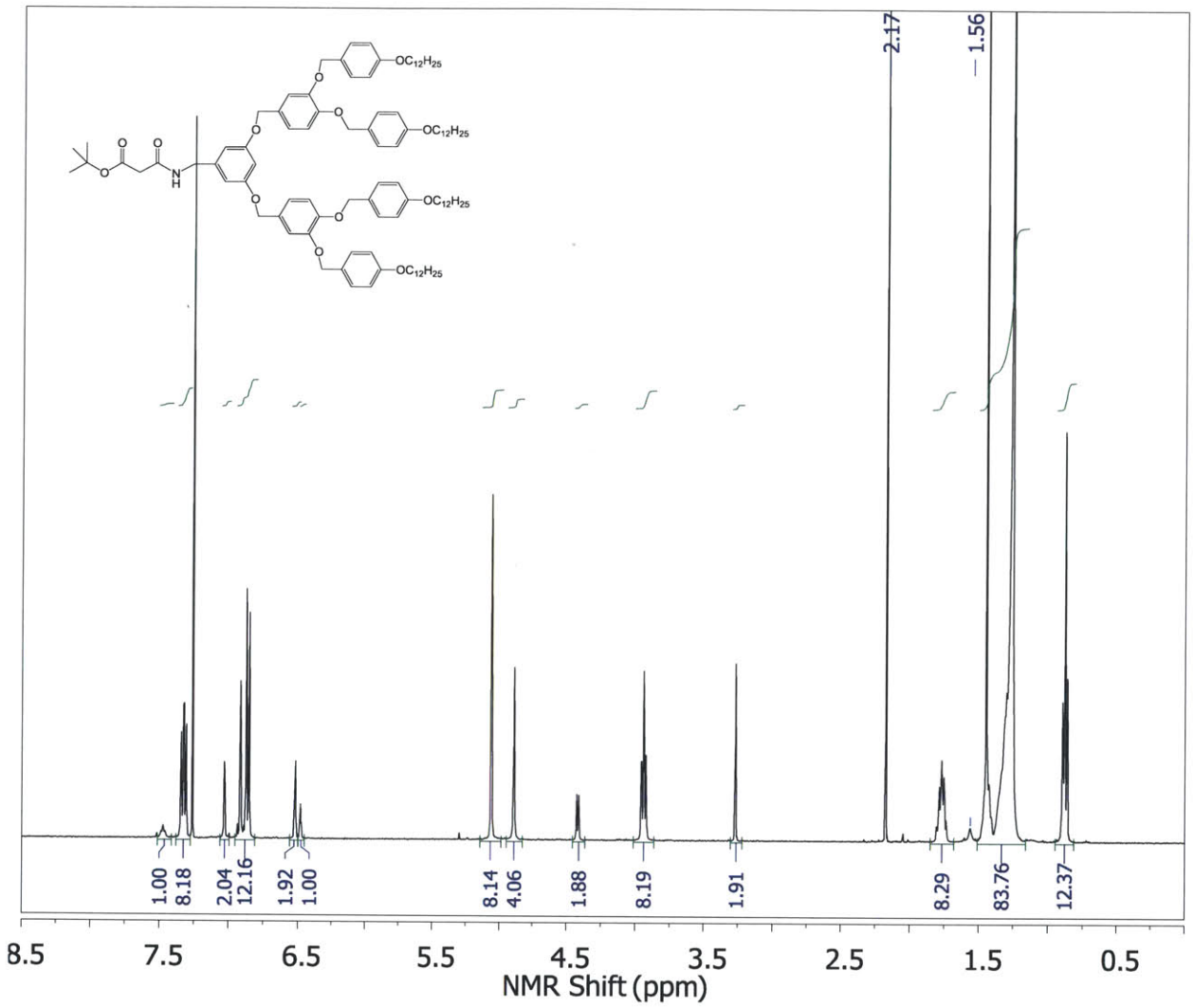

^{1}H-NMR in $CDCl_3$

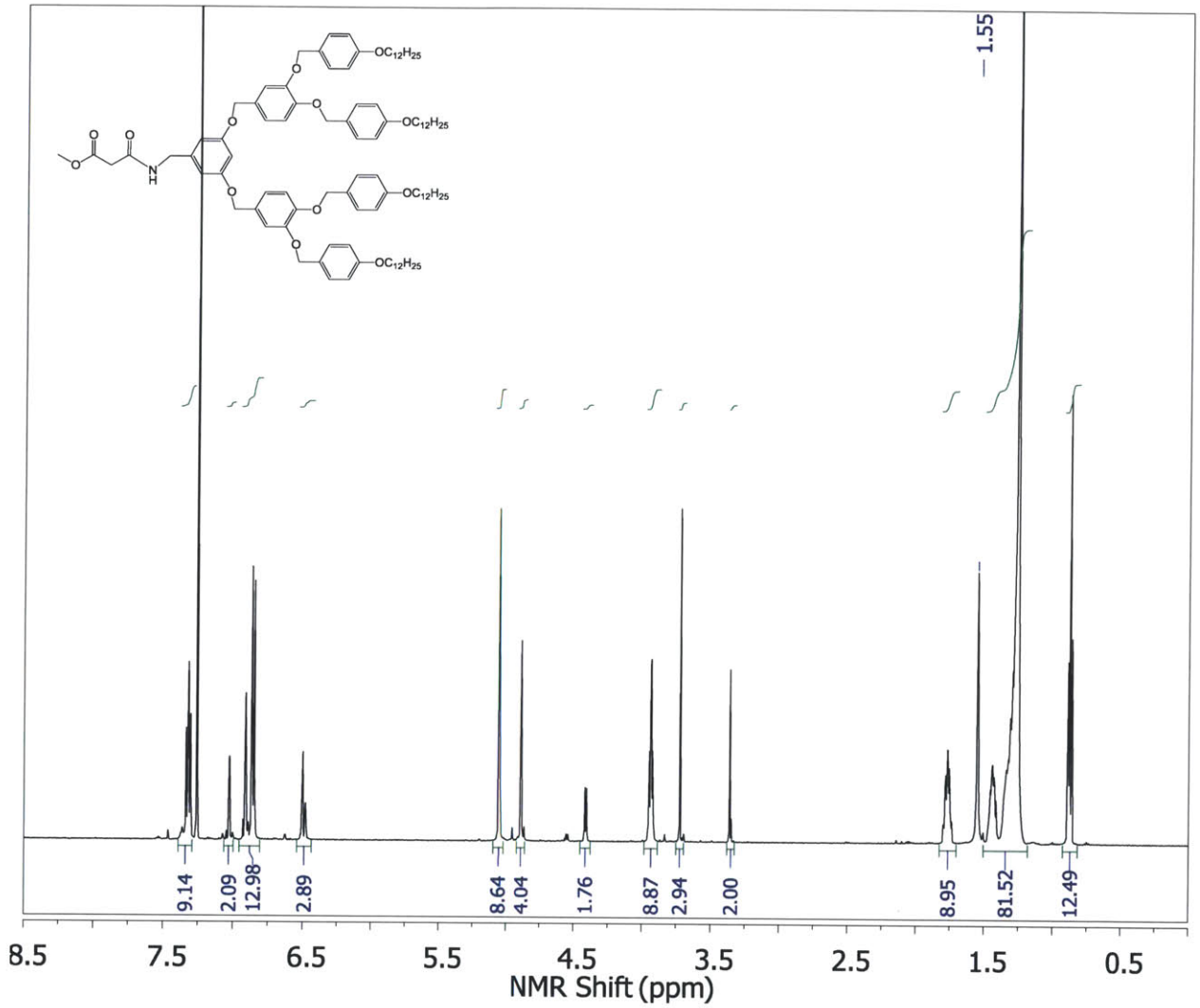

^{1}H-NMR in $CDCl_3$

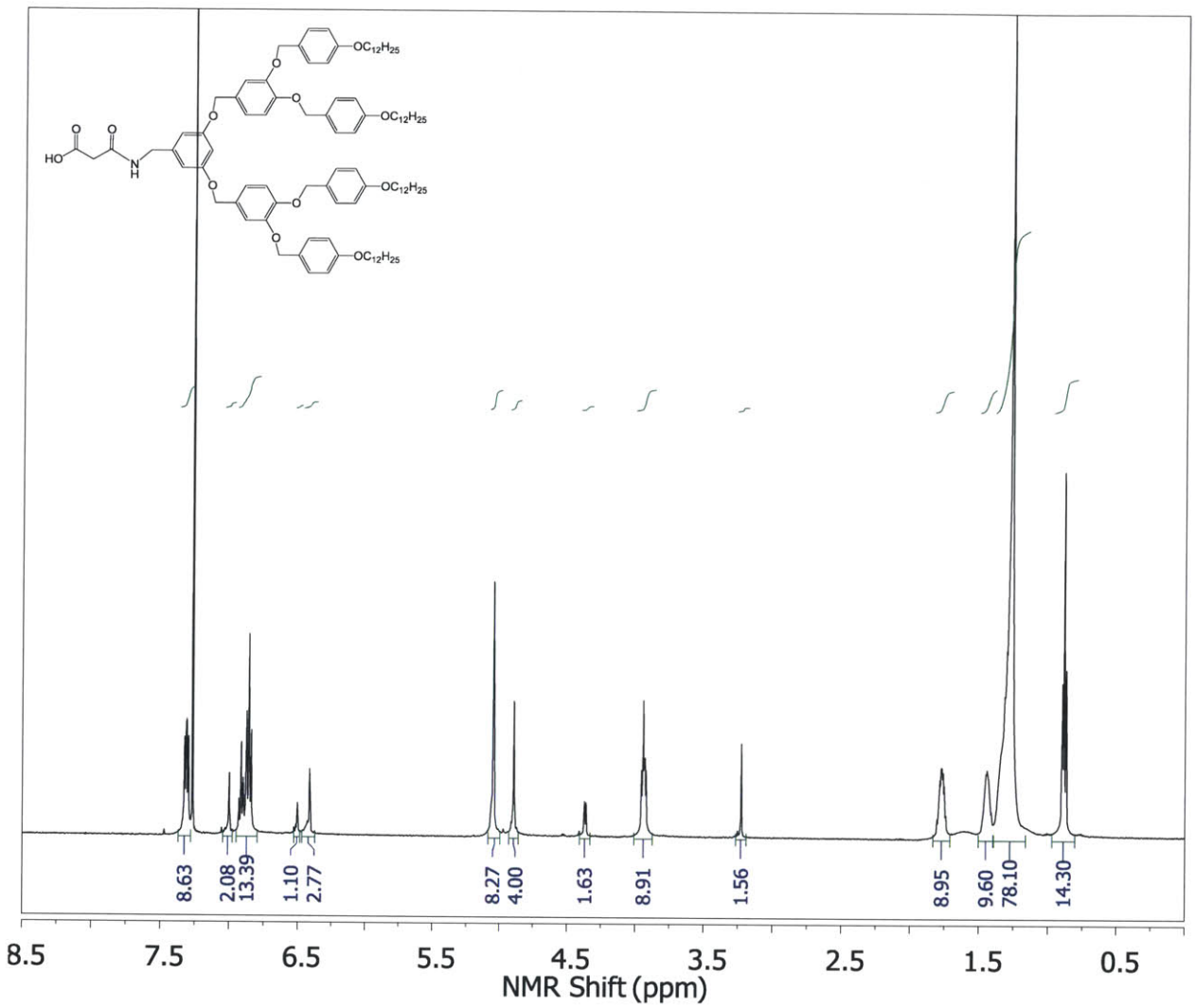

^{1}H-NMR in $CDCl_3$

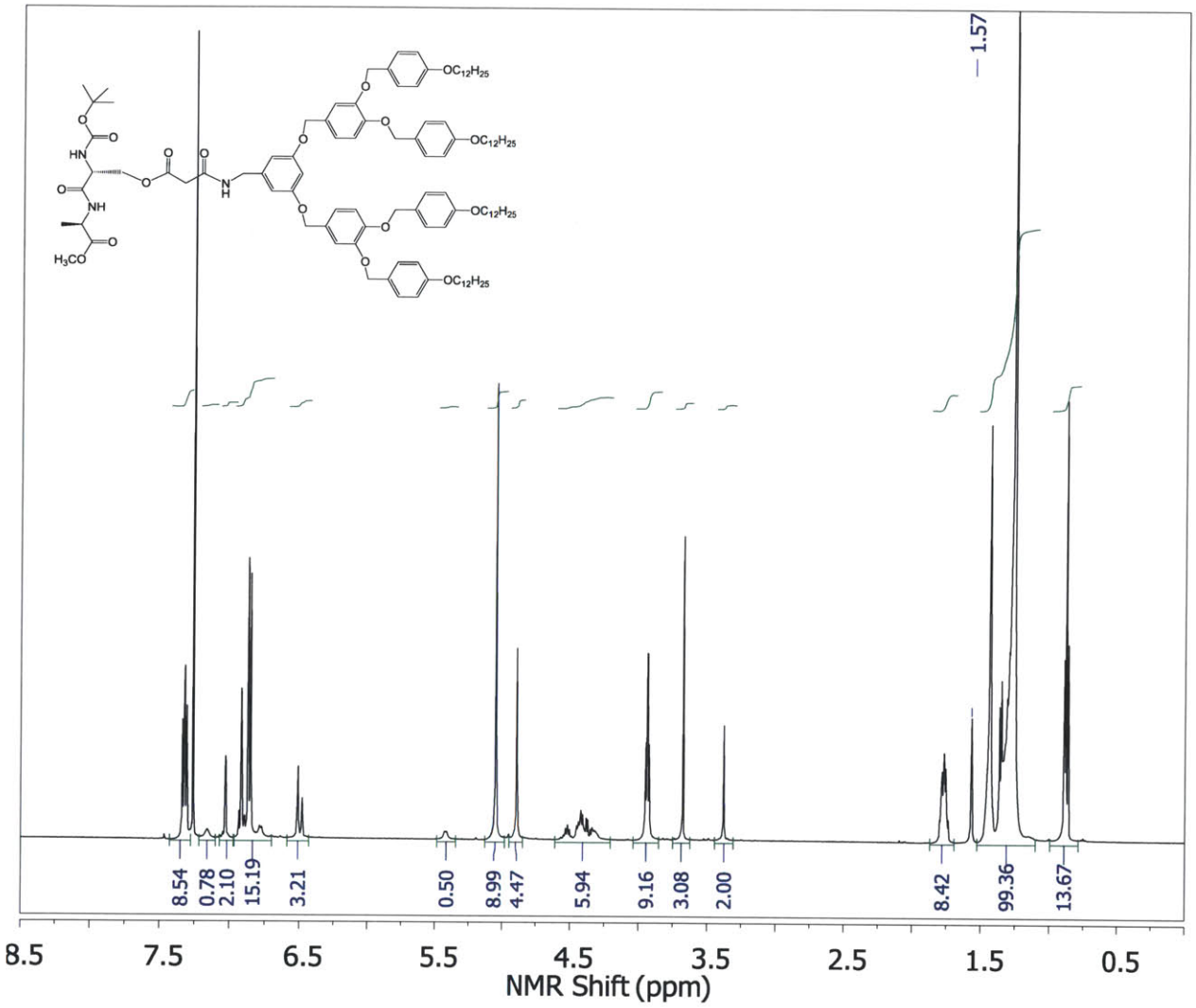

^{1}H-NMR in $CDCl_3$

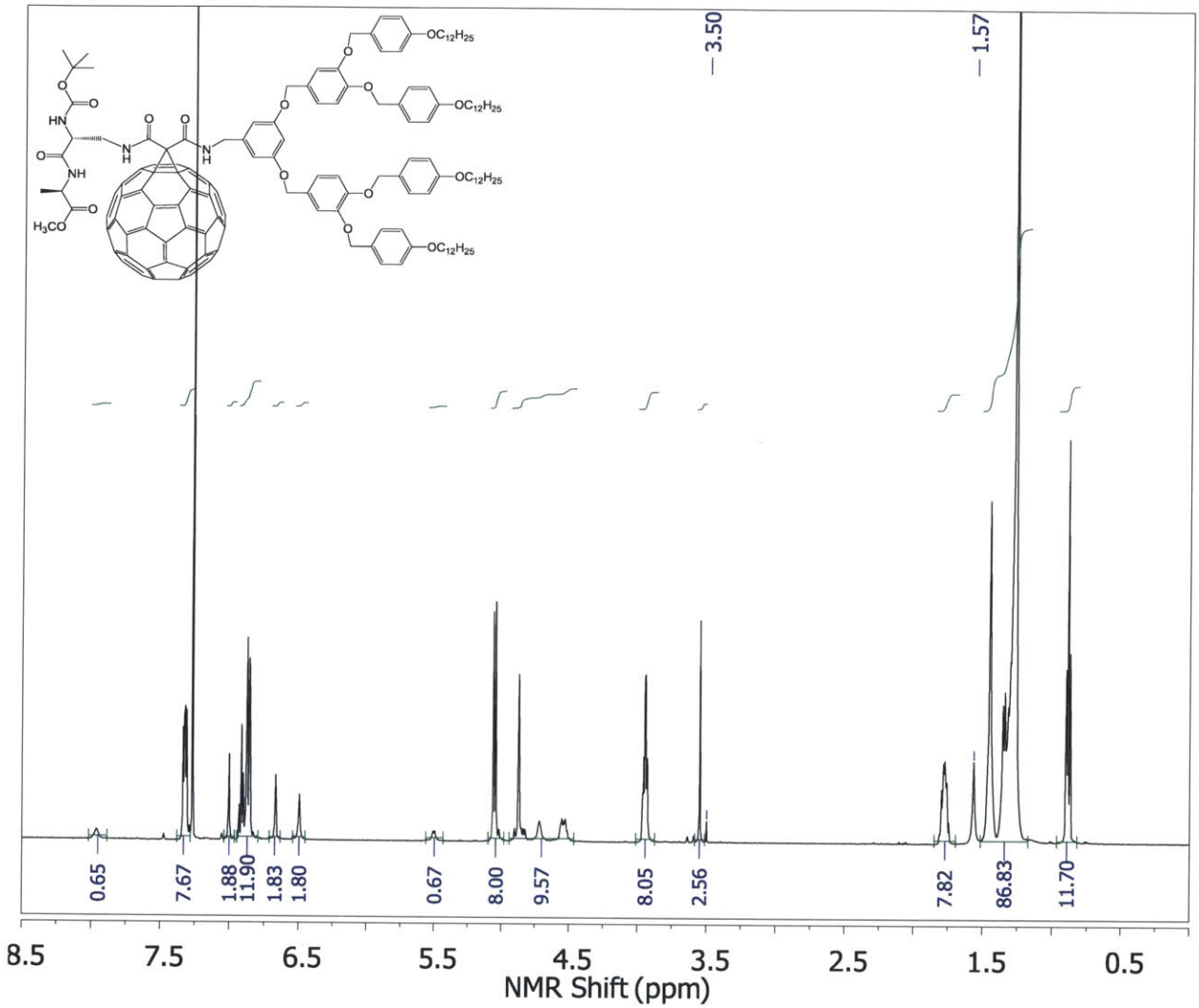

^{1}H-NMR in $CDCl_3$

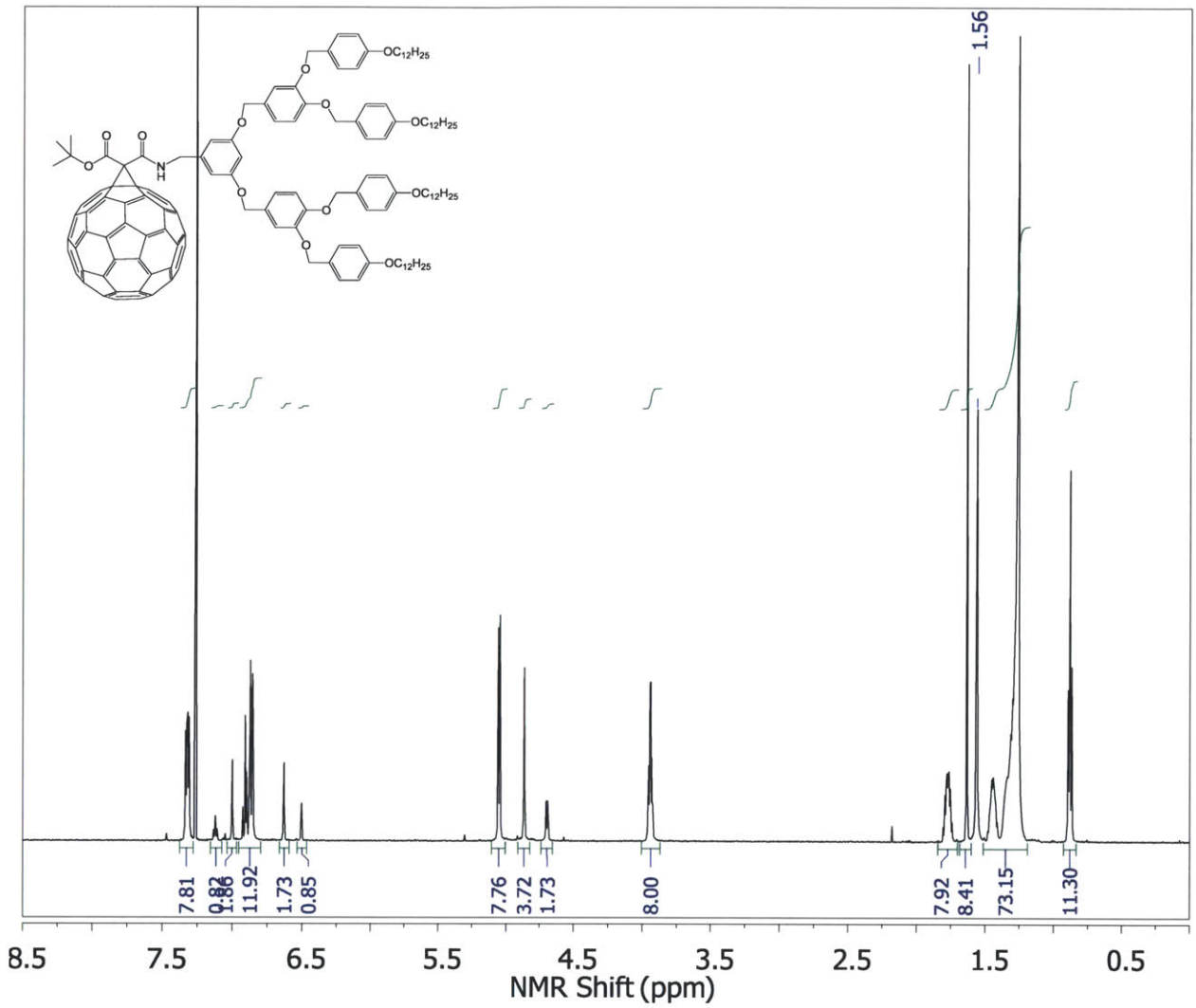

^{1}H-NMR in $CDCl_3$

9 References

1. Paulus, G.L.C., et al., *The Chemical Engineering of Low-Dimensional Materials.* Aiche Journal, 2011. **57**(5): p. 1104-1118.
2. Park, H., J.J. Zhao, and J.P. Lu, *Distinct properties of single-wall carbon nanotubes with monovalent sidewall additions.* Nanotechnology, 2005. **16**(6): p. 635-638.
3. Dresselhaus, M.S., G. Dresselhaus, and P.C. Eklund, *Science of fullerenes and carbon nanotubes*. 1996, San Diego: Academic Press. xviii, 965 p.
4. Reich, S., C. Thomsen, and J. Maultzsch, *Carbon nanotubes : basic concepts and physical properties*. 2004, Weinheim ; Cambridge: Wiley-VCH. ix, 215 p.
5. Dai, H.J., *Carbon nanotubes: opportunities and challenges.* Surface Science, 2002. **500**(1-3): p. 218-241.
6. Graham, M.W., et al., *Two-Dimensional Electronic Spectroscopy Reveals the Dynamics of Phonon-Mediated Excitation Pathways in Semiconducting Single-Walled Carbon Nanotubes.* Nano Letters, 2012. **12**(2): p. 813-819.
7. Choi, C.L. and A.P. Alivisatos, *From Artificial Atoms to Nanocrystal Molecules: Preparation and Properties of More Complex Nanostructures.* Annual Review of Physical Chemistry, 2010. **61**(1): p. 369-389.
8. Novak, J.P. and D.L. Feldheim, *Assembly of phenylacetylene-bridged silver and gold nanoparticle arrays.* Journal of the American Chemical Society, 2000. **122**(16): p. 3979-3980.
9. Loweth, C.J., et al., *DNA-based assembly of gold nanocrystals.* Angewandte Chemie-International Edition, 1999. **38**(12): p. 1808-1812.
10. Zanchet, D., et al., *Electrophoretic and structural studies of DNA-directed Au nanoparticle groupings.* Journal of Physical Chemistry B, 2002. **106**(45): p. 11758-11763.
11. Fu, A.H., et al., *Discrete nanostructures of quantum dots/Au with DNA.* Journal of the American Chemical Society, 2004. **126**(35): p. 10832-10833.
12. Sonnichsen, C., et al., *A molecular ruler based on plasmon coupling of single gold and silver nanoparticles.* Nature Biotechnology, 2005. **23**(6): p. 741-745.
13. Reinhard, B.M., et al., *Use of plasmon coupling to reveal the dynamics of DNA bending and cleavage by single EcoRV restriction enzymes.* Proceedings of the National Academy of Sciences of the United States of America, 2007. **104**(8): p. 2667-2672.
14. Jun, Y.W., et al., *Continuous imaging of plasmon rulers in live cells reveals early-stage caspase-3 activation at the single-molecule level.* Proceedings of the National Academy of Sciences of the United States of America, 2009. **106**(42): p. 17735-17740.
15. Howarth, M., et al., *Monovalent, reduced-size quantum dots for imaging receptors on living cells.* Nature Methods, 2008. **5**(5): p. 397-399.
16. Howarth, M. and A.Y. Ting, *Imaging proteins in live mammalian cells with biotin ligase and monovalent streptavidin.* Nat. Protocols, 2008. **3**(3): p. 534-545.
17. Voiry, D., O. Roubeau, and A. Penicaud, *Stoichiometric control of single walled carbon nanotubes functionalization.* J. Mater. Chem., 2010. **20**(Copyright (C) 2010 American Chemical Society (ACS). All Rights Reserved.): p. 4385-4391.
18. Brunetti, F.G., et al., *Microwave-induced multiple functionalization of carbon nanotubes.* Journal of the American Chemical Society, 2008. **130**(25): p. 8094-8100.

19. Peng, X.H. and S.S. Wong, *Controlling Nanocrystal Density and Location on Carbon Nanotube Templates.* Chemistry of Materials, 2009. **21**(4): p. 682-694.
20. Li, X.H., et al., *Labeling the defects of single-walled carbon nanotubes using titanium dioxide nanoparticles.* Journal of Physical Chemistry B, 2003. **107**(11): p. 2453-2458.
21. Del Canto, E., et al., *Critical Investigation of Defect Site Functionalization on Single-Walled Carbon Nanotubes.* Chemistry of Materials, 2010. **23**(1): p. 67-74.
22. Bachilo, S.M., et al., *Structure-assigned optical spectra of single-walled carbon nanotubes.* Science, 2002. **298**(5602): p. 2361-2366.
23. Banerjee, S. and S.S. Wong, *Selective Metallic Tube Reactivity in the Solution-Phase Osmylation of Single-Walled Carbon Nanotubes.* Journal of the American Chemical Society, 2004. **126**(7): p. 2073-2081.
24. Strano, M.S., et al., *Electronic structure control of single-walled carbon nanotube functionalization.* Science, 2003. **301**(5639): p. 1519-1522.
25. Graupner, R., et al., *Nucleophilic−Alkylation−Reoxidation: A Functionalization Sequence for Single-Wall Carbon Nanotubes.* Journal of the American Chemical Society, 2006. **128**(20): p. 6683-6689.
26. Li, J.Q., et al., *Bond-curvature effect of sidewall [2+1] cycloadditions of single-walled carbon nanotubes: A new criterion to the adduct structures.* Chemistry of Materials, 2006. **18**(15): p. 3579-3584.
27. Weizmann, Y., et al., *Regiospecific Synthesis of Au-Nanorod/SWCNT/Au-Nanorod Heterojunctions.* Nano Letters, 2010.
28. Weizmann, Y., D.M. Chenoweth, and T.M. Swager, *Addressable Terminally Linked DNA−CNT Nanowires.* Journal of the American Chemical Society, 2010. **132**(40): p. 14009-14011.
29. Palma, M., et al., *Controlled formation of carbon nanotube junctions via linker induced assembly in aqueous solution.* Journal of the American Chemical Society, 2013.
30. Usrey, M.L., E.S. Lippmann, and M.S. Strano, *Evidence for a two-step mechanism in electronically selective single-walled carbon nanotube reactions.* Journal of the American Chemical Society, 2005. **127**(46): p. 16129-16135.
31. Wang, H.M. and J.S. Xu, *Theoretical evidence for a two-step mechanism in the functionalization single-walled carbon nanotube by aryl diazonium salts: Comparing effect of different substituent group.* Chemical Physics Letters, 2009. **477**(1-3): p. 176-178.
32. Nair, N., et al., *A structure-reactivity relationship for single walled carbon nanotubes reacting with 4-hydroxybenzene diazonium salt.* Journal of the American Chemical Society, 2007. **129**(13): p. 3946-3954.
33. Eyring, H., *Electrochemistry.* Physical chemistry, an advanced treatise, v. 9. 1970, New York,: Academic Press. v.
34. Sumpter, B.G., D.-E. Jiang, and V. Meunier, *New Insight into Carbon-Nanotube Electronic-Structure Selectivity.* Small, 2008. **4**(11): p. 2035-2042.
35. Lewis, N.S. and D.G. Nocera, *Powering the planet: Chemical challenges in solar energy utilization.* Proceedings of the National Academy of Sciences of the United States of America, 2006. **103**(43): p. 15729-15735.
36. Barone, P.W., R.S. Parker, and M.S. Strano, *In vivo fluorescence detection of glucose using a single-walled carbon nanotube optical sensor: Design, fluorophore properties, advantages, and disadvantages.* Analytical Chemistry, 2005. **77**(23): p. 7556-7562.

37. Durkop, T., et al., *Extraordinary mobility in semiconducting carbon nanotubes.* Nano Letters, 2004. **4**(1): p. 35-39.
38. Jain, R.M., et al., *Polymer-Free Near-Infrared Photovoltaics with Single Chirality (6,5) Semiconducting Carbon Nanotube Active Layers.* Advanced Materials, 2012: p. n/a-n/a.
39. Bernardi, M., et al., *Nanocarbon-Based Photovoltaics.* Acs Nano, 2012. **6**(10): p. 8896-8903.
40. Ramuz, M.P., et al., *Evaluation of Solution-Processable Carbon-Based Electrodes for All-Carbon Solar Cells.* Acs Nano, 2012. **6**(11): p. 10384-10395.
41. Bindl, D.J. and M.S. Arnold, *Efficient Exciton Relaxation and Charge Generation in Nearly Monochiral (7,5) Carbon Nanotube/C60 Thin-Film Photovoltaics.* The Journal of Physical Chemistry C, 2013. **117**(5): p. 2390-2395.
42. Sandanayaka, A.S.D., et al., *Diameter dependent electron transfer in supramolecular nanohybrids of (6,5)- or (7,6)-enriched semiconducting SWCNT as donors and fullerene as acceptor.* Chemical Communications, 2010. **46**(46): p. 8749-8751.
43. D'Souza, F., et al., *Supramolecular carbon nanotube-fullerene donor-acceptor hybrids for photoinduced electron transfer.* Journal of the American Chemical Society, 2007. **129**(51): p. 15865-15871.
44. Kooistra, F.B., et al., *New C84 Derivative and Its Application in a Bulk Heterojunction Solar Cell.* Chemistry of Materials, 2006. **18**(13): p. 3068-3073.
45. Juha, L., et al., *Single-photon photolysis of C-60, C-70, C-76, and C-84 in solutions.* Chemical Physics Letters, 2001. **335**(5-6): p. 539-544.
46. Zhang, J., et al., *Single Molecule Detection of Nitric Oxide Enabled by d(AT)15 DNA Adsorbed to Near Infrared Fluorescent Single-Walled Carbon Nanotubes.* Journal of the American Chemical Society, 2010. **133**(3): p. 567-581.
47. Kim, J.H., et al., *The rational design of nitric oxide selectivity in single-walled carbon nanotube near-infrared fluorescence sensors for biological detection.* Nature Chemistry, 2009. **1**(6): p. 473-481.
48. Jin, H., et al., *Detection of single-molecule H2O2 signalling from epidermal growth factor receptor using fluorescent single-walled carbon nanotubes.* Nature Nanotechnology, 2010. **5**(4): p. 302-U81.
49. Mu, B., et al., *A Structure–Function Relationship for the Optical Modulation of Phenyl Boronic Acid-Grafted, Polyethylene Glycol-Wrapped Single-Walled Carbon Nanotubes.* Journal of the American Chemical Society, 2012. **134**(42): p. 17620-17627.
50. Kim, J.H., et al., *A Luciferase/Single-Walled Carbon Nanotube Conjugate for Near-Infrared Fluorescent Detection of Cellular ATP.* Angewandte Chemie-International Edition, 2010. **49**(8): p. 1456-1459.
51. Boghossian, A.A., et al., *Near-Infrared Fluorescent Sensors based on Single-Walled Carbon Nanotubes for Life Sciences Applications.* Chemsuschem, 2011. **4**(7): p. 848-863.
52. Ahn, J.-H., et al., *Label-Free, Single Protein Detection on a Near-Infrared Fluorescent Single-Walled Carbon Nanotube/Protein Microarray Fabricated by Cell-Free Synthesis.* Nano Letters, 2011. **11**(7): p. 2743-2752.
53. Guldi, D.M. and K.D. Asmus, *Photophysical properties of mono- and multiply-functionalized fullerene derivatives.* Journal of Physical Chemistry A, 1997. **101**(8): p. 1472-1481.
54. Reich, S., et al., *Excited-state carrier lifetime in single-walled carbon nanotubes.* Physical Review B, 2005. **71**(3).

55. Moser, C.C., et al., *Nature of Biological Electron-Transfer.* Nature, 1992. **355**(6363): p. 796-802.
56. Tanaka, Y., et al., *Determination of electronic states of individually dissolved (n,m) single-walled carbon nanotubes in solution.* Chemical Physics Letters, 2009. **482**(1–3): p. 114-117.
57. Ohkubo, K., et al., *Small reorganization energy of intramolecular electron transfer in fullerene-based dyads with short linkage.* Journal of Physical Chemistry A, 2002. **106**(46): p. 10991-10998.
58. Guldi, D.M., et al., *Zwitterionic Acceptor Moieties: Small Reorganization Energy and Unique Stabilization of Charge Transfer Products†.* The Journal of Physical Chemistry B, 2003. **107**(30): p. 7293-7298.
59. Imahori, H., et al., *Modulating Charge Separation and Charge Recombination Dynamics in Porphyrin−Fullerene Linked Dyads and Triads: Marcus-Normal versus Inverted Region.* Journal of the American Chemical Society, 2001. **123**(11): p. 2607-2617.
60. Imahori, H., et al., *An extremely small reorganization energy of electron transfer in porphyrin-fullerene dyad.* Journal of Physical Chemistry A, 2001. **105**(10): p. 1750-1756.
61. Babu, S.S., H. Mohwald, and T. Nakanishi, *Recent progress in morphology control of supramolecular fullerene assemblies and its applications.* Chemical Society Reviews, 2010. **39**(11): p. 4021-4035.
62. Li, H., et al., *Alkylated-C60 based soft materials: regulation of self-assembly and optoelectronic properties by chain branching.* Journal of Materials Chemistry C, 2013. **1**(10): p. 1943-1951.
63. Mas-Torrent, M. and C. Rovira, *Novel small molecules for organic field-effect transistors: towards processability and high performance.* Chemical Society Reviews, 2008. **37**(4): p. 827-838.
64. Delgado, J.L., et al., *Organic photovoltaics: a chemical approach.* Chemical Communications, 2010. **46**(27): p. 4853-4865.
65. Liu, T. and A. Troisi, *What Makes Fullerene Acceptors Special as Electron Acceptors in Organic Solar Cells and How to Replace Them.* Advanced Materials, 2013. **25**(7): p. 1038-1041.
66. Yu, G., et al., *Polymer Photovoltaic Cells - Enhanced Efficiencies Via a Network of Internal Donor-Acceptor Heterojunctions.* Science, 1995. **270**(5243): p. 1789-1791.
67. Chen, W., M.P. Nikiforov, and S.B. Darling, *Morphology characterization in organic and hybrid solar cells.* Energy & Environmental Science, 2012. **5**(8): p. 8045-8074.
68. Yang, X. and J. Loos, *Toward High-Performance Polymer Solar Cells: The Importance of Morphology Control.* Macromolecules, 2007. **40**(5): p. 1353-1362.
69. Feng, M., J. Zhao, and H. Petek, *Atomlike, Hollow-Core–Bound Molecular Orbitals of C60.* Science, 2008. **320**(5874): p. 359-362.
70. Zhao, J., et al., *The Superatom States of Fullerenes and Their Hybridization into the Nearly Free Electron Bands of Fullerites.* Acs Nano, 2009. **3**(4): p. 853-864.
71. Ganin, A.Y., et al., *Polymorphism control of superconductivity and magnetism in Cs3C60 close to the Mott transition.* Nature, 2010. **466**(7303): p. 221-225.
72. Hebard, A.F., et al., *Superconductivity at 18 K in potassium-doped C60.* Nature, 1991. **350**(6319): p. 600-601.
73. Tanigaki, K., et al., *Superconductivity at 33 K in CsxRbyC60.* Nature, 1991. **352**(6332): p. 222-223.

74. Nakanishi, T., *Supramolecular soft and hard materials based on self-assembly algorithms of alkyl-conjugated fullerenes.* Chemical Communications, 2010. **46**(20): p. 3425-3436.
75. Tsunashima, R., et al., *Fullerene Nanowires: Self-Assembled Structures of a Low-Molecular-Weight Organogelator Fabricated by the Langmuir-Blodgett Method.* Chemistry-a European Journal, 2008. **14**(27): p. 8169-8176.
76. Muñoz, A., et al., *Nanorods versus Nanovesicles from Amphiphilic Dendrofullerenes.* Journal of the American Chemical Society, 2011. **133**(42): p. 16758-16761.
77. Nakanishi, T., et al., *Perfectly Straight Nanowires of Fullerenes Bearing Long Alkyl Chains on Graphite.* Journal of the American Chemical Society, 2006. **128**(19): p. 6328-6329.
78. Feng, M., et al., *Nanoscale templating of close-packed C-60 nanowires.* Journal of the American Chemical Society, 2007. **129**(41): p. 12394-+.
79. Rosen, B.M., et al., *Dendron-Mediated Self-Assembly, Disassembly, and Self-Organization of Complex Systems.* Chemical Reviews, 2009. **109**(11): p. 6275-6540.
80. Percec, V., et al., *Synthesis and structural analysis of two constitutional isomeric libraries of AB(2)-based monodendrons and supramolecular dendrimers.* Journal of the American Chemical Society, 2001. **123**(7): p. 1302-1315.
81. Rosen, B.M., et al., *Predicting the Structure of Supramolecular Dendrimers via the Analysis of Libraries of AB(3) and Constitutional Isomeric AB(2) Biphenylpropyl Ether Self-Assembling Dendrons.* Journal of the American Chemical Society, 2009. **131**(47): p. 17500-17521.
82. Percec, V., et al., *Self-assembly of amphiphilic dendritic dipeptides into helical pores.* Nature, 2004. **430**(7001): p. 764-768.
83. Percec, V., et al., *Programming the Internal Structure and Stability of Helical Pores Self-Assembled from Dendritic Dipeptides via the Protective Groups of the Peptide.* Journal of the American Chemical Society, 2005. **127**(50): p. 17902-17909.
84. Percec, V., et al., *Principles of self-assembly of helical pores from dendritic dipeptides.* Proceedings of the National Academy of Sciences of the United States of America, 2006. **103**(8): p. 2518-2523.
85. Percec, V., et al., *Helical Pores Self-Assembled from Homochiral Dendritic Dipeptides Based on l-Tyr and Nonpolar α-Amino Acids.* Journal of the American Chemical Society, 2007. **129**(18): p. 5992-6002.
86. Rosen, B.M., et al., *Programming the Supramolecular Helical Polymerization of Dendritic Dipeptides via the Stereochemical Information of the Dipeptide.* Journal of the American Chemical Society, 2011. **133**(13): p. 5135-5151.
87. Maringa, N., et al., *Liquid-crystalline methanofullerodendrimers which display columnar mesomorphism.* Journal of Materials Chemistry, 2008. **18**(13): p. 1524-1534.
88. Allard, E., et al., *Liquid-crystalline [60]fullerene-TTF dyads.* Organic Letters, 2005. **7**(3): p. 383-386.
89. Campidelli, S., et al., *Supramolecular fullerene materials: Dendritic liquid-crystalline fulleropyrrolidines.* Macromolecules, 2005. **38**(19): p. 7915-7925.
90. Hilmer, A.J., N. Nair, and M.S. Strano, *A kinetic Monte Carlo analysis for the production of singularly tethered carbon nanotubes.* Nanotechnology, 2010. **21**(49): p. 495703.

91. Wunderlich, D., F. Hauke, and A. Hirsch, *Preferred functionalization of metallic and small-diameter single walled carbon nanotubes via reductive alkylation.* Journal of Materials Chemistry, 2008. **18**(13): p. 1493-1497.
92. Caswell, K.K., et al., *Preferential end-to-end assembly of gold nanorods by biotin-streptavidin connectors.* Journal of the American Chemical Society, 2003. **125**(46): p. 13914-13915.
93. Tasis, D., et al., *Chemistry of carbon nanotubes.* Chemical Reviews, 2006. **106**(3): p. 1105-1136.
94. Cognet, L., et al., *Stepwise quenching of exciton fluorescence in carbon nanotubes by single-molecule reactions.* Science, 2007. **316**(5830): p. 1465-1468.
95. Siitonen, A.J., et al., *Surfactant-Dependent Exciton Mobility in Single-Walled Carbon Nanotubes Studied by Single-Molecule Reactions.* Nano Letters, 2010.
96. Kim, W.J., M.L. Usrey, and M.S. Strano, *Selective functionalization and free solution electrophoresis of single-walled carbon nanotubes: Separate enrichment of metallic and semiconducting SWNT.* Chemistry of Materials, 2007. **19**(7): p. 1571-1576.
97. Hersam, M.C., *Progress towards monodisperse single-walled carbon nanotubes.* Nature Nanotechnology, 2008. **3**(7): p. 387-394.
98. Arnold, M.S., et al., *Sorting carbon nanotubes by electronic structure using density differentiation.* Nature Nanotechnology, 2006. **1**(1): p. 60-65.
99. Ghosh, S., S.M. Bachilo, and R.B. Weisman, *Advanced sorting of single-walled carbon nanotubes by nonlinear density-gradient ultracentrifugation.* Nat Nano, 2010. **5**(6): p. 443-450.
100. Nish, A., et al., *Highly selective dispersion of singlewalled carbon nanotubes using aromatic polymers.* Nature Nanotechnology, 2007. **2**(10): p. 640-646.
101. Krupke, R., et al., *Separation of metallic from semiconducting single-walled carbon nanotubes.* Science, 2003. **301**(5631): p. 344-347.
102. Shin, D.H., et al., *Continuous Extraction of Highly Pure Metallic Single-Walled Carbon Nanotubes in a Microfluidic Channel.* Nano Letters, 2008. **8**(12): p. 4380-4385.
103. Tu, X.M., et al., *DNA sequence motifs for structure-specific recognition and separation of carbon nanotubes.* Nature, 2009. **460**(7252): p. 250-253.
104. Zheng, M., et al., *Structure-based carbon nanotube sorting by sequence-dependent DNA assembly.* Science, 2003. **302**(5650): p. 1545-1548.
105. Kim, W.J., et al., *Covalent functionalization of single-walled carbon nanotubes alters their densities allowing electronic and other types of separation.* Journal of Physical Chemistry C, 2008. **112**(19): p. 7326-7331.
106. Hayter, A.J., *Probability and statistics for engineers and scientists*. 3rd ed. 2007, Belmont, Calif.: Thomson Brooks/Cole. xviii, 812 p.
107. Bard, A.J. and L.R. Faulkner, *Electrochemical methods : fundamentals and applications*. 2nd ed. 2001, New York: Wiley. xxi, 833 p.
108. Gillespie, D.T., *Exact Stochastic Simulation of Coupled Chemical-Reactions.* Journal of Physical Chemistry, 1977. **81**(25): p. 2340-2361.
109. Reich, S., et al., *Tight-binding description of graphene.* Physical Review B, 2002. **66**(3): p. -.
110. Mintmire, J.W. and C.T. White, *Universal density of states for carbon nanotubes.* Physical Review Letters, 1998. **81**(12): p. 2506-2509.

111. Ding, F., A.R. Harutyunyan, and B.I. Yakobson, *Dislocation theory of chirality-controlled nanotube growth.* Proceedings of the National Academy of Sciences of the United States of America, 2009. **106**(8): p. 2506-2509.
112. Luo, Z.T., et al., *(n,m) abundance evaluation of single-walled carbon nanotubes by fluorescence and absorption spectroscopy.* Journal of the American Chemical Society, 2006. **128**(48): p. 15511-15516.
113. Usrey, M.L., et al., *Controlling the electrophoretic mobility of single-walled carbon nanotubes: A comparison of theory and experiment.* Langmuir, 2007. **23**(14): p. 7768-7776.
114. Bronikowski, M.J., et al., *Gas-phase production of carbon single-walled nanotubes from carbon monoxide via the HiPco process: A parametric study.* Journal of Vacuum Science & Technology a-Vacuum Surfaces and Films, 2001. **19**(4): p. 1800-1805.
115. Chen, Y., et al., *Synthesis of uniform diameter single wall carbon nanotubes in Co-MCM-41: effects of CO pressure and reaction time.* Journal of Catalysis, 2004. **226**(2): p. 351-362.
116. Chen, Y., et al., *Synthesis of uniform diameter single-wall carbon nanotubes in Co-MCM-41: effects of the catalyst prereduction and nanotube growth temperatures.* Journal of Catalysis, 2004. **225**(2): p. 453-465.
117. Huang, S.M., et al., *Growth mechanism of oriented long single walled carbon nanotubes using "fast-heating" chemical vapor deposition process.* Nano Letters, 2004. **4**(6): p. 1025-1028.
118. Liu, Q.F., et al., *Diameter-selective growth of single-walled carbon nanotubes with high quality by floating catalyst method.* Acs Nano, 2008. **2**(8): p. 1722-1728.
119. You, C., et al., *Self-Controlled Monofunctionalization of Quantum Dots for Multiplexed Protein Tracking in Live Cells13.* Angewandte Chemie, 2010. **122**(24): p. 4202-4206.
120. Hilmer, A.J., et al., *Role of Adsorbed Surfactant in the Reaction of Aryl Diazonium Salts with Single-Walled Carbon Nanotubes.* Langmuir, 2012. **28**(2): p. 1309-1321.
121. Schnorr, J.M. and T.M. Swager, *Emerging Applications of Carbon Nanotubes†.* Chemistry of Materials, 2010. **23**(3): p. 646-657.
122. Kostarelos, K., A. Bianco, and M. Prato, *Promises, facts and challenges for carbon nanotubes in imaging and therapeutics.* Nat Nano, 2009. **4**(10): p. 627-633.
123. Bianco, A., K. Kostarelos, and M. Prato, *Applications of carbon nanotubes in drug delivery.* Current Opinion in Chemical Biology, 2005. **9**(6): p. 674-679.
124. Menard-Moyon, C., et al., *The alluring potential of functionalized carbon nanotubes in drug discovery.* Expert Opinion on Drug Discovery, 2010. **5**(7): p. 691-707.
125. Lin, Y., et al., *Glucose Biosensors Based on Carbon Nanotube Nanoelectrode Ensembles.* Nano Letters, 2003. **4**(2): p. 191-195.
126. Cai, H., et al., *Carbon nanotube-enhanced electrochemical DNA biosensor for DNA hybridization detection.* Analytical and Bioanalytical Chemistry, 2003. **375**(2): p. 287-293.
127. Zhao, P., et al., *First-principles study of the switching characteristics of the phenoxynaphthacenequinone-based optical molecular switch with carbon nanotube electrodes.* Physica E: Low-dimensional Systems and Nanostructures, 2009. **41**(3): p. 474-478.
128. Li, X.F., et al., *Nanomechanically induced molecular conductance switch.* Applied Physics Letters, 2009. **95**(23).

129. Sorgenfrei, S., et al., *Label-free single-molecule detection of DNA-hybridization kinetics with a carbon nanotube field-effect transistor.* Nat Nano, 2011. **6**(2): p. 126-132.
130. Goldsmith, B.R., et al., *Conductance-controlled point functionalization of single-walled carbon nanotubes.* Science, 2007. **315**(5808): p. 77-81.
131. Siitonen, A.J., et al., *Surfactant-Dependent Exciton Mobility in Single-Walled Carbon Nanotubes Studied by Single-Molecule Reactions.* Nano Letters, 2010. **10**(5): p. 1595-1599.
132. Singh, P., et al., *Organic functionalisation and characterisation of single-walled carbon nanotubes.* Chemical Society Reviews, 2009. **38**(8): p. 2214-2230.
133. Bahr, J.L., et al., *Functionalization of Carbon Nanotubes by Electrochemical Reduction of Aryl Diazonium Salts: A Bucky Paper Electrode.* Journal of the American Chemical Society, 2001. **123**(27): p. 6536-6542.
134. Graff, R.A., T.M. Swanson, and M.S. Strano, *Synthesis of nickel-nitrilotriacetic acid coupled single-walled carbon nanotubes for directed self-assembly with polyhistidine-tagged proteins.* Chemistry of Materials, 2008. **20**(5): p. 1824-1829.
135. Li, H.M., et al., *Functionalization of single-walled carbon nanotubes with well-defined polystyrene by "click" coupling.* Journal of the American Chemical Society, 2005. **127**(41): p. 14518-14524.
136. Patai, S., *The Chemistry of diazonium and diazo groups*. The Chemistry of functional groups. 1978, Chichester Eng. ; New York: J. Wiley.
137. Doyle, C.D., et al., *Structure-dependent reactivity of semiconducting single-walled carbon nanotubes with benzenediazonium salts.* Journal of the American Chemical Society, 2008. **130**(21): p. 6795-6800.
138. Schmidt, G., et al., *Mechanism of the Coupling of Diazonium to Single-Walled Carbon Nanotubes and Its Consequences.* Chemistry-a European Journal, 2009. **15**(9): p. 2101-2110.
139. Schmidt, G., et al., *Labile Diazo Chemistry for Efficient Silencing of Metallic Carbon Nanotubes.* Chemistry – A European Journal, 2011. **17**(5): p. 1415-1418.
140. Liu, J., et al., *A simple chemical route to selectively eliminate metallic carbon nanotubes in nanotube network devices.* Journal of the American Chemical Society, 2004. **126**(34): p. 10520-10521.
141. Burghard, M., et al., *A selective electrochemical approach to carbon nanotube field-effect transistors.* Nano Letters, 2004. **4**(5): p. 827-830.
142. Israelachvili, J.N., *Intermolecular and surface forces*. 3rd ed. 2011, Burlington, MA: Academic Press. xxx, 674 p.
143. Piran, M., et al., *End-selective functionalization of carbon nanotubes. Use of DOE for the optimization of a DNA probe attachment and hybridization using an enzymatic amplifying system.* Journal of Materials Chemistry, 2009. **19**(5): p. 631-638.
144. O'Connell, M.J., et al., *Band gap fluorescence from individual single-walled carbon nanotubes.* Science, 2002. **297**(5581): p. 593-596.
145. Jin, Z., et al., *Click Chemistry on Solution-Dispersed Graphene and Monolayer CVD Graphene.* Chemistry of Materials, 2011. **23**(14): p. 3362-3370.
146. Seyedi, S.M., et al., *Design, synthesis and SAR studies of 4-allyoxyaniline amides as potent 15-lipoxygensae inhibitors.* Bioorganic & Medicinal Chemistry, 2009. **17**(4): p. 1614-1622.

147. Barone, P.W., et al., *Modulation of Single-Walled Carbon Nanotube Photoluminescence by Hydrogel Swelling.* Acs Nano, 2009. **3**(12): p. 3869-3877.
148. Richard, C., et al., *Supramolecular Self-Assembly of Lipid Derivatives on Carbon Nanotubes.* Science, 2003. **300**(5620): p. 775-778.
149. Striolo, A. and N.R. Tummala, *SDS Surfactants on Carbon Nanotubes: Aggregate Morphology.* Acs Nano, 2009. **3**(3): p. 595-602.
150. Yang, X.N., Z.J. Xu, and Z. Yang, *A Molecular Simulation Probing of Structure and Interaction for Supramolecular Sodium Dodecyl Sulfate/Single-Wall Carbon Nanotube Assemblies.* Nano Letters, 2010. **10**(3): p. 985-991.
151. Mukhopadhyay, S. and U. Maitra, *Chemistry and biology of bile acids.* Current Science, 2004. **87**(12): p. 1666-1683.
152. Lin, S.C. and D. Blankschtein, *Role of the Bile Salt Surfactant Sodium Cholate in Enhancing the Aqueous Dispersion Stability of Single-Walled Carbon Nanotubes: A Molecular Dynamics Simulation Study.* Journal of Physical Chemistry B, 2010. **114**(47): p. 15616-15625.
153. Vlachy, V., *Ionic effects beyond Poisson-Boltzmann theory.* Annual Review of Physical Chemistry, 1999. **50**: p. 145-165.
154. Borukhov, I., *Charge renormalization of cylinders and spheres: Ion size effects.* Journal of Polymer Science Part B-Polymer Physics, 2004. **42**(19): p. 3598-3615.
155. Siitonen, A.J., et al., *Dependence of Exciton Mobility on Structure in Single-Walled Carbon Nanotubes.* The Journal of Physical Chemistry Letters, 2010. **1**(14): p. 2189-2192.
156. Hiemenz, P.C. and R. Rajagopalan, *Principles of colloid and surface chemistry.* 3rd ed. 1997, New York: Marcel Dekker. xix, 650 p.
157. Borukhov, I., D. Andelman, and H. Orland, *Steric effects in electrolytes: A modified Poisson-Boltzmann equation.* Physical Review Letters, 1997. **79**(3): p. 435-438.
158. D'Angelo, P., V. Migliorati, and L. Guidoni, *Hydration Properties of the Bromide Aqua Ion: the Interplay of First Principle and Classical Molecular Dynamics, and X-ray Absorption Spectroscopy.* Inorganic Chemistry, 2010. **49**(9): p. 4224-4231.
159. Raugei, S. and M.L. Klein, *An ab initio study of water molecules in the bromide ion solvation shell.* Journal of Chemical Physics, 2002. **116**(1): p. 196-202.
160. Ricci, M.A., et al., *Hydration of sodium, potassium, and chloride ions in solution and the concept of structure maker/breaker.* Journal of Physical Chemistry B, 2007. **111**(48): p. 13570-13577.
161. White, J.A., et al., *The solvation of Na+ in water: First-principles simulations.* Journal of Chemical Physics, 2000. **113**(11): p. 4668-4673.
162. Grossiord, N., et al., *Determination of the surface coverage of exfoliated carbon nanotubes by surfactant molecules in aqueous solution.* Langmuir, 2007. **23**(7): p. 3646-3653.
163. McDonald, T.J., et al., *Kinetics of PL quenching during single-walled carbon nanotube rebundling and diameter-dependent surfactant interactions.* Journal of Physical Chemistry B, 2006. **110**(50): p. 25339-25346.
164. McDonald, T.J., et al., *Chiral-selective protection of single-walled carbon nanotube photoluminescence by surfactant selection.* Journal of Physical Chemistry C, 2007. **111**(48): p. 17894-17900.

165. Bonaccorso, F., et al., *Density Gradient Ultracentrifugation of Nanotubes: Interplay of Bundling and Surfactants Encapsulation.* The Journal of Physical Chemistry C, 2010. **114**(41): p. 17267-17285.
166. Dai, L.M., et al., *Carbon Nanomaterials for Advanced Energy Conversion and Storage.* Small, 2012. **8**(8): p. 1130-1166.
167. Welsher, K., et al., *A route to brightly fluorescent carbon nanotubes for near-infrared imaging in mice.* Nature Nanotechnology, 2009. **4**(11): p. 773-780.
168. Strano, M.S., et al., *Reversible, Band-Gap-Selective Protonation of Single-Walled Carbon Nanotubes in Solution.* The Journal of Physical Chemistry B, 2003. **107**(29): p. 6979-6985.
169. Dukovic, G., et al., *Reversible surface oxidation and efficient luminescence quenching in semiconductor single-wall carbon nanotubes.* Journal of the American Chemical Society, 2004. **126**(46): p. 15269-15276.
170. Heller, D.A., et al., *Multimodal optical sensing and analyte specificity using single-walled carbon nanotubes.* Nature Nanotechnology, 2009. **4**(2): p. 114-120.
171. Choi, J.H. and M.S. Strano, *Solvatochromism in single-walled carbon nanotubes.* Applied Physics Letters, 2007. **90**(22).
172. Wohlfarth, C., *Dielectric constant of hexadecane*, in *Data extract from Landolt-Börnstein IV/17: Static Dielectric Constants of Pure Liquids and Binary Liquid Mixtures*, M.D. Lechner, Editor. 2008, Springer-Verlag Berlin Heidelberg.
173. Fagan, J.A., et al., *Analyzing Surfactant Structures on Length and Chirality Resolved (6,5) Single-Wall Carbon Nanotubes by Analytical Ultracentrifugation.* Acs Nano, 2013. **7**(4): p. 3373-3387.
174. Price, A.H., J.O. Williams, and R.W. Munn, *Dielectric Tensor, Effective Polarizability and Local Electric-Field in Pyrene Crystals.* Chemical Physics, 1976. **14**(3): p. 413-419.
175. Ren, S.L., et al., *Ellipsometric Determination of the Optical-Constants of C60 (Buckminsterfullerene) Films.* Applied Physics Letters, 1991. **59**(21): p. 2678-2680.
176. Ren, S.L., et al., *Dielectric Function of Solid C-70 Films.* Applied Physics Letters, 1992. **61**(2): p. 124-126.
177. Armbruster, J.F., et al., *Electron-Energy-Loss and Photoemission-Studies of Solid C-84.* Physical Review B, 1994. **50**(7): p. 4933-4936.
178. Trasatti, S., *The Absolute Electrode Potential - an Explanatory Note (Recommendations 1986).* Pure and Applied Chemistry, 1986. **58**(7): p. 955-966.
179. Henson, Z.B., et al., *Pyridalthiadiazole-Based Narrow Band Gap Chromophores.* Journal of the American Chemical Society, 2012.
180. Herranz, M.A., C.T. Cox, and L. Echegoyen, *Retrocyclopropanation reactions of fullerenes: Complete product analyses.* Journal of Organic Chemistry, 2003. **68**(12): p. 5009-5012.
181. Tamaki, K., et al., *Acceleration of Photoinduced Electron Transfer in Porphyrin-Linked C70.* Chemistry Letters, 1999. **28**(3): p. 227-228.
182. Allemand, P.M., et al., *Two different fullerenes have the same cyclic voltammetry.* Journal of the American Chemical Society, 1991. **113**(3): p. 1050-1051.
183. Clarke, T.M. and J.R. Durrant, *Charge Photogeneration in Organic Solar Cells.* Chemical Reviews, 2010. **110**(11): p. 6736-6767.
184. Dresselhaus, M.S., et al., *Exciton photophysics of carbon nanotubes.* Annual Review of Physical Chemistry, 2007. **58**: p. 719-747.

185. Bingel, C., *Cyclopropanierung von Fullerenen.* Chemische Berichte, 1993. **126**(8): p. 1957-1959.
186. Alam, J., T.H. Keller, and T.-P. Loh, *Functionalization of Peptides and Proteins by Mukaiyama Aldol Reaction.* Journal of the American Chemical Society, 2010. **132**(28): p. 9546-9548.
187. Perez-Juste, J., et al., *Electric-field-directed growth of gold nanorods in aqueous surfactant solutions.* Advanced Functional Materials, 2004. **14**(6): p. 571-579.
188. Deng, S., et al., *Confined propagation of covalent chemical reactions on single-walled carbon nanotubes.* Nat Commun, 2011. **2**: p. 382.